Mixing by Swimming at Intermediate Reynolds Number

by

Thomas Albert Morrell

A dissertation submitted in partial fulfillment of

the requirements for the degree of

Doctor of Philosophy

(Mathematics)

at the

UNIVERSITY OF WISCONSIN–MADISON

2019

Date of final oral examination: 04/22/2019

The dissertation is approved by the following members of the Final Oral Committee:

Saverio Spagnolie, Associate Professor, Mathematics
Jean-Luc Thiffeault, Professor, Mathematics
Samuel Stechmann, Professor, Mathematics
Michael Graham, Professor, Chemical and Biological Engineering

To my loving wife and family, for their endless support.

ACKNOWLEDGMENTS

I am forever indebted to my advisors, Saverio Spagnolie and Jean-Luc Thiffeault, for their many years of mentorship. I would also like to thank the other members of my committee: Samuel Stechmann and Michael Graham.

I also owe a deep debt of gratitude to my wife, Leah, as well as to both my parents, Jim and Susan Morrell, and my in-laws, Larry Laux and Nina Wulff. Thank you for being an ever-present source of love and support, and freeing my mind to focus on my research and education.

CONTENTS

LIST OF FIGURES

ABSTRACT

Much study has been made previously of the effects of swimming at low Reynolds number, particularly with regards to velocity fluctuations caused by different swimmers and to particle displacements over time. This work extends those studies to intermediate Reynolds number. In this regime, the effects of inertia emerge, while viscosity still plays a central role. A suspension of viscous vortex rings is presented as a model for the fluctuations in the flow field caused by jellyfish, which decay spatially as $O(r^{-3})$ and temporally as $O(t^{-3/2})$, with these asymptotic regimes separated by a diffusive front where viscous stresses modify the flow.

For a dilute suspension of viscous vortex rings, the distribution of velocity fluctuations is found to be a truncated $\frac{5}{3}$-stable distribution. This result is robust in that the flow due to any randomized forcing with impulses isolated in space and time will follow the same distribution. These observations can be understood in terms of analogous results for microswimmers, but with the addition of needing to consider the time required for momentum to diffuse, often approximated to be instantaneous at low Reynolds number. The behavior of particle displacements due to these velocity fluctuations is more complicated. Due to the addition of an extra time scale, results found for microswimmers, while qualitatively similar to numerical observations, cannot be applied to understand the displacements at larger length scales. The mean square drift after a time t grows as $t^{3/2}$, indicating

superdiffusive particle dispersion. The probability density function of the distribution of drifts features a Gaussian core comprising of small velocities with width scaling linearly in time, transient tails obeying a -3 power law (for small times), and exponentially-decaying tails for the largest drifts.

1 PRELIMINARIES

1.1 Introduction

Mixing by swimming has been studied extensively for microswimmers. Dewar et al. (2006), among others, suggested that the aquatic life mix the ocean, and that this mixing may be a significant source of energy for global ocean circulation. Although relatively early studies, e.g., Huntley and Zhou (2004), found that animals of all sizes produce a similar energy output per kilogram, most later studies have focused on microorganisms, which typically swim in high-density plumes. Some work has been done at intermediate length scales, however, especially with regards to understanding a mechanism by which jellyfish can mix the ocean (Katija and Dabiri, 2009). In Chapters 3 and 4, we analyze the distributions of velocity fluctuations and drifts for viscous vortex rings, e.g., produced by swimming jellyfish, extending results for microswimmers.

This thesis is structured as follows: in Chapter 1, we recall several useful properties of stable distributions, differentiating by stability parameter α. Of particular interest are the differences between the Gaussian distribution ($\alpha = 2$) and non-Gaussian stable distributions ($\alpha < 2$), which are said to be "tail-heavy." The differences between these distributions are explored for the velocity fluctuations and particle displacements due to microswimmers, when the heavy tails (or sometimes lack thereof) have physical significance. Chapter 2 explores properties of viscous vortex rings,

from which we will build a model for the fluid disturbances caused by jellyfish. We will use a model vortex ring due to Fukumoto and Kaplanski (2008) which has nice analytical properties. In particular, the velocity distribution due to a single vortex ring will be found to have finite moments M_n only for $\frac{5}{3} < n < 4$, which in Chapter 3 will be shown to imply that the velocity fluctuations due to a suspension of viscous vortex rings will follow a $\frac{5}{3}$-stable distribution. Further properties of the velocity field are analyzed in Chapter 4 to guide discussion of the distribution of particle displacements, or drifts, caused by the vortices. We find that the distribution of drifts transitions from a $\frac{5}{3}$-stable distribution at early times to a Gaussian at later times, and that the mean square drift grows superdiffusively.

The above findings are robust in that the details of the model are of secondary importance in determining the shapes of the velocity and drift distributions, so long as fluctuations are caused by impulses which are localized in space and time. We briefly discuss what happens when these force monopoles are replaced by dipoles or quadrupoles, etc., although more work is needed to determine whether anisotropy or correlations between various forces change the distributions.

1.2 Stable distributions

Let X_1, X_2 be independent random variables belonging to some probability distribution p. We say that p is stable if $aX_1 + bX_2$ $(a, b > 0)$ has the same

distribution as $cX + d$, where $c > 0$ and X belongs to the same distribution p. Such distributions were first studied by Lévy (1925) and are sometimes called Lévy stable distributions in his honor.

The general form of a stable distribution over a single random variable can be written in Fourier space:

$$p(x) = \frac{1}{2\pi} \int_{-\infty}^{\infty} \varphi(k) e^{-ikx} dk. \tag{1.1}$$

The characteristic function φ can be expressed in terms of four parameters:

$$\varphi(k; \alpha, \beta, c, \mu) = \exp\left(ik\mu - |ck|^{\alpha}(1 - i\beta \operatorname{sign}(k)\phi)\right), \tag{1.2}$$

where

$$\phi = \begin{cases} \tan\left(\frac{\pi\alpha}{2}\right), & \alpha \neq 1, \\ -\frac{2}{\pi} \log|ck|, & \alpha = 1 \end{cases} \tag{1.3}$$

(Voit, 2005). The parameter $\alpha \in (0, 2]$ is known as the stability parameter. Two special cases are $\alpha = 2$, which is the Gaussian distribution, and $\alpha = 1$, which is the Cauchy distribution. The location parameter $\mu \in \mathbb{R}$ corresponds to the mean for $\alpha > 1$ (mean is undefined for $\alpha \leqslant 1$), $\beta \in [-1, 1]$ is the skewness parameter, and $c > 0$ is the scale parameter. For the Gaussian ($\alpha = 2$), the skewness is zero and the variance is $2c^2$, while for $\alpha < 2$, the skewness is undefined and the variance is infinite.

For $\alpha < 2$, the distribution is tail-heavy:

$$p(x) \sim \frac{c^{\alpha}\Gamma(\alpha+1)}{\pi|x|^{\alpha+1}} \sin\left(\frac{\pi\alpha}{2}\right)(1+\text{sign}(x)\beta) \tag{1.4}$$

as $|x| \to \infty$ (Lévy, 1925; Feller, 1971; Zaid and Mizuno, 2016). For a truncated stable distribution, the $|x|^{-\alpha-1}$ tails only persist up to some finite value of $|x|$, with a faster decay beyond the cutoff, similar to Min et al. (1996). Such distributions may have additional finite moments depending on the nature of the distribution beyond the cutoff. The "core" region of the distribution around $x = \mu$ looks remarkably similar to that of a Gaussian when $\beta = 0$, but it is narrower due to the heavy tails.

Gnedenko and Kolmogorov (1968) proved a generalized version of the central limit theorem, which states that the sum of a number of i.i.d. random variables X_i with non-zero variance will converge to a stable distribution. By contrast, the standard central limit theorem, which indicates convergence to a 2-stable distribution (i.e., a Gaussian), only holds when the variance of the i.i.d. random variables is finite. Although the statement of the theorem and its proof are relatively complex, a simple corollary of the generalized central limit theorem is that if the probability density function of the X_i has power-law tails $|x|^{-1-\alpha}$ (for $0 < \alpha \leqslant 2$, so that the variance of the X_i is infinite), then the sum (as the number of summands increases) converges to an α-stable distribution. When $\alpha > 2$, then the variance is finite, so the sum of the X_i converges to a Gaussian distribution.

Via a change in coordinates, it is always possible to move the location μ to the origin and set the scale c to be unity. We will only need to consider the case of the symmetric stable distribution, which corresponds to $\beta = 0$. We will notate the standard symmetric α-stable distribution with these parameters by

$$\Phi_\alpha(x) = \frac{1}{2\pi}\int_{-\infty}^{\infty} e^{-ikx-|k|^\alpha}\,dx. \tag{1.5}$$

It will also be beneficial to create notation for a stable distribution with arbitrary width. By $\Phi_\alpha(x;a) := \frac{1}{a}\Phi_\alpha(x/a)$, denote the symmetric stable distribution with mean zero and scale $c = a^{1/\alpha}$.

While most α-stable distributions do not have analytic expressions, we can write the standard symmetric $\frac{5}{3}$-stable distribution in terms of generalized hypergeometric functions ${}_pF_q$, which appears to be a new result:

$$\begin{aligned}
\Phi_{5/3}(x) = {} & \frac{3^{11/10}\Gamma(\frac{1}{5})\Gamma(\frac{8}{15})\Gamma(\frac{13}{15})}{10\pi^2}\,{}_4F_7\left(\tfrac{4}{15},\tfrac{13}{30},\tfrac{23}{30},\tfrac{14}{15};\tfrac{1}{5},\tfrac{3}{10},\tfrac{2}{5},\tfrac{1}{2},\tfrac{7}{10},\tfrac{8}{10},\tfrac{9}{10};-\xi\right) \\
& - \frac{3^{23/10}x^2\Gamma(\frac{1}{5})\Gamma(\frac{14}{15})\Gamma(\frac{19}{15})}{100\cdot 2^{1/5}\pi^{3/2}\Gamma(\frac{11}{10})}\,{}_4F_7\left(\tfrac{7}{15},\tfrac{19}{30},\tfrac{29}{30},\tfrac{17}{15};\tfrac{2}{5},\tfrac{1}{2},\tfrac{3}{5},\tfrac{7}{10},\tfrac{9}{10},\tfrac{11}{10},\tfrac{6}{5};-\xi\right) \\
& - \frac{3^{27/10}x^6\Gamma(\frac{26}{15})\Gamma(\frac{31}{15})\Gamma(\frac{12}{5})}{1120\pi^2}\,{}_4F_7\left(\tfrac{13}{15},\tfrac{31}{30},\tfrac{41}{30},\tfrac{23}{15};\tfrac{4}{5},\tfrac{9}{10},\tfrac{11}{10},\tfrac{13}{10},\tfrac{7}{5},\tfrac{3}{2},\tfrac{8}{5};-\xi\right) \\
& + \frac{3^{19/10}x^8\Gamma(\frac{32}{15})\Gamma(\frac{37}{15})\Gamma(\frac{14}{5})}{8960\pi^2}\,{}_4F_7\left(\tfrac{16}{15},\tfrac{37}{30},\tfrac{47}{30},\tfrac{26}{15};\tfrac{11}{10},\tfrac{6}{5},\tfrac{13}{10},\tfrac{3}{2},\tfrac{8}{5},\tfrac{17}{10},\tfrac{9}{5};-\xi\right) \\
& + \frac{x^4}{20\pi}\,{}_5F_8\left(\tfrac{2}{3},\tfrac{5}{6},1,\tfrac{7}{6},\tfrac{4}{3};\tfrac{3}{5},\tfrac{7}{10},\tfrac{4}{5},\tfrac{9}{10},\tfrac{11}{10},\tfrac{6}{5},\tfrac{13}{10},\tfrac{7}{5};-\xi\right),
\end{aligned} \tag{1.6}$$

where $\xi = 729x^{10}/156250000$. This expression unfortunately has little

computational value as the terms grow polynomially, while $\Phi_{5/3}(x)$ decays like $|x|^{-8/3}$ as $|x| \to \infty$, so an ever increasing number of terms in the expansions of the generalized hypergeometric functions are required to approximate Φ accurately for large x. Fortunately, the integral (1.5) converges numerically very quickly.

1.3 Velocity fluctuations in fluids

A natural question when faced with a fluid flow with some degree of randomness is how to characterize its velocity fluctuations. This is a classical problem in turbulence, but also in gravitational sedimentation (Caflisch and Luke, 1985; Nicolai and Herzhaft, 1995; Luke, 2000; Mucha et al., 2004; Guazzelli and Hinch, 2011; Möller and Naraynan, 2017), and in suspensions of microswimmers (Dombrowski et al., 2004; Drescher et al., 2010; Guasto et al., 2010; Ishikawa and Pedley, 2007; Ishikawa, 2009; Leptos et al., 2009; Rushkin et al., 2010; Underhill et al., 2008; Yeomans et al., 2014; Lin et al., 2011; Zaid et al., 2011; Zaid and Mizuno, 2016; Delmotte et al., 2018). In the case of sedimentation and microswimmers, the velocity field due to a single particle or swimmer is commonly used as a building block to understand the velocity distribution in the full system. At leading order for a dilute suspension, interactions are neglected and much is learned by examining a random superposition of individual particles or swimmers. In particular, for small velocities the distribution is typically identified

as Gaussian (Delmotte et al., 2018), since superimposing many distant sources usually results in an application of the (gneralized) central limit theorem, although there are a number of situations for which we more generally find a (different) stable distribution.

Biomixing

Biomixing is the study of the velocity fluctuations and particle dispersion within a body of water (e.g., the ocean, a lake, a tank, etc.) due to the swimming motions of biological life forms. Since larger organisms tend to be sparsely distributed (Visser, 2007), much of the focus on biomixing has been at small length scales, where the fluid velocity $\mathbf{u}$ is governed by the Stokes equations:

$$\mathbf{0} = -\boldsymbol{\nabla} p + \eta \nabla^2 \mathbf{u} + \mathbf{f}, \tag{1.7}$$

$$0 = \boldsymbol{\nabla} \cdot \mathbf{u}, \tag{1.8}$$

where η is the kinematic viscosity, p the (reduced) pressure, and $\mathbf{f}$ is the external forcing.

Since the Stokes equations are linear, much can be learned by solving for the response of a point force $\mathbf{f} = \mathbf{F}\delta(\mathbf{r})$ applied at the origin, i.e., finding the Green's function (see, e.g., Graham (2018)). Towards this end, take the

divergence of (1.7) and apply (1.8) to eliminate the velocity. Then

$$0 = -\nabla^2 p + \boldsymbol{\nabla} \cdot \mathbf{f} = -\nabla^2 p + \mathbf{F}\, \boldsymbol{\nabla} \cdot \delta(\mathbf{r}). \tag{1.9}$$

The divergence of a delta function is an awkward expression with which to work, so let ϕ be the Green's function for Laplace's equation, i.e., $\nabla^2 \phi = \delta(\mathbf{r})$. Then

$$0 = -\nabla^2 p - \nabla^2(\mathbf{F} \cdot \boldsymbol{\nabla}\phi). \tag{1.10}$$

Therefore, the pressure is

$$p = -\mathbf{F} \cdot \boldsymbol{\nabla}\phi + h(\mathbf{r}), \tag{1.11}$$

where h is a harmonic function chosen to satisfy the boundary conditions. Assuming an otherwise quiescent fluid filling all of space, $h = 0$. Plugging (1.11) into (1.7), we find that

$$\eta \nabla^2 \mathbf{u} = -\mathbf{F} \cdot (\boldsymbol{\nabla}\boldsymbol{\nabla}\phi - \mathbb{I}\nabla^2\phi), \tag{1.12}$$

where $\mathbb{I}$ is the identity tensor. Now let $\nabla^2 \zeta = \phi$, so that

$$\nabla^2 \mathbf{u} = -\nabla^2 \left(\frac{1}{\eta} \mathbf{F} \cdot (\boldsymbol{\nabla}\boldsymbol{\nabla}\zeta - \mathbb{I}\phi) \right). \tag{1.13}$$

As before, we can remove the Laplacian operators and then need to add an arbitrary harmonic function, but by boundary conditions, that function

will again be zero, so

$$\mathbf{u} = -\frac{1}{\eta}\mathbf{F} \cdot (\boldsymbol{\nabla}\boldsymbol{\nabla}\zeta - \mathbb{I}\phi). \tag{1.14}$$

It is rather straightforward to show that in three dimensions, $\phi = 1/4\pi r$ and $\zeta = r/8\pi$, so

$$\mathbf{u} = \frac{1}{8\pi\eta r}\left(\mathbb{I} + \frac{\mathbf{rr}}{r^2}\right) \cdot \mathbf{F}, \tag{1.15}$$

which is called the Stokeslet. Of particular note for us is that $\mathbf{u}$ scales as $1/r$ for large distances. This also holds true if the Stokeslet is regularized (although the near-field velocity may change).

One may consider a random, isotropic arrangement of Stokeslets in a fluid. A natural question is then, "what is the distribution of fluid velocities?" To answer this question, it is necessary to find a probability density for measuring a given velocity for a single, randomly-oriented Stokeslet in some finite volume V, i.e.,

$$p_1(\mathbf{v}) = \frac{1}{4\pi V}\int_\Omega \int_V \delta(\mathbf{O} \cdot \mathbf{u}(\mathbf{r}) - v)\, dV_\mathbf{r}\, d\Omega = \frac{1}{V}\int_V \delta(u(\mathbf{r}) - v)\, dV_\mathbf{r}, \tag{1.16}$$

where $\mathbf{O}$ is the orientation, $u = |\mathbf{u}|$, $v = |\mathbf{v}|$, and the outer integral is over all possible orientations of the Stokeslet. The assumption of isotropy allows us to ignore the directions of the velocity vectors and instead focus solely on the magnitudes. The remaining delta function constrains the integral

to the surface $u(\mathbf{r}) = v$, so

$$p_1(\mathbf{v}) = \frac{1}{V}\int_{S(v)} \frac{dS_{\mathbf{r}}}{|\boldsymbol{\nabla}_{\mathbf{r}}\, u(\mathbf{r})|}, \tag{1.17}$$

where $S(v)$ is the surface comprising of all points where the velocity $\mathbf{u}$ has magnitude equal to v. Let θ be the angle between the position $\mathbf{r}$ and the force $\mathbf{F}$. Then

$$u(\mathbf{r}) = \frac{F\sqrt{1+3\cos^2\theta}}{8\pi\eta r}, \tag{1.18}$$

where $F = |\mathbf{F}|$, so, inverting to solve for r as a function of u,

$$r = \frac{F\sqrt{1+3\cos^2\theta}}{8\pi\eta u}. \tag{1.19}$$

Also,

$$|\boldsymbol{\nabla}_{\mathbf{r}}\, u(\mathbf{r})| = \frac{F}{8\pi\eta r^2}\sqrt{\frac{1+15\cos^2\theta}{1+3\cos^2\theta}} = \frac{8\pi\eta u^2(1+15\cos^2\theta)^{1/2}}{F(1+3\cos^2\theta)^{3/2}}, \tag{1.20}$$

where we have used (1.19) to get an expression for the gradient which does not explicitly depend on r. Then (1.17) can be rewritten as an integral over θ:

$$p_1(\mathbf{v}) = \frac{2\pi}{V}\int_0^{\pi} \frac{r(\theta)\sqrt{r(\theta)^2 + r'(\theta)^2}}{|\boldsymbol{\nabla} u|(\theta)} \sin\theta\, d\theta \approx \frac{2.403\times 10^{-3}}{V}\frac{F^3}{\eta^3 v^4}. \tag{1.21}$$

Here we have written the surface in spherical coordinates as $r = r(\theta)$ (there is no dependence on the polar angle φ) and then computed the surface

area element $dS = |\mathbf{r}_\theta \times \mathbf{r}_\varphi| \, d\theta \, d\varphi = r(\theta) \sin\theta \sqrt{r(\theta)^2 + r'(\theta)^2} \, d\theta \, d\varphi$. The integral over φ is trivial, as the integrand is independent of φ.

Here the actual coefficient is not so important as the fact that $p_1(\mathbf{v})$ scales as ν^{-4} for small ν. For the Stokeslet, $p_1(\mathbf{v})$ also scales as ν^{-4} for large speeds ν, but if we regularize the Stokeslet to model more realistic behavior in the neighborhood of the force, the large ν scaling breaks down, while the small ν scaling, which is contributed to by points far away from the force, is preserved. Note that all of the above discussion requires ν to not be too small so that all points with $u = \nu$ are actually contained within the domain V. Once ν is small enough that we exit our domain, a different scaling emerges (although this will be unimportant for our purposes).

Now Rushkin et al. (2010) note that the second moment of $p_1(\nu)$ is finite (ignoring the limit $\nu \to 0$, which has a different scaling due to the boundary of the domain), so it is possible to apply the central limit theorem to determine that the distribution of velocities in a random isotropic suspension of Stokeslets converges to a Gaussian. Experimental observations in the same paper confirm that the distribution is indeed Gaussian, except for tails falling as ν^{-4} outside some core region.

However, the justification provided for why this should be is insufficient. Their study looks at several fixed volume fractions ϕ of microswimmers, but in a large enough domain that one can pretend $r_{max} \to \infty$, so there are an infinite number of swimmers ($N \to \infty$). The central limit theorem, however, naïvely applies in the case as $\phi \to \infty$, not as $N \to \infty$,

so the observations made do not immediately fall under its purview.

That said, the conclusions reached by Rushkin et al. (2010) are correct. Instead of just considering the case of a Stokeslet, assume instead that the velocity field of a swimmer decays as $v \sim r^{-n}$ instead. Then $p_1(v) \sim v^{-1-3/n}$ for v not too large (so long as v is large enough that all points with velocity v are contained within the domain). For $n < 3/2$, the resulting velocity distribution for the suspension of swimmers is Gaussian, while for larger n, the velocity distribution is a $\frac{3}{n}$-stable distribution. Zaid et al. (2011) confirm the correctness of this prediction numerically and create a model for a regularized flow field which provides analytical justification, although it is not clear that they fully understand why the distribution is non-Gaussian. They write, "for $n \geqslant 2$, the variance of [the probability density function] remains very large and the convergence to a Gaussian limiting distribution is very slow." However, as n increases, the velocity at every point in space typically decreases, which lowers the variance of the distribution.

A much simpler argument which shows that the velocity distribution converges to a Gaussian for $n < \frac{3}{2}$ and a $\frac{3}{n}$-stable distribution for $n \geqslant \frac{3}{2}$ is presented in the next subsection. Also, the direct calculation performed in Section 3.2 for a viscous vortex ring is easily modified to show convergence to a $\frac{3}{n}$-stable distribution for $n \geqslant \frac{3}{2}$.

Zaid and Mizuno (2016) also include the effects of truncating the distribution at large velocities (since true Stokeslets, stresslets, etc., don't occur in nature – the singularities are unphysical) and give an analytic formula

and explanation for a transition from a truncated stable distribution to a Gaussian distribution as n increases, including information about the intermediate distributions, but arguments for this transition are much older (see, e.g., Shlesinger (1995)). Since the details of the distribution for large velocities depend heavily on the exact flow field (see, e.g., (3.36)), the qualitative description of the distribution will generally be more enlightening (and more accurate for real flows), than the analytic expression.

Improved justification for the shape of the distribution

Consider a uniform isotropic distribution of swimmers, each creating a velocity disturbance which scales like $v \sim r^{-n}$ as $r \to \infty$, so that $p_1(v) \sim v^{-1-3/n}$. This scaling only holds above some small velocity $v_{\min}$ due to the necessity of choosing a finite domain (so that the integral of $p_1(v)$ is unity). Values of the velocity smaller than $v_{\min}$ are attained outside the domain, lowering the probability that they are measured, possibly all the way to zero.

There is also a cutoff velocity $v_{\max}$ above which the scaling breaks down because the swimmers have finite size. This removes the singularity. Assuming $p_1(v)$ is zero outside the interval $[v_{\min}, v_{\max}]$,

$$p_1(\mathbf{v}) = \begin{cases} \dfrac{3}{4\pi n} \dfrac{v^{-3-3/n}}{v_{\min}^{-3/n} - v_{\max}^{-3/n}} & v_{\min} \leqslant v \leqslant v_{\max}, \\ 0 & \text{otherwise.} \end{cases} \tag{1.22}$$

Then the velocity at a given point in a suspension containing N swimmers is the sum of the velocities $\mathbf{U}_i$ of the fluid at that location due to each of the swimmers. Each $\mathbf{U}_i$ is independent and identically distributed according to (1.22):

$$\mathbf{U}^N = \sum_{i=1}^{N} \mathbf{U}_i. \tag{1.23}$$

Now if we want to take $N \to \infty$ while also keeping the number density of swimmers constant, we must also let r_{max} grow like $N^{1/3}$, so that the minimum velocity $v_{min} \propto N^{-n/3}$. Equivalently, we could keep v_{min} fixed, but increase the maximum velocity by a factor of $v_{max} \propto N^{n/3}$. In order to do so without changing the magnitude of the summed velocity, it will be necessary to then divide by $N^{n/3}$, so that

$$\mathbf{U}^N = N^{-n/3} \sum_{i=1}^{N} \mathbf{V}_i, \tag{1.24}$$

where the $\mathbf{V}_i$ are i.i.d. according to the distribution

$$p_1(\mathbf{v}; N) = \begin{cases} \dfrac{3}{4\pi n} \dfrac{v^{-3-3/n}}{v_{min}^{-3/n} - \dfrac{v_{max,ref}^{-3/n}}{N}} & v_{min} \leqslant v \leqslant N^{n/3} v_{max,ref}, \\ 0 & \text{otherwise}, \end{cases} \tag{1.25}$$

where $v_{max,ref}$ is the maximum velocity in the case where $N = 1$. Taking

the limit as $N \to \infty$, $p_1(\mathbf{v}; N)$ converges to the fixed distribution

$$p_1(\mathbf{v}; \infty) = \begin{cases} \dfrac{3}{4\pi n} \dfrac{\nu^{-3-3/n}}{\nu_{min}^{-3/n}} & \nu \geqslant \nu_{min} \\ 0 & \text{otherwise.} \end{cases} \tag{1.26}$$

Therefore, when (1.26) has finite variance σ^2, we can apply the central limit theorem:

$$\mathbf{U}^N = N^{-1/2} \sum_{i=1}^{N} N^{1/2-n/3} \mathbf{V}_i \to \mathcal{N}(0, N^{1-2n/3}\sigma^2) = \mathcal{N}(0, r_{max}^{3-2n}\sigma^2) \tag{1.27}$$

as $N, r_{max} \to \infty$. That is, the distribution of the suspension is Gaussian precisely when the variance of $p_1(\mathbf{v}; \infty)$ is finite. The corollary to the generalized central limit theorem mentioned in Section 1.2, when applied to $p_1(\mathbf{v}, \infty)$, immediately indicates convergence to a $\frac{3}{n}$-stable distribution for $n \geqslant \frac{3}{2}$. Note that although the distribution is Gaussian for $n < \frac{3}{2}$ (the values for which σ^2 is finite), the magnitude of the velocity fluctuations $\mathbf{U}^N$ depend on the size of the domain r_{max}.

This argument also holds when the velocity outside of the interval $\nu_{min} \leqslant \nu \leqslant \nu_{max}$ isn't identically zero, so long as the true value of ν_{max} is independent of N, and the lower bound on the power law, ν_{min}, goes to zero with increasing N.

Paradoxically, we see that the Gaussianity of the distribution is determined by whether the second moment of the distribution would be finite

considering the scaling of the small velocities as though it was the scaling of the large velocities.

Meanwhile, it seems that large velocities are generally due to the velocity fields created by the nearest single swimmer (with the background flow created by further away swimmers only entering into calculations at the next order), but this requires a different argument, which will be done for a slightly different scenario in Section 3.2. This observation sheds light on why it matters whether the velocity distribution is Gaussian or a different (truncated) stable distribution. The velocities in the core region of the distributions discussed in Section 1.2 is generally due to the sum of the effects due to many different swimmers, while the velocities outside the core region (in the tails of the distribution) are generally dominated by the contribution from a single swimmer. For a non-Gaussian truncated stable distribution, the heavy tails provide a large contribution to the variance, and so we can understand the flow in terms of tracer particles being moved around by the nearest swimmer at any given time. For a Gaussian distribution, however, the bulk of the variance comes from the core, so the velocity of a tracer particle is almost always due to the simultaneous effects of many different swimmers.

In light of these observations, the paradox is simply resolved. For $n < \frac{3}{2}$, the velocity field decays very slowly as $r \to \infty$. As a result, the velocity at any given point is due to the effects of all of the swimmers. Therefore, the tails of the distribution should make a subdominant contribution to the

energy – i.e., the distribution should be Gaussian. By contrast, if $n > \frac{3}{2}$, the velocity decays very rapidly, so most of the energy comes from tracers responding to the flow field created by a single swimmer. These appear in the tails of the probability density function, which must therefore be heavy. Therefore, the distribution is a non-Gaussain stable distribution.

1.4 Particle displacements in fluids

In addition to velocity fluctuations, the particle displacements (or drifts) as a result of these fluctuations have also been studied extensively for microswimmers. Leptos et al. (2009) found experimentally that the distribution of particle displacements due to swimming *Chlamydomonas reinhardtii* (which are "pullers," so they create velocity fields scaling like $\mathbf{v} \sim 1/r^2$) was a weighted sum of Gaussian and exponential distributions:

$$p(\Delta) = \frac{1-f}{(2\pi\delta_g^2)^{1/2}} e^{-\Delta^2/2\delta_g^2} + \frac{f}{2\delta_e} e^{-|\Delta|/\delta_e}, \tag{1.28}$$

where δ_g and δ_e are constants which each scale as $t^{1/2}$, and $0 \leqslant f \leqslant 1$ is the fraction of the distribution which comes from the exponential. Thiffeault (2015) also observed this distribution for later times and noted that the exponential tails are due to the rarity of close interactions between any given particle and the swimmers.

At earlier times, the tails of the distribution appear to be polynomial.

Pushkin and Yeomans (2013) predicted analytically that for large displacements,

$$p(\Delta) \propto |\Delta|^{-1-d/(n-1)}, \tag{1.29}$$

where d is the effective dimension of the system. Then the distribution will be Gaussian (with power law tails) for $d > 2(n-1)$ and $\frac{d}{n-1}$-stable otherwise. Thiffeault (2015) notes, however, that the near-field velocity generally typically does not follow a clean power law, as was assumed in the derivation of (1.29). *Chlamydomonas rienhardtii*, for example, produce a regularized stresslet ($n = 2$) and a source dipole ($n = 3$), and so at large enough volume fraction, the prediction (1.29) may not be observed, even for the smallest times. Numerical simulations by Thiffeault (2015) in $d = 3$ dimensions indicated that the tails of the probability distribution approximately followed the Δ^{-4} power law predicted by (1.29), but the log-log plot of the distribution in his Figure 5 has gently curved tails, indicating a very narrow range of validity of the power law. Experimental observations made by Ortlieb et al. (2019) confirm the accuracy of these numerical observations.

Zaid et al. (2011) note that the statistics of an active suspension are generally non-Gaussian and tend to exhibit features of Lévy processes, whose correlations are much less well-understood than those of Gaussian processes. For small times, however, they note that processes are essentially ballistic, as the local velocity field generally persists for some finite length

of time. For longer periods of time, autocorrelations seem to vanish, after which the Fourier transform of p is given by

$$\hat{p}(\mathbf{k}) = \exp\left(D_\alpha[K^\alpha - (K^2 + |\mathbf{k}|^2)^{\alpha/2}]t - D_0|\mathbf{k}|^2 t\right), \tag{1.30}$$

where D_0 is the diffusivity due to thermal fluctuations, D_α is the anomalous diffusion rate due to the Lévy processes, and K is a regularization parameter. The parameter α corresponds to the stability parameter of the velocity distribution, which is a non-Gaussian stable distribution for $n > \frac{3}{2}$. This model is of particular interest because it captures the qualitative change in the shape of the distribution of drifts over time from truncated non-Gaussian stable at short times to a distribution which appears to be the sum of Gaussian and exponential distributions, as in (1.28), at long times. It is unclear whether (1.30) can be generalized to the case where the velocity autocorrelation function decays at a much slower rate, such that it cannot be neglected, which appears to be a hard problem to fully solve analytically.

2 SINGLE VORTEX RINGS

This chapter reviews several calculations performed for single vortex rings acting under diffusion. Section 2.1 examines short-time calculations for the evolution of a thin vortex filament, while Section 2.2 reviews calculations performed for vortices which are in their final state of viscous decay. Finally, Section 2.3 rederives and explores some properties of a model viscous vortex ring due to Fukumoto and Kaplanski (2008) which behaves in agreement with the calculations in the other sections in both the short and long time regimes.

This chapter will not cover inviscid vortices, such as Hill's spherical vortex (Hill, 1894), since such vortices do not decay over time, but rather translate unchanged at a fixed velocity. The diffusion and ultimate decay of vortices, which is more realistic at low to intermediate Reynolds number, will lead to many interesting and unique results in later chapters.

Of particular interest to us will be swirl-free, axisymmetric vortex rings. Consider an infinite incompressible fluid initially at rest, with density set to unity. Cylindrical coordinates (ρ, ϑ, z) are chosen, so that by conservation of mass,

$$\frac{1}{\rho}\frac{\partial(\rho u_\rho)}{\partial \rho} + \frac{1}{\rho}\frac{\partial u_\vartheta}{\partial \vartheta} + \frac{\partial u_z}{\partial z} = 0, \tag{2.1}$$

and by conservation of momentum,

$$\frac{\partial u_\rho}{\partial t} + u_\rho \frac{\partial u_\rho}{\partial \rho} + \frac{u_\vartheta}{\rho}\frac{\partial u_\rho}{\partial \vartheta} - \frac{u_\vartheta^2}{\rho} + u_z \frac{\partial u_\rho}{\partial z} = -\frac{\partial p}{\partial \rho} \tag{2.2}$$
$$+ \eta\left(\frac{1}{\rho}\frac{\partial}{\partial \rho}\left(\rho \frac{\partial u_\rho}{\partial \rho}\right) - \frac{u_\rho}{\rho^2} + \frac{1}{\rho^2}\frac{\partial^2 u_\rho}{\partial \vartheta^2} - \frac{2}{\rho^2}\frac{\partial u_\vartheta}{\partial \vartheta} + \frac{\partial^2 u_\rho}{\partial z^2}\right)$$
$$\frac{\partial u_\vartheta}{\partial t} + u_\rho \frac{\partial u_\vartheta}{\partial \rho} + \frac{u_\vartheta}{\rho}\frac{\partial u_\vartheta}{\partial \vartheta} + \frac{u_\rho u_\vartheta}{\rho} + u_z \frac{\partial u_\vartheta}{\partial z} = -\frac{1}{\rho}\frac{\partial p}{\partial \vartheta} \tag{2.3}$$
$$+ \eta\left(\frac{1}{\rho}\frac{\partial}{\partial \rho}\left(\rho \frac{\partial u_\vartheta}{\partial \rho}\right) - \frac{u_\vartheta}{\rho^2} + \frac{1}{\rho^2}\frac{\partial^2 u_\vartheta}{\partial \vartheta^2} + \frac{2}{\rho^2}\frac{\partial u_\rho}{\partial \vartheta} + \frac{\partial^2 u_\vartheta}{\partial z^2}\right)$$
$$\frac{\partial u_z}{\partial t} + u_\rho \frac{\partial u_z}{\partial \rho} + \frac{u_\vartheta}{\rho}\frac{\partial u_z}{\partial \vartheta} + u_z \frac{\partial u_z}{\partial z} = -\frac{\partial p}{\partial z} \tag{2.4}$$
$$+ \eta\left(\frac{1}{\rho}\frac{\partial}{\partial \rho}\left(\rho \frac{\partial u_z}{\partial \rho}\right) + \frac{1}{\rho^2}\frac{\partial^2 u_z}{\partial \vartheta^2} + \frac{\partial^2 u_z}{\partial z^2}\right).$$

These are the Navier–Stokes equations. Here, u_ρ, u_ϑ, u_z are the components of the velocity in the ρ, ϑ, z-directions, respectively, p is the (reduced) pressure,[1] and η is the kinematic viscosity.

For an axisymmetric, swirl-free, vortex ring initially located at the origin and oriented in the $+z$-direction, it is clear by symmetry that the only component of vorticity which is nonzero is the azimuthal vorticity $\zeta = \frac{\partial u_\rho}{\partial z} - \frac{\partial u_z}{\partial \rho}$. The evolution equation for ζ can be found by taking the z-derivative of (2.2) and subtracting the ρ-derivative of (2.4):

$$\frac{\partial \zeta}{\partial t} + \frac{\partial (u_\rho \zeta)}{\partial \rho} + \frac{\partial (u_z \zeta)}{\partial z} = \eta\left(\frac{\partial^2 \zeta}{\partial \rho^2} + \frac{1}{\rho}\frac{\partial \zeta}{\partial \rho} - \frac{\zeta}{\rho^2} + \frac{\partial^2 \zeta}{\partial z^2}\right), \tag{2.5}$$

[1] Since the density is taken to be unity, the pressure and the reduced pressure, which is found by dividing the pressure by the density, are the same.

where we have set $u_\vartheta = 0$ due to the swirl-free assumption and derivatives with respect to θ equal to zero by axisymmetry.

It is possible to define a Stokes streamfunction Ψ such that

$$u_\rho = -\frac{1}{\rho}\frac{\partial \Psi}{\partial z}, \qquad u_z = \frac{1}{\rho}\frac{\partial \Psi}{\partial \rho}. \tag{2.6}$$

The vector potential $\mathbf{A} = \frac{1}{\rho}\Psi\hat{\vartheta}$, where $\hat{\vartheta}$ is a unit vector in the same direction as the polar angle ϑ.

2.1 Short time asymptotics

In this section, we consider the case that the vortex ring is in fact a vortex filament, where the vorticity has not had time to diffuse outside of a narrow ring. Let R_0 be the initial radius of the vortex ring, and let σ be the radius of the filament, with $\sigma \ll R_0$. Also, let Γ_0 be the initial circulation of the vortex ring. The situation is modeled in Figure 2.1.

Lord Kelvin (1867), in a note added to Tait's translation (Tait, 1867) of Helmholtz's original paper on vorticity (Helmholtz, 1858), gave a formula without justification for the velocity W of such a vortex ring:

$$W \sim \frac{\Gamma_0}{4\pi R_0}\left(\log\frac{8R_0}{\sigma} - \frac{1}{4}\right), \qquad \frac{\sigma}{R_0} \ll 1. \tag{2.7}$$

Helmholtz (1858) had found the same formula (except for the determination of the constant $-1/4$) by performing the crude approximation that

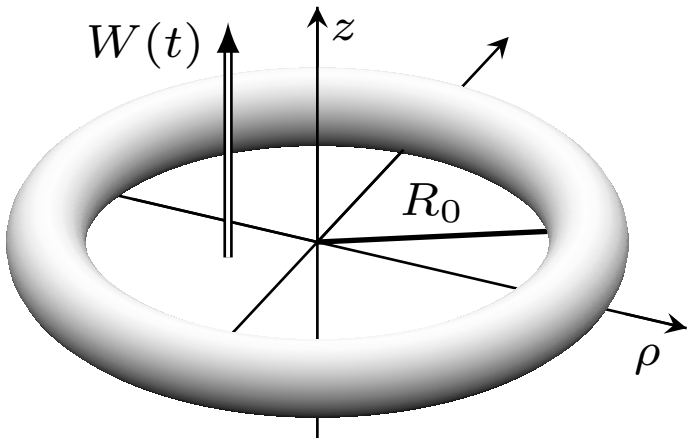

Figure 2.1: Diagram of an early-stage vortex ring.

$U \approx H/(2I)$, where H is the total kinetic energy of the fluid and I is the magnitude of the hydrodynamic impulse Fukumoto (2010).

Equation (2.7) was rederived by Saffman (1970) using the Helmholtz-Lamb transformation, first used by Lamb (1932) for the study of discrete vortices. The general idea is to derive an expression for the moments of vorticity and then take a derivative in time in order to obtain the velocity of the vortex ring as a whole structure. Let u'_ρ, u'_z be the velocity in the frame of the vortex ring (so $u'_\rho = u_\rho$ and $u'_z = u_z - W$).

Saffman begins his argument with the identity

$$\begin{aligned}\zeta\rho(zu'_\rho - \rho u'_z) &= 3\rho z u'_\rho \zeta - \left(2\rho z u'_\rho \zeta + \rho^2 z \frac{\partial u'_\rho}{\partial \rho}\zeta + \rho^2 z u'_\rho \frac{\partial \zeta}{\partial \rho}\right) \\ &\quad - \left(\rho^2 u'_z \zeta + \rho^2 z \frac{\partial u'_z}{\partial z}\zeta + \rho^2 z u'_z \frac{\partial \zeta}{\partial z}\right) \\ &= 3\rho z u'_\rho \zeta - \frac{\partial}{\partial \rho}\left(\rho^2 z u'_\rho \zeta\right) - \frac{\partial}{\partial z}\left(\rho^2 z u'_z \zeta\right), \end{aligned} \tag{2.8}$$

which is evident after accounting for incompressibility (2.1) and the inviscid steady-state evolution of vorticity given by (2.5) after setting the quantities $\frac{\partial \zeta}{\partial t} = \eta = 0$. Then

$$\int_V u'_z \hat{z} \cdot (\mathbf{r} \times \zeta \hat{\theta}) \, dV = 2\pi \int_A (\rho^2 u'_z \zeta - \rho z u'_\rho \zeta) \, dA = -6\pi \int_A \rho z u'_\rho \zeta \, dA, \quad (2.9)$$

where V is the full volume of the fluid, and A is the ρz-plane. Equation (2.8) provides the second equality, since the integral over the plane of the derivatives is zero by the boundary conditions.

Now let (s, θ) represent local polar coordinates within the cross-section of the filament located in the ρz-plane. It is now possible to substitute $\rho = R_0$, $z = s\cos\theta$, $\zeta = \zeta_0(s)$, and $u'_\rho = \frac{\Gamma_0 \Gamma(s)}{2\pi s} \cos\theta$ into (2.9), so that

$$\int_V u'_z \hat{z} \cdot (\mathbf{r} \times \zeta \hat{\theta}) \, dV = -\tfrac{3}{4} R_0 \Gamma_0^2 \left(1 + O(\sigma/R_0)\right). \quad (2.10)$$

Now note that the kinetic energy of the fluid is

$$E = \int_V \tfrac{1}{2} \mathbf{u}^2 \, dV = 2WI + \int_V u'_z \hat{z} \cdot (\mathbf{r} \times \zeta \hat{\theta}) \, dV, \quad (2.11)$$

where $I = \pi R_0^2 \Gamma_0 (1 + O(\sigma/R_0))$ is the hydrodynamic impulse. An integration by parts reveals that

$$E = \pi \int_A \zeta \Psi \, dA \sim \tfrac{1}{2} \Gamma_0^2 R_0 (\log 8 - 2) + \tfrac{1}{2} \Gamma_0^2 R_0 \left(\int_0^\sigma \Gamma(s)^2 \frac{ds}{s} - \log \frac{\sigma}{R_0} \right), \quad (2.12)$$

where

$$\Gamma(s) = \frac{2\pi}{\Gamma_0}\int_0^s s'\zeta_0(s')\,ds', \qquad \Gamma(\sigma) = 1. \tag{2.13}$$

Now it is possible to substitute all the found values into (2.11) to solve for W:

$$W \sim \frac{\Gamma_0}{4\pi R_0}\left(\log 8 - \tfrac{1}{2} + \int_0^\sigma \Gamma(s)^2\frac{ds}{s} - \log\frac{\sigma}{R_0}\right). \tag{2.14}$$

If one assumes uniform vorticity, Saffman (1970) concludes the argument by noting that $\Gamma(s) = s^2/\sigma^2$ results in Kelvin's formula (2.7). Saffman's approach has the added benefit that it can provide an accurate estimation of W even when the vorticity is not uniform. Then Kelvin's constant of $-1/4$ may no longer be accurate.

The above results all assume an inviscid flow. In the presence of diffusion, however, a true filament with $\sigma = 0$ initially will widen with time: $\sigma \sim \sqrt{4\eta t}$. Using a small modification of the Helmholtz-Lamb transformation, Saffman (1970) found that

$$W(t) \sim \frac{\Gamma_0}{4\pi R_0}\left(\log\frac{8R_0}{\sqrt{4\eta t}} - \frac{1-\gamma+\log 2}{2}\right), \qquad \frac{\eta t}{R_0^2} \ll 1, \tag{2.15}$$

where γ is the Euler-Mascheroni constant.

2.2 Long time asymptotics

Diffusion eventually causes the vortex ring to grow in size and slow down, with the Reynolds number decaying to zero as well. Then the inertia and

pressure terms of the Navier-Stokes equations can be ignored, so that, approximately,

$$\frac{\partial \mathbf{u}}{\partial t} = \eta \nabla^2 \mathbf{u}. \tag{2.16}$$

Phillips (1956) performed a multipole expansion of the solution, assuming an initial hydrodynamic impulse $\mathbf{I}$. To leading order (and correcting the leading coefficient),

$$\mathbf{u}(\mathbf{r}, t) \sim \frac{1}{2\pi^{3/2} r^3} \left(\left(\frac{3\pi^{1/2}}{2} \operatorname{erf}(\xi) - (2\xi^2 + 3)\xi e^{-\xi^2} \right) \frac{\mathbf{r} \cdot \mathbf{I}}{r^2} \mathbf{r} + \left((2\xi^2 + 1)\xi e^{-\xi^2} - \frac{\pi^{1/2}}{2} \operatorname{erf}(\xi) \right) \mathbf{I} \right), \tag{2.17}$$

where $r = |\mathbf{r}|$ and $\xi = r/\sqrt{4\eta(t - t_0)}$, for some time t_0 after which (2.16) is valid. Note that this has no swirl, so when the impulse $\mathbf{I} = I\hat{\mathbf{z}}$ is in the $\hat{\mathbf{z}}$-direction, the streamfunction can be written as

$$\Psi \sim \frac{I}{2\pi^{3/2}} \left(\frac{\pi^{1/2}}{2} \operatorname{erf}(\xi) - \xi e^{-\xi^2} \right) \frac{\rho^2}{r^3} \tag{2.18}$$

(Fukumoto and Kaplanski, 2008).

As in the previous section, we can make use of the Helmholtz-Lamb transformation to compute the velocity of the vortex ring, this time using a slightly different (yet equivalent) formulation (Fukumoto, 2010). The z-component of the vorticity centroid is given by

$$Z(t) = \int \zeta \rho^2 z \, dA \Big/ \int \zeta \rho^2 \, dA \tag{2.19}$$

(we integrate over $0 \leqslant \rho < \infty, -\infty < z < \infty$). The denominator is (proportional to) the hydrodynamic impulse (i.e., the total z-momentum), which is constant. Thus, when we take a derivative with respect to time, we get

$$W(t) = \dot{Z}(t) = \int \dot{\zeta}\rho^2 z \, dA \Big/ \int \zeta\rho^2 \, dA. \tag{2.20}$$

We can now use (2.5) to remove the time derivative. Noting that the viscous terms from that equation should integrate out to zero, we have that

$$\begin{aligned} W(t) &= \int -(\frac{\partial}{\partial\rho}(u_\rho\zeta) + \frac{\partial}{\partial z}(u_z\zeta))\rho^2 z \, dA \Big/ \int \zeta\rho^2 \, dA \\ &= \int (2\rho z u_\rho\zeta + \rho^2 u_z\zeta) \, dA \Big/ \int \zeta\rho^2 \, dA. \end{aligned} \tag{2.21}$$

In the second equality, we integrated by parts. Boundary conditions are such that the boundary terms all go to zero.

Now using (2.18) to compute the velocity and vorticity, (2.21) can be computed directly. This was done by Rott and Campbell (1993), who found that

$$W(t) \sim \frac{7I}{15(8\pi\eta t)^{3/2}}, \tag{2.22}$$

which they claim has been verified numerically to four significant figures.

2.3 Model viscous vortex ring

In this section, we follow a derivation by Fukumoto and Kaplanski (2008) which starts with a vortex filament at time $t = 0$ and follows the evolution over time through the final viscous decay as $t \to \infty$.

In order to solve (2.5), assume that we are at small Reynolds number, so the unsteady Stokes equations are a good approximation (at least for short times). Ignoring the nonlinear terms, the solutions with the correct boundary conditions all have the form $\zeta = e^{-(k^2+p^2)\eta t} e^{ikz} J_1(p\rho)$, where $p \geqslant 0$, k is an real value, and J_1 is a Bessel function of the first kind. Allowing an arbitrary superposition of such solutions,

$$\zeta(\rho, z, t) = \int_{-\infty}^{\infty} \int_{0}^{\infty} a(k, p) e^{-(k^2+p^2)\eta t} e^{ikz} J_1(p\rho)\, dp\, dk. \tag{2.23}$$

The coefficient $a(k, p)$ can be determined using the Fourier-Bessel theorem by plugging in the initial condition $\zeta(\rho, z, 0) = \zeta_0(\rho, z)$:

$$a(k, p) = \frac{p}{2\pi} \int_{-\infty}^{\infty} \int_{0}^{\infty} \zeta_0(\rho, z) e^{ikz} J_1(p\rho) \rho\, d\rho\, dz. \tag{2.24}$$

Now assume we start with a true filament, i.e., $\zeta_0(\rho, z) = \Gamma_0 \delta(\rho - R_0)\delta(z)$, where Γ_0 is the initial circulation and R_0 is the initial radius of the vortex ring. Then

$$a(k, p) = \frac{\Gamma_0 R_0}{2\pi} p J_1(pR_0), \tag{2.25}$$

so

$$\begin{aligned}\zeta(\rho,z,t) &= \frac{\Gamma_0 R_0}{2\pi}\int_{-\infty}^{\infty}\int_0^{\infty} e^{-(k^2+p^2)\eta t}e^{ikz}J_1(p\rho)J_1(pR_0)p\,dp\,dk \\ &= \frac{\Gamma_0 R_0}{4\pi^{1/2}(\eta t)^{3/2}}\exp\left(-\frac{z^2+\rho^2+R_0^2}{4\eta t}\right)I_1\left(\frac{R_0\rho}{2\eta t}\right), \qquad (2.26)\end{aligned}$$

where I_1 is a modified Bessel function of the first kind. Similarly,

$$\begin{aligned}\Psi(\rho,z,t) &= \int_{-\infty}^{\infty}\int_0^{\infty}\frac{a(k,p)}{k^2+p^2}e^{-(k^2+p^2)\eta t}e^{ikz}J_1(p\rho)\rho\,dp\,dk \\ &= \frac{\Gamma_0 R_0\rho}{2\pi}\int_{-\infty}^{\infty}\int_0^{\infty}\frac{p}{k^2+p^2}e^{-(k^2+p^2)\eta t}e^{ikz}J_1(p\rho)J_1(pR_0)\,dp\,dk \\ &= \frac{\Gamma_0 R_0\rho}{4}\int_0^{\infty}\left[e^{pz}\mathrm{erfc}\left(\frac{2p\eta t+z}{2\sqrt{\eta t}}\right)\right. \qquad (2.27)\\ &\qquad\left. +e^{-pz}\mathrm{erfc}\left(\frac{2p\eta t-z}{2\sqrt{\eta t}}\right)\right]J_1(p\rho)J_1(pR_0)\,dp,\end{aligned}$$

where recall that erfc is the complimentary error function. Note that the expressions for ζ and Ψ are both computed in the frame of reference of the laboratory, but with the origin shifted so as to always be at the very center of the vortex ring. Figure 2.2 (left) shows the contours of Ψ, while the contours on the right show the usual elliptical body (circular here) of the vortex ring (usually taken to correspond to $\Psi \geqslant 0$). To obtain the streamfunction on the right, $\frac{1}{2}\rho^2 W$ must be subtracted from Ψ in (2.27) to subtract the velocity of the vortex ring and enter into the comoving frame.

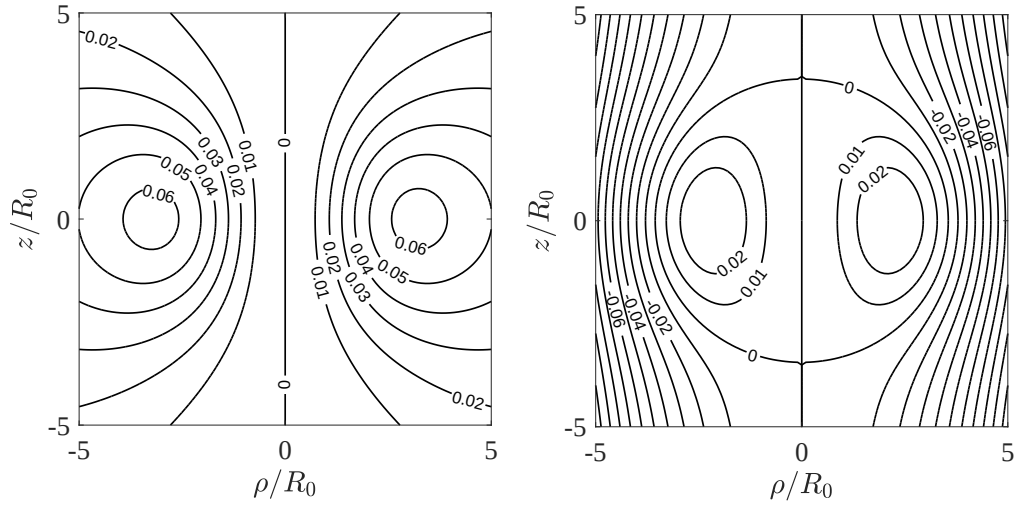

Figure 2.2: (Left) Contours of the streamfunction Ψ normalized by $\Gamma_0 R_0$ in the lab frame from Eq. (2.27) at time $t = R_0^2/\eta$. (Right) The same normalized streamfunction in a frame moving with the vortex ring.

The circulation Γ can also be solved for as a function of time:

$$\Gamma(t) = \Gamma_0 \left[1 - \exp\left(-\frac{R_0^2}{4\eta t}\right)\right]. \tag{2.28}$$

And although the circulation decays over time, a consequence of vorticity diffusing and canceling over the line $\rho = 0$, the total hydrodynamic impulse of the vortex ring is constant:

$$I = \pi \int_0^\infty \int_{-\infty}^\infty \zeta \rho^2 \, dz \, d\rho = \pi R_0^2 \Gamma_0. \tag{2.29}$$

Fukumoto and Kaplanski (2008) also find the total energy of the vortex

ring:

$$E_1(t) = \pi \int_0^\infty \int_{-\infty}^\infty \zeta \Psi \, dz \, d\rho = \frac{I^2}{3(8\pi\eta t)^{3/2}} \, {}_2F_2\left(\frac{3}{2}, \frac{3}{2}; \frac{5}{2}, 3; -\frac{R_0^2}{2\eta t}\right), \quad (2.30)$$

where ${}_2F_2$ is a generalized hypergeometric function. This expression has asymptotic forms

$$E_1(t) \sim \begin{cases} \Gamma_0^2 R_0 (\frac{1}{4} \log(8R_0^2/\eta t) + \frac{1}{4}\gamma - 1), & t \downarrow 0, \\ I^2/3(8\pi\eta t)^{3/2}, & t \to \infty \end{cases} \quad (2.31)$$

(Morrell et al., 2019). Note that each of these limits is integrable, so it makes sense to consider the total action of the vortex ring, which will be significant when considering a suspension of vortices:

$$\mathcal{E}_1 = \int_0^\infty E(t) \, dt = \frac{I^2}{6\pi^2 \eta R_0} = \tfrac{1}{6} Re^2 \eta R_0^3, \quad (2.32)$$

where $Re := \Gamma_0/\eta$ is the Reynolds number.

As in the previous sections, the Helmholtz-Lamb transformation can be applied to solve for the velocity of the vortex as a full structure. Fukumoto and Kaplanski (2008) find that

$$W(t) = \frac{1}{2I} \left(7E_1(t) - \frac{3\pi}{\eta t} \int_0^\infty \int_{-\infty}^\infty z^2 \zeta \Psi \, dz \, d\rho \right). \quad (2.33)$$

After much tedious algebra, they find the expression

$$W(t) = \frac{I}{6(8\pi\eta t)^{3/2}}\left[{}_2F_2\left(\frac{3}{2},\frac{3}{2};\frac{5}{2},3;-\frac{R_0^2}{2\eta t}\right) - \frac{36}{5}\,{}_2F_2\left(\frac{3}{2},\frac{5}{2};2,\frac{7}{2};-\frac{R_0^2}{2\eta t}\right) + \frac{72\eta t}{R_0^2}\exp\left(-\frac{R_0^2}{4\eta t}\right) I_1\left(\frac{R_0^2}{4\eta t}\right)\right]. \tag{2.34}$$

For $\eta t \ll R_0^2$, (2.34) has asymptotic expansion

$$W(t) \sim \frac{\Gamma_0}{4\pi R_0}\left\{\log\left(\frac{4R_0}{\sqrt{\eta t}}\right) - \frac{1-\gamma+\log 2}{2} - \frac{9}{2}\left[\log\left(\frac{4R_0}{\sqrt{\eta t}}\right) - \frac{2-\gamma+\log 2}{2}\right]\frac{\eta t}{R_0^2} + \frac{105}{32}\left(\frac{\eta t}{R_0^2}\right)^2\right\}, \tag{2.35}$$

which agrees with (2.15). For $\eta t \gg R_0$, on the other hand,

$$W(t) \sim \frac{7I}{240\sqrt{2}(\pi\eta t)^{3/2}}\left\{1 - \frac{33}{196}\frac{R_0^2}{\eta t} + \frac{125}{6272}\left(\frac{R_0^2}{\eta t}\right)^2\right\}, \tag{2.36}$$

which perfectly extends (2.22).

Fukumoto and Kaplanski (2008) use (2.34) to compute the total self-advection of the vortex ring, which is now only possible to do analytically because of the existence of a formula for the velocity which is uniformly valid in time. The distance $S(t)$ traveled by the vortex ring after its creation

is

$$S(t) = \int_0^t W(\tau)\,d\tau = \frac{5\Gamma_0 R_0}{24\pi\eta}\left\{1 - \frac{\sqrt{2\pi}R_0}{20\sqrt{\eta t}}\left[{}_2F_2\left(\frac{1}{2},\frac{3}{2};\frac{5}{2},3;-\frac{R_0^2}{2\eta t}\right)\right.\right.$$
$$\left. - \frac{36}{5}\,{}_2F_2\left(\frac{1}{2},\frac{5}{2};2,\frac{7}{2};-\frac{R_0^2}{2\eta t}\right)\right] - \frac{3\sqrt{2\pi\eta t}}{5R_0}\exp\left(-\frac{R_0^2}{4\eta t}\right)$$
$$\left.\times\left[\frac{R_0^2}{\eta t}I_0\left(\frac{R_0^2}{4\eta t}\right) + \left(\frac{R_0^2}{\eta t} - 2\right)I_1\left(\frac{R_0^2}{4\eta t}\right)\right]\right\}. \qquad (2.37)$$

Note in particular that even after an infinite amount of time, the vortex ring only drifts a finite distance, which is proportional to the Reynolds number and the size of the vortex ring, as should be expected:

$$S(\infty) = \frac{5\Gamma_0 R_0}{24\pi\eta} = \frac{5}{24\pi}\mathrm{Re}R_0. \qquad (2.38)$$

This is in stark contrast to two dimensions, where a vortex dipole self-advects an infinite distance, with $W \sim 1/t$ as $t \to \infty$ (Rott and Campbell, 1993), so $S \sim \log t$ grows without bound, albeit very slowly.

It is of note that Fukumoto and Kaplanski validate their model against experimental data, finding excellent agreement for the vorticity distribution against data collected by Cater et al. (2004) at Reynolds number $\mathrm{Re} = 2000$. Since the model velocity W agrees well with both short and long asymptotic results found in earlier sections, this model should describe vortex rings rather well at low to intermediate Reynolds number.

At higher Reynolds number, Maxworthy (1972) observed experimentally that vortices are unstable, breaking apart into in time $O(R_0^2/\eta)$ and

then reforming larger, slower vortex rings at lower Reynolds number. This model should be a valid description of the motion of the vortex both before and after the instability, although different values of Γ_0 and R_0 are required for the time chunks before and after the break up occurs so as to preserve the impulse (2.29), which is conserved.

2.4 Moments of the velocity of the fluid surrounding a single vortex ring

In this section, we follow the arguments of Morrell et al. (2019) to determine which moments of the velocity field in the fluid surrounding the vortex ring exist. The exact streamfunction (2.27) will not be required, as the approximation (2.18) is valid asymptotically far away from the vortex ring for all time and near the vortex ring for large times, and close to the vortex ring at short times it will be possible to derivate estimates for the moments by approximating the circular vortex filament as a line vortex.

The velocity field (2.17) can be simplified by breaking spacetime into two parts: one with $\xi \gtrsim 1$, corresponding to the far-field of the vortex ring, before diffusion has caused the vortex to expand into that space, and the other with $\xi \lesssim 1$, which contains the long-time behavior of the fluid after the vortex ring has diffused to contain that region of space. In the

corresponding limits,

$$\mathbf{u}(\rho, z, t) = \begin{cases} \dfrac{\Gamma_0 R_0^2 \, \hat{\mathbf{z}}}{12\sqrt{\pi}(\eta t)^{3/2}} & \xi \lesssim 1, \\ \dfrac{\Gamma_0 R_0^2 [(2z^2 - \rho^2) \, \hat{\mathbf{z}} + 3z\rho \, \hat{\boldsymbol{\rho}}]}{4(z^2 + \rho^2)^{5/2}} & \xi \gtrsim 1, \end{cases} \qquad \frac{R_0}{\sqrt{4\eta t}} \ll \max(\xi, 1) \,, \tag{2.39}$$

with a relatively sharp transition region around the viscous front $\xi = 1$. Note that although the two parts of (2.39) were derived in the asymptotic regimes where $\xi \ll 1$ and $\xi \gg 1$, respectively, they are good approximations for most points (see Figure 2.3), except for at small times and in an annulus surrounding the viscous front $0.4 \lesssim \xi \lesssim 2.5$. Note that the large ξ approximation matches the flow for an inviscid vortex ring, while fluid inside the vortex ring mostly moves uniformly, so viscous stresses are only significant in this transition region.

Velocity field (2.39) is nice in that it allows us to easily see that for positions far enough away from the vortex ring, the velocity drops off as r^{-3} (recall that $r = \sqrt{z^2 + \rho^2}$) as $r \to \infty$, while at any fixed location, after the "diffusive front" (i.e., the transition region around $\xi = 1$) hits, the velocity starts to decay like $t^{-3/2}$. This decay happens uniformly with position (within the region $\xi \lesssim 1$), so all the material inside the diffusive front moves as a uniform growing and slowing ball.

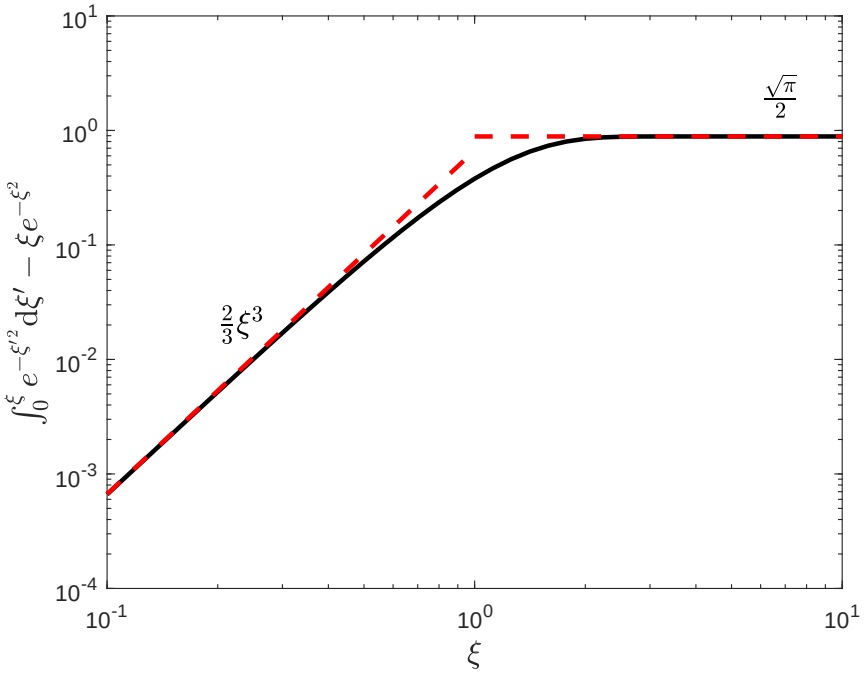

Figure 2.3: Plot of the terms involving ξ inside the parentheses of (2.18), along with the small and large ξ approximations used to derive (2.39). We see that the approximations are very good outside of a transition region with $0.4 \lesssim \xi \lesssim 2.5$.

Now we begin the computation of moments. Let

$$M_n := \int_0^\infty \int_V |\mathbf{u}|^n \, dV \, dt, \tag{2.40}$$

be the n^{th}-moment of the velocity, integrated over time and space. Here, V is our domain, in this section taken to be $\mathbb{R}^3$. At the outset, it is not clear which moments exist, if any, and we shall see that many do not. Because the velocity scales as $1/r^3$ as $r \to \infty$, integrating (2.40) over space, we find

that

$$\int_V |\mathbf{u}|^n \, dV = \int_V |\mathbf{u}|^n r^2 \, dr \, d\Omega \tag{2.41}$$

is infinite for $2 - 3n \geqslant -1$, where $d\Omega$ denotes integration over the unit sphere. Therefore, $M_n = \infty$ for all $n \leqslant 1$, and for $n > 1$, the approximation (2.39) enables us to compute the integral explicitly. Asymptotically, we find that

$$\int_V |\mathbf{u}|^n \, dV = O(\Gamma_0^n (\eta t)^{3(1-n)/2}), \tag{2.42}$$

valid as $t \to \infty$.

Another possible source of moment divergence lies at time $t = 0$, when the velocity field is singular at the vortex filament. For small times, the evolution of vorticity near a point on the vortex ring may be studied using a line vortex approximation. Consider therefore a line vortex located at the origin; the vorticity ζ is the Green's function for the heat equation multiplied by the initial circulation:

$$\zeta = \frac{\Gamma_0}{4\pi\eta t} \exp\left(-\frac{x^2 + y^2}{4\eta t}\right). \tag{2.43}$$

Then the swirl velocity is

$$u = \frac{\Gamma_0}{2\pi\sqrt{x^2 + y^2}} \left[1 - \exp\left(-\frac{x^2 + y^2}{4\eta t}\right)\right], \tag{2.44}$$

counterclockwise around the origin. The velocity decays exponentially quickly far away, so we only need consider the near field (out to a distance

proportional to $\sqrt{4\eta t}$) when determining the spatial moments. Near the vortex, $u \approx \Gamma_0\sqrt{x^2+y^2}/8\pi\eta t$. Integrating, we find that

$$\int |\mathbf{u}|^n \, dA = O(\Gamma_0^n (\eta t)^{1-n/2}), \tag{2.45}$$

valid as $t \downarrow 0$, is finite for all nonnegative n and strictly positive t, so the vortex filament does not contribute to any possible divergence of the spatial moment for any $n \geqslant 0$ (except for possibly at the single time $t = 0$).

Looking across the entirety of the spatial domain, the arguments above suggest the existence of the spatial moments $\int_V |\mathbf{u}|^n \, dV$ at all positive t for all $n > 1$, but we are particularly interested in the moments M_n, which are integrals over both space and time. Examining the rate of decay of (2.42) for large times results in infinite moment M_n precisely when $3(1-n)/2 \geqslant -1$, or $n \leqslant \frac{5}{3}$. Similarly, the behavior of (2.45) at small times results in infinite moment M_n when $1 - n/2 \leqslant -1$, or $n \geqslant 4$. Thus, the moments of $\mathbf{u}$ exist only for $\frac{5}{3} < n < 4$.

Of particular note, recall that the action $\mathcal{E}_1 = \frac{1}{2}M_2$ is finite.

2.5 Entrainment

We finish this chapter with a brief description of the movement of individual tracer particles under the influence of a viscous vortex ring.

Note that the $\xi \gtrsim 1$ case of (2.39) is the velocity field of a potential

dipole oriented in the $+\hat{\mathbf{z}}$-direction, so particles in the far field can be thought of as being pushed out from in front of the vortex ring, backwards around the sides as it passes, and then pulled along behind the vortex ring.

As the vortex ring grows under diffusion, particles which were in the far field are eventually absorbed into the vortex ring through its expanding boundary. During this period, the velocity transitions from the potential dipole characteristic of $\xi \gtrsim 1$ to the uniform flow characteristic of $\xi \lesssim 1$ (after enough expansion has occurred that the particle finds itself close to the center of the vortex, relative to the size of the vortex ring).

In the final stage of motion, particles move uniformly in the $+\hat{\mathbf{z}}$-direction, along with the vortex ring. However, individual particles move faster than the vortex ring itself. The ratio of the fluid speed in the $\xi \lesssim 1$ limit with the speed of the vortex ring asymptotes to

$$\frac{u(\mathbf{x},t)}{W(t)} \longrightarrow \frac{\dfrac{\Gamma_0 R_0^2}{12\sqrt{\pi}(\eta t)^{3/2}}}{\dfrac{7\pi\Gamma_0 R_0^2}{15(8\pi\eta t)^{3/2}}} = \frac{20\sqrt{2}}{7} \approx 4.0406 \tag{2.46}$$

as $t \to \infty$. Therefore, fluid in the center of the vortex ring moves about four times faster than the vortex ring itself, and is pulled up through the middle of the vortex from the back to the front, while fluid near the front of the vortex ring is pushed out of the way, towards the sides of the structure,

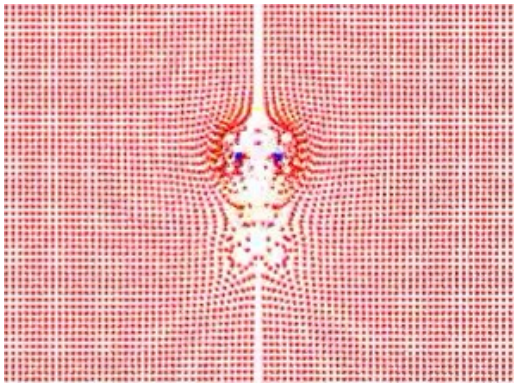

Figure 2.4: A snapshot of the vortex ring early on in its development. We can see the makings of a small tail behind the vortex ring where particles are pulled into the center and up towards the vortex ring.

where fluid is generally moving slower than the vortex ring itself. This motion causes fluid to swirl around a center of vorticity in the ρz-plane, although relatively few rotations should be observed in practice since the growth and slowdown of the vortex ring each make it harder for fluid to complete a full rotation about the vorticity centroid. Only particles which were entrained into the vortex ring very early on are able to complete multiple rotations.

We finish our discussion of entrainment with several diagrams demonstrating the evolution of a particle field as described above. Figures 2.4-2.7 are stills of an initially uniform cross-section of particles under the influence of a single vortex ring oriented in the upwards direction. In each, the red dots are individual tracer particles, while the blue dots denote the center of vorticity in the ρz-plane. The faint yellow circle denotes the boundary of the vortex ring ($\Psi = 0$ in the comoving frame of the vortex

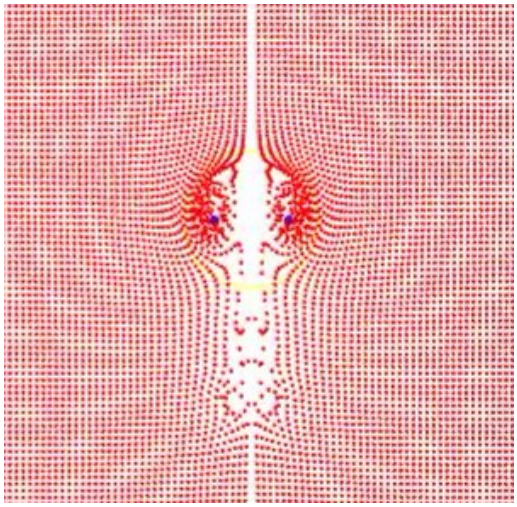

Figure 2.5: A somewhat later snapshot of the same vortex ring. We can see the tail has enlarged somewhat, and can also more clearly see that fluid is pulled up through the back of the vortex ring towards the front, where it is then pushed to the side.

ring), which roughly corresponds with the viscous front $\xi = 1$.

In Figure 2.4, one can see lots of particles bunched near the forward boundary of the vortex ring (and fewer behind) as particles initially inside the vortex ring are pulled up through the center and pushed out towards the sides, while fluid just outside the vortex ring is pushed out of the way. The "tail" that appears behind the vortex ring is the region the vortex ring has passed through en route to its current position. Particles can only enter this region if they are pulled in from the sides.

Figure 2.5 shows a snapshot a little later in time. We see that the tail has elongated as the vortex ring has moved further along, and signs of fluid being pulled up into the vortex ring from behind are indicated by the

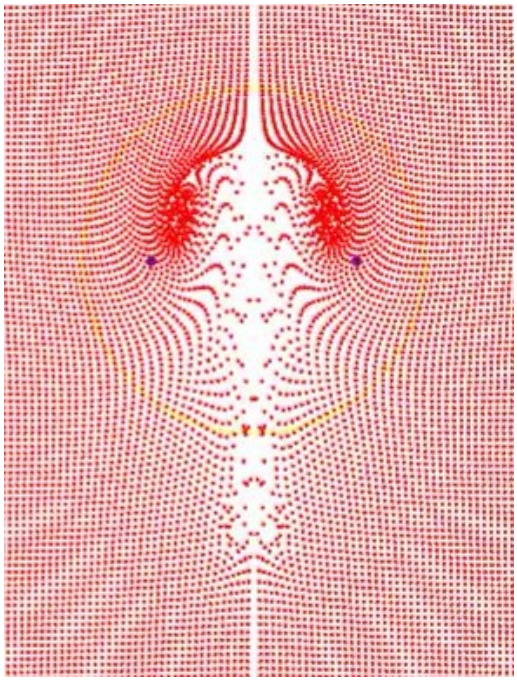

Figure 2.6: A later snapshot of the vortex ring. We start to see the center of vorticity move in the $+\hat{\boldsymbol{\rho}}$-direction, while individual fluid particles do not necessarily follow. The particles which were entrained early on are seen to collect near the front middle of the vortex ring.

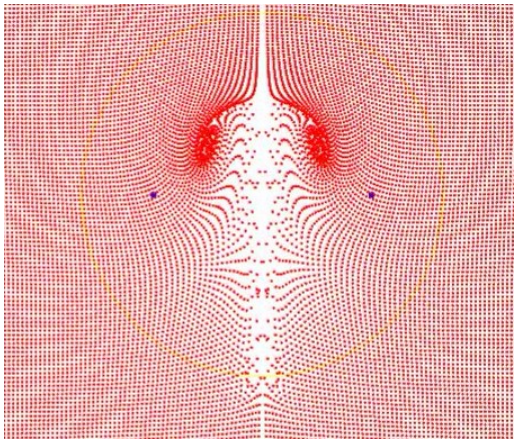

Figure 2.7: A much later snapshot of the vortex ring.

shape of the line of particles in that location. These signs are confirmed in Figure 2.6, where we also see an additional band of fluid being pulled up through the center of the vortex ring, this time from the interior of the vortex ring after making a full revolution around the vorticity centroid. We can also see that the vorticity centroid has moved outwards and that the vortex ring has expanded. The particles which started in the core of the young vortex ring are located ahead of the vorticity centroid, and are radially closer to the center line $\rho = 0$ as well.

Finally, Figure 2.7 shows the vortex ring and particles at a much later time in the development of the vortex ring, after it has had a chance to decay substantially. Qualitatively, there is very little difference between this and the previous figure, except that the vorticity centroid has moved further out radially and the vortex ring has expanded much further. So we see that fluid can enter the vortex ring through the sides, as well as from being pulled in from behind at earlier times. Although the fluid along the central axis moves faster than the vortex ring itself, we see that the rate of expansion of the size of the vortex ring is increasing, while particles within the vortex ring are slowing, so no fluid actually exits the vortex ring through the front.

3 DISTRIBUTION OF THE VELOCITY FIELD FOR A DILUTE SUSPENSION OF VISCOUS VORTEX RINGS

In this chapter we study the velocity distribution in a dilute suspension of viscous vortex rings, closely following Morrell et al. (2019). We assume some mechanism, such as a colony of jellyfish, generates vortices randomly throughout time and space, as observed and illustrated in Figure 3.1. These vortices decay due to viscosity but are replenished such that the system is assumed to reach a statistical equilibrium, containing vortices with some age distribution. Turbulence has been modeled with some success using vortex rings (Synge and Lin, 1943; Phillips, 1956; Saffman, 1997), but here we investigate a moderate Reynolds number regime which is still a long way from turbulence (the jellyfish are assumed to be a few centimeters in size so that the rings they generate are strongly affected by viscosity). Other related biological systems may also exhibit related velocity field fluctuations that may have important functional consequences. In particular, nonmotile pulsing corals share considerable hydrodynamic similarities with undulating jellyfish, and their repeated pulsing is known to contribute to fluid mixing, nutrient transport, and the rate of photosynthesis at intermediate Reynolds numbers (Hamlet et al., 2012; Kremien et al., 2013; Samson et al., 2017). A better understanding of the velocity fluctuations in suspensions may also be of use in the design of biomimetic systems for related purposes (Villanueva et al., 2011; Colin et al., 2012;

Figure 3.1: (Left) A "suspension" of spotted jellyfish (*Mastigias papua*) at the Vancouver Aquarium. (Center) Fast swimming *Nemopsis bachei* expels a single vortex ring with each rapid pulse (reproduced with permission from Dabiri et al. (2006)). (Right) Schematic of the problem: we seek the distribution of the fluid velocity $\mathbf{u}$ at $\mathbf{r}_0$ due to a randomly distributed suspension of viscous vortex rings in three dimensions.

Nawroth et al., 2012),

One key to developing analytical estimates for velocity fluctuations is to start with a tractable 'building block,' in this case a simple model for a vortex ring. There exists a great wealth of literature containing analytical, numerical, and experimental results for vortex rings (Maxworthy, 1972; Cantwell and Rott, 1988; Stanaway et al., 1988; Shariff and Leonard, 1992; Saffman, 1992; Cater et al., 2004; Fukumoto and Kaplanski, 2008; Fukumoto, 2010; Dabiri and Gharib, 2004; Dabiri, 2006; Shadden et al., 2006; Delbende and Rossi, 2009), but to study the role of viscous vortex decay, a classical ideal vortex model is insufficient. Instead, we shall use an intermediate-Reynolds number model of a decaying vortex ring due to Fukumoto and Kaplanski (2008).

In the following pages we show analytically and verify numerically that the probability distribution for the velocity fluctuations of a dilute suspension of vortex rings is a truncated 5/3-stable distribution (1.1). These

results are robust in the sense that any flow produced by impulses sufficiently localized in both space and time will produce the same velocity distribution. The variance of u (mean energy) is shown to be linear in the vortex volume fraction ϕ as expected from such a superposition of individual velocity fields. However, the width of the core scales as $\phi^{3/5}$ rather than $\phi^{1/2}$, suggesting that the tails of the distribution contribute at leading-order to the energy.

The chapter is structured as follows. In Section 3.1, we build a suspension of viscous vortices by superimposing the flow fields of individual model vortex rings (see Sections 2.3-2.4), and we subsequently derive an estimate for the energy of the suspension. This analysis is expanded in Section 3.2 to determine the full velocity distribution analytically. These findings are confirmed numerically using simulations involving the evaluation of transient velocity fields over multiple scales. We show in Section 3.3 that under a particular set of conditions, the $|u|^{-8/3}$ power law observed in the distribution is robust and is a consequence of swimming occurring in a three-dimensional fluid. This enables a brief discussion of how the distribution changes for a force dipole, quadrupole, etc. in Section 3.4. Concluding remarks are given in Section 3.5.

3.1 Energy of a suspension of viscous vortices

In this section we find an analytical estimate for the energy of a suspension of viscous vortices, which will be used in the analysis of the full velocity distribution. Vortex rings are assumed to come into being uniformly in time, space, and orientation, into an otherwise quiescent infinite bath. The rate of vortex production is μ vortices per unit time per unit volume, which when nondimensionalized becomes an effective volume fraction $\phi := \mu R_0^5/\eta$. Since vortices decay over time, there is a natural correspondence between vortex production and volume fraction. Note that with a high enough rate of production, ϕ can be greater than one. This is not unphysical, as vortices can overlap.

In nature, concentrations *Aurelia aurita* jellyfish have been observed in the range of 1×10^{-6} to 3×10^{-4} medusae per cubic centimeter with mean radius R_0 ranging from 0.125 cm to 2.7 cm depending on the time of year (Olesen et al., 1994). Meanwhile, McHenry and Jed (2003) found that jellyfish pulsed at a rate of once per second for smaller medusae, and once per two seconds for larger medusae. We therefore estimate that, for the suspension of vortices, ϕ ranges from 3×10^{-8} in early spring to 0.3 in late summer. Thus, we will assume that $\phi \ll 1$, and therefore that any vortex-vortex interactions are negligible.

Consider the velocity field $\mathbf{v}(\mathbf{r}, t) = \rho^{-1} \boldsymbol{\nabla}^{\perp} \Psi$, with $\boldsymbol{\nabla}^{\perp} = \hat{\mathbf{z}}\, \partial_\rho - \hat{\boldsymbol{\rho}}\, \partial_z$, for a vortex initially at the origin and pointing in the $\hat{\mathbf{z}}$ direction as in

Figure 2.2. Rotating and translating the velocity to represent a vortex with arbitrary position and direction, we first obtain the rotated velocity field

$$\mathbb{Q} \cdot \mathbf{v}\big(\mathbb{Q}^{-1} \cdot \mathbf{r}, t\big), \tag{3.1}$$

where $\mathbb{Q}$ is a rotation matrix, and then translate the field to point $\mathbf{R}$ (replacing $\mathbf{r}$ by $\mathbf{r} - \mathbf{R}$):

$$\mathbb{Q} \cdot \mathbf{v}\big(\mathbb{Q}^{-1} \cdot (\mathbf{r} - \mathbf{R}), t\big). \tag{3.2}$$

Writing the vortex position in time as

$$\mathbf{R}(t) = \mathbf{R}(0) + S(t)\, \mathbb{Q} \cdot \hat{\mathbf{z}}, \qquad S(0) = 0, \tag{3.3}$$

(recall that $S(t)$ is the vortex displacement (2.37) and $W(t) = S'(t)$ is the speed (2.34)), thus results in its induced velocity field

$$\mathbb{Q} \cdot \mathbf{v}\big(\mathbb{Q}^{-1} \cdot (\mathbf{r} - \mathbf{R}(0)) - \hat{\mathbf{z}} S(t)\,,\, t\big)\,. \tag{3.4}$$

Summing the velocity contributions at a point $\mathbf{r}_0$ from N independent vortices, which are initially located at random points $\mathbf{R}_k$, results in

$$\mathbf{U} = \sum_{k=1}^{N} \mathbb{Q}_k \cdot \mathbf{v}\big(\mathbb{Q}_k^{-1} \cdot (\mathbf{r}_0 - \mathbf{R}_k) - \hat{\mathbf{z}}\, S(T_k)\,, T_k\big)\,, \tag{3.5}$$

where the random variable T_k denotes the age of the kth vortex, and $\mathbb{Q}_k$ is a random rotation matrix, which enforces isotropy. We assume $N = \mu V \tau$

is constant, where V is the total volume of the domain and τ is the lifetime of a vortex. Here, V, τ are assumed finite, but we will examine the infinite volume and time limits shortly.

The expected value of $\mathbf{U}$, $\langle \mathbf{U} \rangle$, averaged over all positions, orientations, and birth times, is

$$\langle \mathbf{U} \rangle = N \int_{\Omega} \int_{0}^{\tau} \int_{V} \mathbb{Q} \cdot \mathbf{v}\big(\mathbb{Q}^{-1}(\Omega) \cdot (\mathbf{r}_0 - \mathbf{r}) - \hat{\mathbf{z}}\, S(t)\,,\, t\big)\, \frac{dV_{\mathbf{r}}}{V} \frac{dt}{\tau} \frac{d\Omega}{4\pi}, \quad (3.6)$$

with Ω the solid angle that determines the rotation matrix. With the change of variables

$$\mathbf{r}' = \mathbb{Q}^{-1}(\Omega) \cdot (\mathbf{r}_0 - \mathbf{r}) - \hat{\mathbf{z}}\, S(t), \qquad t' = t, \quad (3.7)$$

we have $\partial \mathbf{r}'/\partial \mathbf{r} = -\mathbb{Q}^{-1}(\Omega)$, and $\partial \mathbf{r}'/\partial t = -W(t)\hat{\mathbf{z}}$. The Jacobian matrix for the transformation is

$$\frac{\partial(\mathbf{r}', t')}{\partial(\mathbf{r}, t)} = \begin{pmatrix} -\mathbb{Q}^{-1}(\Omega) & -W(t)\hat{\mathbf{z}} \\ 0 & 1 \end{pmatrix} \quad (3.8)$$

with determinant -1, so the Jacobian does not modify the integral:

$$\langle \mathbf{U} \rangle = N \int_{\Omega} \int_{0}^{\tau} \int_{V'(\mathbf{r}_0, t', \Omega)} \mathbb{Q} \cdot \mathbf{v}(\mathbf{r}', t') \frac{dV_{\mathbf{r}'}}{V} \frac{dt'}{\tau} \frac{d\Omega}{4\pi}. \quad (3.9)$$

Here $V'(\mathbf{r}_0, t', \Omega)$ is the domain of integration transformed according to (3.7).

Similarly, the qth absolute moment of $\mathbf{U}$ can be computed as

$$\langle |\mathbf{U}|^q \rangle = N \int_\Omega \int_0^\tau \int_V |\mathbf{v}(\mathbf{r}', t')|^q \frac{dV_{\mathbf{r}'}}{V} \frac{dt'}{\tau} \frac{d\Omega}{4\pi}. \tag{3.10}$$

Integrating over the orientation angles and dropping the primes,

$$\begin{aligned} \langle |\mathbf{U}|^q \rangle &= N \int_0^\tau \int_V |\mathbf{v}(\mathbf{r}, t)|^q \frac{dV_{\mathbf{r}}}{V} \frac{dt}{\tau} \\ &= \mu \int_0^\tau \int_V |\mathbf{v}(\mathbf{r}, t)|^q dV_{\mathbf{r}}\, dt. \end{aligned} \tag{3.11}$$

Setting $q = 2$, taking $V = \mathbb{R}^3$ and $\tau \to \infty$ (and dividing by two), we find the expectation of the energy

$$\langle E \rangle = \tfrac{1}{2}\mu \int_0^\tau \int_V |\mathbf{v}(\mathbf{r}, t)|^2 dV_{\mathbf{r}} dt = \mu \mathcal{E}_1 = \frac{\phi}{6} \frac{\Gamma_0^2}{R_0^2}. \tag{3.12}$$

Thus, the expected energy is μ times (2.32), the energy of a single vortex integrated over time and space. This is reasonable: in this noninteracting dilute limit, the energy of the system is the sum of the energies of the individual vortices.

3.2 Velocity distribution

A more refined analysis than that of Section 3.1 allows us to characterize the entire velocity distribution, rather than just the moments. This clarifies whether the dominant contribution to the moments arises from

near or far field dynamics, as well as facilitating potential comparisons to experiments. For small concentrations, we will find stable distributions similar to Zaid et al. (2011) or Zaid and Mizuno (2016) for suspensions of microswimmers, though the relationship between spatial velocity decay and the tail exponents is modified here by the additional temporal behavior of the vortices.

Single vortex

We first consider the velocity distribution due to a single vortex ring, which will be used in Section 3.2 to derive the marginal distribution for the velocity fluctuations in a suspension of viscous vortices. We choose a random point $\mathbf{r} = \mathbf{r}_0 + (\rho\cos\theta, \rho\sin\theta, z)$ uniformly inside the ball $V = B_L(\mathbf{r}_0)$ of radius L centered at $\mathbf{r}_0$, and choose a random vortex age t uniformly in $[0, \tau]$. The probability density function $p_{U^1}(u)$ for the magnitude of the single-vortex velocity $U^1 = |\mathbf{U}^1|$ is

$$p_{U^1}(u) = \int_0^\tau \int_V \delta(u - \nu(\mathbf{r}, t)) \frac{dV_\mathbf{r}}{V} \frac{dt}{\tau} \tag{3.13}$$

where $\nu(\mathbf{r}, t) = |\mathbf{v}(\mathbf{r}, t)|$. The delta function constrains the integral to a hypersurface $\nu(\mathbf{r}, t) = u$:

$$p_{U^1}(u) = \frac{1}{V\tau} \int_{\nu(\mathbf{r},t)=u} \frac{1}{|\boldsymbol{\nabla}_{(\mathbf{r},t)}\nu(\mathbf{r}, t)|} \, dS_{\mathbf{r},t} \tag{3.14}$$

where $|\boldsymbol{\nabla}_{(\mathbf{r},t)}\nu(\mathbf{r},t)|$ is a Jacobian (Hörmander, 1983) and $dS_{\mathbf{r},t}$ is the integration element on the hypersurface $\nu(\mathbf{r},t) = u$. An analytical estimate may be achieved by splitting the integral into two pieces, $\xi \leqslant 1$ and $\xi \geqslant 1$ with $\xi = |\mathbf{r}|/\sqrt{4\eta t}$, and using (2.39), valid for small u, to approximate the velocity. (We neglect the transition region near $\xi = 1$.)

For $\xi \leqslant 1$, the velocity is only a function of the time t. Inverting the expression to write t as a function of the velocity u, $t = (\Gamma_0 R_0^2/12u\sqrt{\pi}\eta^{3/2})^{2/3}$, so

$$\int\limits_{\nu(\mathbf{r},t)=u,\,\xi\leqslant 1} \frac{dS_{\mathbf{r},t}}{|\boldsymbol{\nabla}_{(\mathbf{r},t)}\nu(\mathbf{r},t)|} = \tfrac{4}{3}\pi(4\eta t)^{3/2}\left(\frac{\Gamma_0 R_0^2}{8\sqrt{\pi}\eta^{3/2}t^{5/2}}\right)^{-1}\Bigg|_{t=\left(\frac{\Gamma_0 R_0^2}{12u\sqrt{\pi}\eta^{3/2}}\right)^{2/3}}$$
$$= \frac{2^{8/3}\pi^{1/6}}{3^{11/3}}\frac{\Gamma_0^{5/3}R_0^{10/3}}{\eta}\,u^{-8/3}. \tag{3.15}$$

The integral for $\xi \geqslant 1$ is somewhat more complicated. From (2.39), we see that

$$\nu = \frac{\Gamma_0 R_0^2}{r^3}\frac{\sqrt{1+3\cos^2\theta}}{4} =: \frac{\Gamma_0 R_0^2}{r^3}f(\theta), \tag{3.16}$$

where θ is the angle from the positive z-axis. When the velocity is u, $r = (\Gamma_0 R_0^2 f(\theta)/u)^{1/3}$. Then

$$\int\limits_{\nu(\mathbf{r},t)=u,\xi\geqslant 1} \frac{dS_{\mathbf{r},t}}{|\boldsymbol{\nabla}_{(\mathbf{r},t)}\nu(\mathbf{r},t)|} = \int_0^{\pi}\int_0^{r_u(\theta)^2/4\eta}\left(\frac{u}{r_u(\theta)}\sqrt{9+\frac{f'(\theta)^2}{f(\theta)^2}}\right)^{-1} \tag{3.17}$$
$$\times\, 2\pi r_u(\theta)\sqrt{r_u(\theta)^2 + r_u'(\theta)^2}\sin\theta\,dt\,d\theta,$$

where we have parameterized our surface in θ, φ, t and performed the integral over φ. The integral in (3.17) can be computed analytically:

$$\frac{2\pi}{4\eta u}\int_0^\pi \frac{r_u(\theta)^4\sqrt{r_u(\theta)^2+r_u'(\theta)^2}}{\sqrt{9f(\theta)^2+f'(\theta)^2}} f(\theta)\sin\theta\,d\theta \tag{3.18}$$
$$= \frac{\pi}{6}\frac{\Gamma_0^{5/3}R_0^{10/3}}{\eta}\,u^{-8/3}\int_0^\pi f(\theta)^{13/3}\sin\theta\,d\theta = 0.01453\frac{\Gamma_0^{5/3}R_0^{10/3}}{\eta}\,u^{-8/3}.$$

By combining Eqs. (3.15) and (3.18), we find that

$$p_{U^1}(u) \lesssim \frac{0.1514}{V\tau}\frac{\Gamma_0^{5/3}R_0^{10/3}}{\eta}\,u^{-8/3}, \qquad \varepsilon \ll \frac{uR_0}{\Gamma_0} \ll 1, \tag{3.19}$$

where

$$\varepsilon = \frac{R_0^3}{\min(V,(\eta\tau)^{3/2})}. \tag{3.20}$$

The approximation breaks down as $(uR_0/\Gamma_0) \uparrow 1$ because then the details of the near field of the vortex become important, and we cannot use (2.39) to go from (3.14) to (3.19) as we did above. The approximation (3.19) also breaks down as $(uR_0/\Gamma_0) \downarrow \varepsilon$ because, at fixed V and τ, the region $\nu(\mathbf{r},t) < \varepsilon\Gamma_0/R_0$ falls outside the domain of integration in (3.13). The value of ε is typically small, indicating a wide range of validity for (3.19), as long as the domain radius L is much larger than the vortex size R_0, and the time of integration τ is much longer than the viscous dissipation time R_0^2/η.

In order to probe the accuracy of this approximation, we computed (3.13) via Monte Carlo integration, finding the velocity at a point $\mathbf{r}_0$ using a second-order finite difference approximation of (2.27) for a single vortex

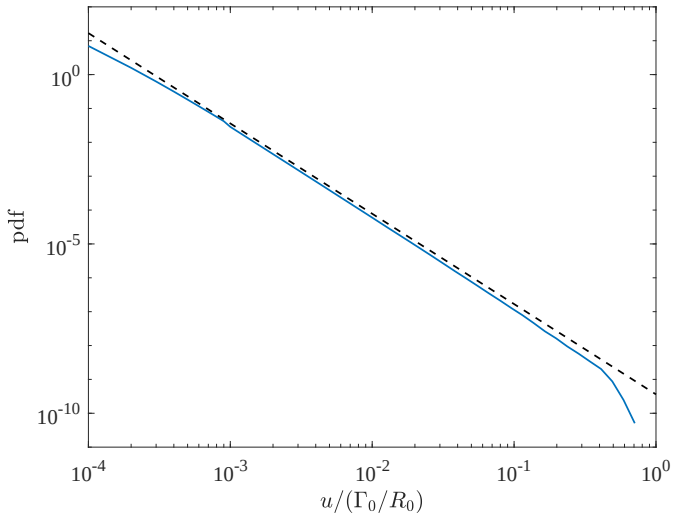

Figure 3.2: The numerically evaluated velocity probability density function for a single vortex ring (solid line) compared with the analytic approximation (3.19) (dashed line). The approximation is about 40% higher than the numerical values on the segment with $0.001\Gamma_0/R_0 \lesssim u \lesssim 0.04\Gamma_0/R_0$.

ring (see the subsection on numeric results later in this section for more details) positioned randomly in $B_L(\mathbf{r}_0)$ with $\Gamma_0 = 100\eta$, $L = 100\,R_0$, and $\tau = 100\,R_0^2/\eta$, and continuing to sample until the distribution converged. Figure 3.2 shows a comparison between the numerical computation of (3.13) and the analytical approximation (3.19). We see that the $u^{-8/3}$ power law holds over a wide range of values of u. The analytical prediction (3.19) is about 40% too large when compared with the numerics due to the transition region around $\xi \approx 1$. However, this error does not affect the exponent in the $-8/3$ power law, just the prefactor.

Suspension of vortices

We now use the velocity distribution for a single vortex ring to determine the corresponding distribution for a suspension of vortices, modifying the argument of Thiffeault (2015) that characterized the drifts associated with microswimmers. We will use components of the velocity instead of its magnitude, since components can be added together but not magnitudes. This additivity of velocity is a good approximation at low volume fractions ϕ. Since we have assumed isotropy of the suspension, there is no loss in generality in considering only a single component of the fluid velocity $\mathbf{u}$.

Starting from the single-vortex distribution $p_{U^1}(u)$ for the magnitude of velocity, Eq. (3.13), we convert to the distribution for the components with

$$p_{\mathbf{U}^1}(\mathbf{u}) = p_{\mathbf{U}^1}(\mathbf{u}|u)\, p_{U^1}(u) = \int_V \int_0^\tau \frac{\delta(u - v(\mathbf{r},t))}{4\pi u^2}\, \frac{dt}{\tau}\, \frac{dV_\mathbf{r}}{V}, \qquad u = |\mathbf{u}|, \tag{3.21}$$

where, due to the isotropy of $\mathbf{u}$, the conditional probability $p_{\mathbf{U}^1}(\mathbf{u}|u) = 1/4\pi u^2$ is the uniform distribution on the sphere of radius u. We then find the marginal distribution for the x-component of $\mathbf{u}$, denoted by u_x:

$$\begin{aligned} p_{U^1_x}(u_x) &= \int_{-\infty}^{\infty}\int_{-\infty}^{\infty} p_{\mathbf{U}^1}(\mathbf{u})\, du_y du_z \\ &= \int_V \int_0^\tau \int_{-\infty}^{\infty}\int_{-\infty}^{\infty} \frac{\delta(u - v(\mathbf{r},t))}{4\pi u^2}\, du_y\, du_z\, \frac{dt}{\tau}\, \frac{dV_\mathbf{r}}{V}, \end{aligned} \tag{3.22}$$

where the superscript 1 on U_x^1 and $\mathbf{U}^1$ is a reminder that this is still for a single vortex. Carrying out the integrals over u_y and u_z yields

$$p_{U_x^1}(u_x) = \int_V \int_0^\tau \frac{1}{2\nu(\mathbf{r},t)} \left[\nu^2(\mathbf{r},t) > u_x^2\right] \frac{dt}{\tau} \frac{dV_\mathbf{r}}{V}, \tag{3.23}$$

where $[A]$ is the indicator function of A, defined as 1 if A is true, and 0 otherwise.

In order to determine the distribution for multiple vortex rings, we compute the characteristic function

$$\langle e^{ikU_x^1} \rangle = \int_{-\infty}^{\infty} p_{U_x^1}(u_x)\, e^{iku_x}\, du_x = \int_V \int_0^\tau \operatorname{sinc}(k\nu(\mathbf{r},t)) \frac{dt}{\tau} \frac{dV_\mathbf{r}}{V}, \tag{3.24}$$

where $\operatorname{sinc}(x) := \sin x/x$ for $x \neq 0$ and $\operatorname{sinc}(0) := 1$. We find that

$$\langle e^{ikU_x^1} \rangle = 1 - \frac{\gamma(k)}{V\tau}, \tag{3.25}$$

where

$$\gamma(k) := \int_V \int_0^\tau \{1 - \operatorname{sinc}(k\nu(\mathbf{r},t))\}\, dt\, dV_\mathbf{r}\,. \tag{3.26}$$

Recall that μ is the constant rate of production of vortex rings, per unit space and time. Hence, after a time τ we have $N = \mu V\tau$ independent vortex rings, which together induce a random velocity U_x^N at the origin.

The random variable U_x^N has characteristic function

$$\langle e^{ikU_x^N} \rangle = \langle e^{ikU_x^1} \rangle^N = \left(1 - \frac{\gamma(k)}{V\tau}\right)^{\mu V\tau} \sim \exp\left(-\mu\gamma(k)\right) \tag{3.27}$$

as $V, \tau \to \infty$ (Thiffeault, 2015). Therefore, for the suspension of vortices, the probability density function of velocities is obtained from the inverse Fourier transform

$$p_{U_x}(u_x) = \frac{1}{2\pi} \int_{-\infty}^{\infty} \exp(-\mu\gamma(k))\, e^{-iku_x} dk, \tag{3.28}$$

where we have dropped the superscript $N \to \infty$ on U_x.

Since $1 - \operatorname{sinc}(x) \sim \frac{1}{6}x^2$ as $x \to 0$, we have $\gamma(k) \sim \frac{1}{3}\mathcal{E}_1 k^2$ as $k \to 0$, from which we can solve for an approximate velocity distribution, mathematically valid as $\phi = \mu R_0^5/\eta \gg 1$:

$$p_{U_x}(u_x) \approx \sqrt{\frac{3}{4\pi\mu\mathcal{E}_1}}\, \exp\left(-\frac{3u_x^2}{4\mu\mathcal{E}_1}\right), \tag{3.29}$$

consistent with the central limit theorem. Then $\langle u_x^2 \rangle = \frac{2}{3}\langle E \rangle = \frac{2}{3}\mu\mathcal{E}_1$, as predicted by (3.12). Recall that technically ϕ can be greater than one, since vortices can overlap. Of course, in the limit of large ϕ our linear superposition assumption breaks down, so (3.29) is unlikely to be observed in practice.

To find an approximation of the probability density function which is valid for small ϕ, where our model applies, we can use the probability

distribution $p_{U^1}(u)$ from (3.19) to find an approximation of γ which is valid for large k in the limit as $V, \tau \to \infty$, by way of a change of variables to transform (3.26) into an integral over u:

$$\gamma(k) = V\tau \int_0^\infty \{1 - \operatorname{sinc}(ku)\}\, p_{U^1}(u)\, du \sim 0.1096\, \frac{\Gamma_0^{5/3} R_0^{10/3}}{\eta} |k|^{5/3} =: \frac{a}{\mu} |k|^{5/3} \tag{3.30}$$

(with $a = 0.1096\, \mu(\Gamma_0 R_0^2)^{5/3}/\eta = 0.1096\, (\Gamma_0/R_0)^{5/3}\phi$), where we have compensated for the uniform 40% overestimate of $p_{U^1}(u)$ by (3.19), as observed in Figure 3.2 by decreasing the prefactor to match numerical estimates. We can compute (3.28) analytically using this γ; the result is a $\frac{5}{3}$-stable distribution (1.5). For larger u_x, $\Phi_{5/3}(u_x; a)$ has tails

$$p_{U_x}(u_x) \sim \frac{1}{2\pi}\, \Gamma\left(\tfrac{8}{3}\right) a\, |u_x|^{-8/3}, \qquad \phi^{3/5} \ll \frac{u_x R_0}{\Gamma_0} \ll 1, \tag{3.31}$$

while for small u_x the core region is reasonably well approximated by a Gaussian

$$p_{U_x}(u_x) \sim 0.2844 a^{-3/5} \exp\left(-u_x^2/3.198 a^{6/5}\right), \qquad \frac{u_x R_0}{\Gamma_0} \ll \phi^{3/5}. \tag{3.32}$$

These forms come into alignment using asymptotic matching when $u_x \propto a^{3/5}$. Of particular note, we see here that the width of the core scales as $\phi^{3/5}$. Contrasting these last two equations with the Gaussian distribution (3.29), it is clear that (3.31) and (3.32) are only valid when $\phi \ll 1$; that is, even though (3.32) resembles a Gaussian distribution, it is completely

different from the Gaussian (3.29) in the large ϕ limit. Moreover, the tail distribution (3.31) contributes heavily to the energy $\mu\mathcal{E}_1$, which therefore cannot be deduced from the width of (3.32).

The $-8/3$ power law in (3.31) does not persist for arbitrarily large u_x, and in fact one can show using an argument similar to that in the previous subsection that $p_{U_x}(u_x) \propto |u_x|^{-5}$ as $|u_x| \to \infty$ due to the singular behavior of a vortex ring at $\rho = R_0$ and $t = 0$. Including the large u behavior in our calculations changes the distribution from a stable distribution to a truncated stable distribution, which has finite second moment (and thus finite energy). This observation explains the seemingly inconsistent large and small ϕ approximations for $p_{U_x}(u_x)$ of a Gaussian and a non-Gaussian stable distribution, respectively. The transition from a truncated stable distribution to a Gaussian distribution occurs near a volume fraction where the width of the core region is on the same order of magnitude as the cutoff, which follows immediately from the Berry–Esséen theorem (Shlesinger, 1995).

A further discussion of the relative contributions of the core and the tails to the energy, both with and without truncation, is warranted. The expected energy of the suspension of vortices is

$$\langle E \rangle = \tfrac{3}{2} \int_{-\infty}^{\infty} u_x^2 \, p_{U_x}(u_x) du_x. \tag{3.33}$$

Equations (3.31) and (3.32) cannot be used by themselves to approximate

the energy, since this results in divergence in the expression above, so the $|u_x|^{-5}$ tails for the largest velocities must be included in order to obtain a convergent integral.

Using (3.31)–(3.32) to determine the behavior of the inner and middle regions, we find that

$$p_{U_x}(u_x) \approx \begin{cases} 0.2844a^{-3/5}\exp\left(-u_x^2/3.198a^{6/5}\right) & |u_x| \leqslant 3.260a^{3/5}, \\ 0.2395a|u_x|^{-8/3} & 3.260a^{3/5} \leqslant |u_x| \leqslant c, \\ 0.2395ac^{7/3}|u_x|^{-5} & |u_x| \geqslant c, \end{cases} \tag{3.34}$$

where $c \approx 0.4\Gamma_0/R_0$, as in Figure 3.5, and $a = 0.1096\,(\Gamma_0/R_0)^{5/3}\phi$ (from (3.30)). A comparison to (1.5) suggests that (3.34) somewhat underestimates $p_{U_x}(u_x)$ around the transition at $|u_x| = 3.260a^{3/5}$.

Let $\langle E_C\rangle$, $\langle E_{-8/3}\rangle$, and $\langle E_{-5}\rangle$ be the portions of the energy using the approximations of $p_{U_x}(u_x)$ in the core (C), middle ($-8/3$), and outer (-5) regions in (3.34) with the appropriate bounds, so that $\langle E\rangle = \langle E_C\rangle + \langle E_{-8/3}\rangle + \langle E_{-5}\rangle$. We find the contributions

$$\langle E_C\rangle = 1.980a^{6/5}, \tag{3.35a}$$

$$\langle E_{-8/3}\rangle = -3.196a^{6/5} + 2.156ac^{1/3}, \tag{3.35b}$$

$$\langle E_{-5}\rangle = 0.3593ac^{1/3}. \tag{3.35c}$$

Without the underestimate of $p_{U_x}(u_x)$ in the transition between the core

and middle regions, the $a^{6/5}$ terms above should cancel exactly (since the energy is known to scale with ϕ and a is linear in ϕ), which we verified using (1.5) directly and integrating numerically. The lack of exact cancellation is a symptom of our approximations in the transition region. Thus, a rough estimate of the energy is $\langle E \rangle \approx 2.515 a c^{1/3} = 0.2031(\Gamma_0/R_0)^2\phi$, a slight overestimate of the exact expression in (3.12). Hence, we see that the greatest contribution to the energy comes from the middle region of the distribution for small ϕ. As ϕ increases, the largest contribution begins to come from the core region, which encompasses the far-field velocity of the vortices. The transition from the tails contributing most of the energy to the core doing so happens at about the same value of ϕ where the distribution changes shape from a $\frac{5}{3}$-stable distribution to a Gaussian, due to the core width approaching the value of the cutoff between the middle and outer regions of (3.34), which is independent of ϕ.

Comparison with numerical simulations

Since a number of approximations were used to derive the distributions in the previous section, a comparison with numerical simulations is in order. In particular, in computing (3.28) we inserted a cutoff between the $-8/3$ and -5 power laws, and the use of (3.30) is not valid for small k.

Our numerical investigation involves a Monte Carlo integration of (3.22): we simulate the suspension by generating and evolving vortex rings uniformly in time and space in a spherical volume of radius $L = 100R_0$ for

$t \in [0, \tau]$ with $\tau = 100R_0^2/\eta$ and computing the velocity at the origin. We fix the initial single-vortex circulation to be $\Gamma_0 = 100\eta$, so all the vortices have the same initial strength. The velocity field due to individual vortices is obtained by differentiating the streamfunction (2.27) using a fourth-order-accurate finite-difference approximation. The velocity fields of individual vortices are then superimposed linearly to generate the total velocity field. This is a reasonable approximation in the dilute regime, $\phi \ll 1$, when vortices stay far enough apart so that they do not significantly interact.

Because of the special functions and the oscillatory integrand, the streamfunction Ψ is prohibitively expensive to evaluate directly. We compute it for several points on two overlapping grids and form a cubic spline interpolant to evaluate it at arbitrary points in space. One grid covers $\rho, |z| \leqslant 20R_0$ and $0 \leqslant t \leqslant 20R_0^2/\eta$ with 200^3 grid points, while another grid with higher resolution covers $0.75R_0 \leqslant \rho \leqslant 1.25R_0$, $|z| \leqslant 0.25R_0$ and $0 \leqslant t \leqslant 0.5R_0^2/\eta$, with $250^2 \times 100$ grid points around the initial singularity. For points outside these grids, Ψ is approximated using (2.18). Since the interpolated values of Ψ do not match (2.18) on the boundary of the grid, a buffer region is established where Ψ is represented as a convex combination of the interpolated value and (2.18); the smoothness of the transition is important in order to accurately compute the velocity. The integration required to compute Ψ in (2.27) at any particular grid point is performed using a global adaptive quadrature (Matlab's integral function) with absolute and relative error tolerances 10^{-10} and 10^{-6}, respectively. A single

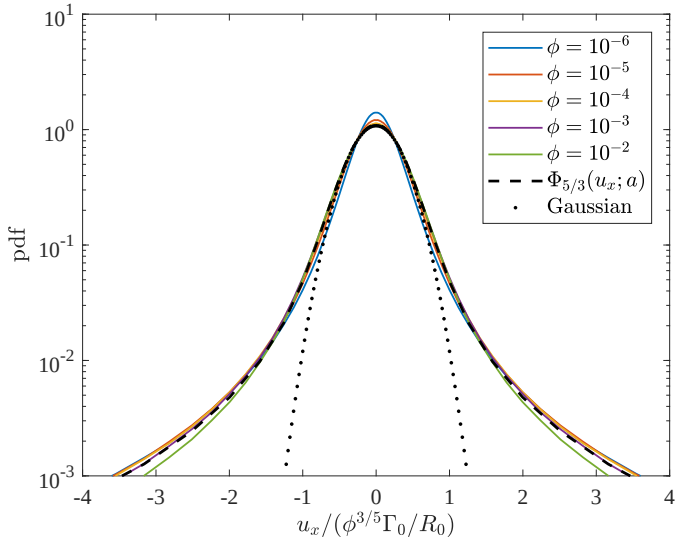

Figure 3.3: The probability density function for the x-component of velocity (normalized by $\phi^{3/5}\Gamma_0/R_0$) for various ϕ. We see that the core scales with $\phi^{3/5}$. The dashed curve is the analytical expression $\Phi_{5/3}(u_x; a)$, which agrees closely with the numerics. The dotted curve is a Gaussian distribution with unit standard deviation, included for reference.

simulation amounts to placing a random distribution of vortices, each with a random position, orientation, and age, and using the machinery above to compute the velocity at the origin at that moment.

For a given value of the effective volume fraction $\phi = \mu R_0^5/\eta$ we run 15 million simulations on a distributed computing framework and then compute the probability density function $p_{u_x}(u_x)$ for a single component of velocity by placing the results in exponentially-sized bins. Figure 3.3 shows this density normalized for a selection of different ϕ, along with the theoretical expression $\Phi_{5/3}(u_x; a)$ as a dashed line and a Gaussian distribution as a dotted line for reference. The numerical simulations

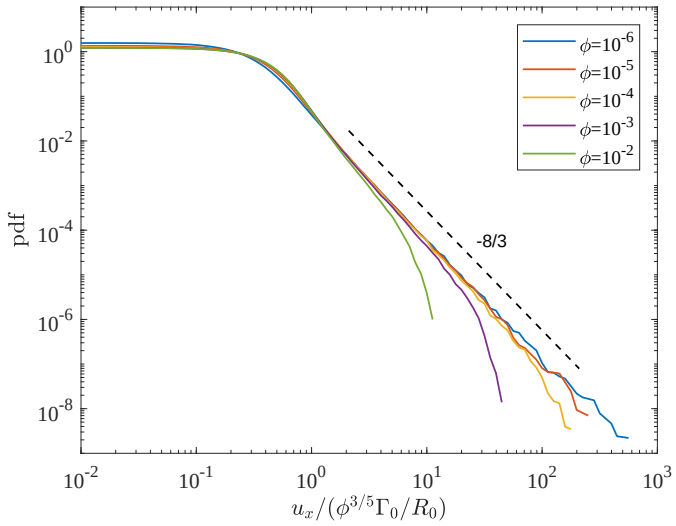

Figure 3.4: The same distributions as in Figure 3.3, but on a log-log scale. The additional dashed line verifies the $-8/3$ power law for large (but not very large) velocities.

appear to confirm the accuracy of this analytic estimate for the entire range of ϕ considered. Note in particular the scaling of the core width as $\phi^{3/5}$. Figure 3.4 shows the same distributions on a log-log scale, with a dashed line of slope $-8/3$ included for reference. The probability density function decays as $|u_x|^{-8/3}$ outside the core, as predicted in (3.31). We were unable to verify the predicted $|u_x|^{-5}$ power law for very large velocities due to the extreme resolution needed near the initial vortex filaments in order to properly capture the largest velocities.

For large enough velocities, the nearest vortex ring determines the velocity at a point, so that the many-vortex probability distribution $p_{U_x}(u_x)$ has the same tails as the single-vortex $p_{U_x^1}(u_x)$. In particular, outside the

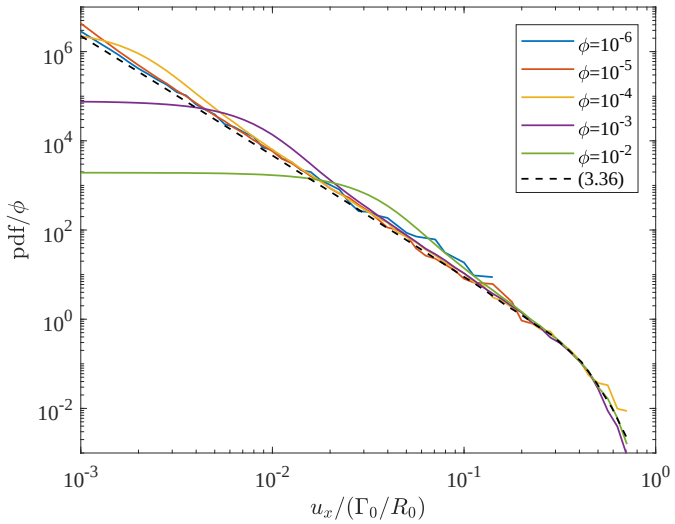

Figure 3.5: Plot of the (normalized) probability density function for the x-component of velocity divided by ϕ compared with (3.36) (the dashed line), showing close agreement, except at small velocities. In particular, regardless of ϕ, the distributions transition away from the $-8/3$ power law at around $u_x \approx 0.4\Gamma_0/R_0$, regardless of ϕ.

core of the distribution we have

$$p_{U_x}(u_x) \sim \phi\, p_{U_x^1}(u_x) = \phi \int_{|u_x|}^{\infty} \frac{p_{U^1}(u)}{2u}\, du, \qquad \frac{u_x R_0}{\Gamma_0} \gg \phi^{3/5}. \tag{3.36}$$

Figure 3.5 compares (3.36) (dashed curve) with PDFs divided by ϕ for several values of ϕ. There is excellent agreement outside the core of the distribution, so typical velocities in the suspension are indeed dominated by the nearest vortex ring except in the case of small velocities.

Figures 3.3–3.5 suggest strongly that $p_{U_x}(u_x)$ is a truncated stable distribution with smooth cutoff near $u_x \approx \pm 0.4\Gamma_0/R_0$. Note that this cutoff is independent of ϕ and only depends on the transition between small

and large u asymptotics for the velocity distribution of a single vortex ring. When $\phi \ll 1$, the cutoff is far down the tail, so a stable distribution is a good approximation for the velocity distribution. A more precise expression for the truncated stable distribution was found (for different α) by Zaid and Mizuno (2016), but as was mentioned in Section 1.3, little is lost by omitting the analytic expression in favor of the above qualitative description of the truncation.

3.3 Robustness

In this section we consider the flow due to an arbitrary impulsive force localized near the origin in time and space and find the same far-field behavior as in the previous section. Thus, the analysis from the last section (except for the large-velocity $|u_x|^{-5}$ tails, which are specific to the vortex model) is generic and carries through to more general flows.

Various aspects of the flow due to an impulsive force have been studied in many contexts (Lamb, 1932; Phillips, 1956; Saffman, 1967, 1970; Bühler, 2007). We follow a combination of Saffman (1967) and Bühler (2007). Consider an external force density

$$\widetilde{\mathbf{F}}(\mathbf{r}, t) = \rho_0 \, \mathbf{F}(\mathbf{r}) \, \frac{1}{\Delta t} \, g(t/\Delta t), \tag{3.37}$$

where ρ_0 is the constant fluid density, $g(s)$ is nonnegative with unit inte-

gral and with support contained in $[0,1]$, and $\mathbf{F}(\mathbf{r})$ has compact support encompassing the origin. For small Δt, a classical argument (see for example Lamb (1932) or Bühler (2007)) shows that the nonlinear terms in the incompressible Navier–Stokes equations are negligible when considering the evolution due to this force of a fluid initially at rest. The pressure $\tilde{p}$ then satisfies a Poisson equation $\nabla^2\tilde{p} = \boldsymbol{\nabla}\cdot\widetilde{\mathbf{F}}$ with boundary condition $\boldsymbol{\nabla}\tilde{p} \to \mathbf{0}$ as $r \to \infty$. Bühler (2007) concludes that $\tilde{p}$ has the same time dependence as $\widetilde{\mathbf{F}}$, i.e.,

$$\tilde{p}(\mathbf{r}, t) = \rho_0\, p(\mathbf{r})\, \frac{1}{\Delta t}\, g(t/\Delta t). \tag{3.38}$$

The linear momentum equation can be integrated over $t \in [0, \Delta t]$, at the end of which

$$\mathbf{v}(\mathbf{r}, \Delta t) + \boldsymbol{\nabla} p(\mathbf{r}) = \mathbf{F}(\mathbf{r}), \tag{3.39}$$

where we neglected the viscous term since it is of order Δt after integration. Far away from the origin, the pressure is harmonic with

$$p(\mathbf{r}) \sim \frac{\mathbf{I}\cdot\mathbf{r}}{4\pi r^3}, \qquad r \to \infty, \quad \text{where} \quad \mathbf{I} = \int_{\mathbb{R}^3} \mathbf{F}(\mathbf{r})\,dV, \tag{3.40}$$

so that $\rho_0\mathbf{I}$ is the total impulsive momentum input (Bühler, 2007). Substituting (3.40) into (3.39), we find that $v(\mathbf{r}, \Delta t) = O(r^{-3})$ in the far field. In fact, for $\mathbf{I} = \pi\Gamma_0 R_0^2\hat{\mathbf{z}}$, the hydrodynamic impulse for the model vortex ring, the velocity $\mathbf{v}(\mathbf{r}, \Delta t)$ found here exactly matches the $\xi \gtrsim 1$ limit of (2.39).

Similarly, we can determine the velocity distribution for long times knowing only the impulse (see for example Phillips (1956) or Saffman (1970)). Taking the curl of (3.39) gives vorticity $\boldsymbol{\omega}(\mathbf{r}, \Delta t) = \boldsymbol{\nabla} \times \mathbf{F}(\mathbf{r})$. Note that $\boldsymbol{\omega}(\mathbf{r}, \Delta t)$ has compact support contained in the support of $\mathbf{F}$. Assume small Reynolds number, in this section defined to be $\mathrm{Re} := R_0 F/\eta$, where F is a characteristic magnitude of $\mathbf{F}$ and R_0 is the radius of the smallest ball containing the support of $\mathbf{F}$. Then the nonlinear term in Navier–Stokes can be neglected, so the vorticity obeys a heat equation

$$\frac{\partial \boldsymbol{\omega}}{\partial t} \approx \eta \nabla^2 \boldsymbol{\omega}, \qquad t > \Delta t, \qquad \boldsymbol{\omega}(\mathbf{r}, \Delta t) = \boldsymbol{\nabla} \times \mathbf{F}(\mathbf{r}). \tag{3.41}$$

In the limit $\Delta t \to 0$, this has solution

$$\boldsymbol{\omega}(\mathbf{r}, t) = \frac{1}{(4\pi\eta t)^{3/2}} \int\limits_{|\mathbf{r}'| \leqslant R_0} [\boldsymbol{\nabla} \times \mathbf{F}(\mathbf{r}')]\ e^{-|\mathbf{r}'-\mathbf{r}|^2/4\eta t} dV_{\mathbf{r}'}. \tag{3.42}$$

For $\eta t \gg R_0 \max(R_0, |\mathbf{r}|)$, we can expand the exponential to obtain

$$\boldsymbol{\omega}(\mathbf{r}, t) = \frac{1}{(4\pi\eta t)^{3/2}} \int\limits_{|\mathbf{r}'| \leqslant R_0} [\boldsymbol{\nabla} \times \mathbf{F}(\mathbf{r}')]\, e^{-|\mathbf{r}|^2/4\eta t} \left(1 - \frac{|\mathbf{r}'|^2 - 2\mathbf{r} \cdot \mathbf{r}'}{4\eta t} + \cdots\right) dV_{\mathbf{r}'}. \tag{3.43}$$

The integral of the first term in the series vanishes; the next order term gives the asymptotic behavior of the vorticity:

$$\boldsymbol{\omega}(\mathbf{r}, t) \sim \frac{\pi}{(4\pi\eta t)^{5/2}}\, e^{-|\mathbf{r}|^2/4\eta t} \int\limits_{|\mathbf{r}'| \leqslant R_0} [\boldsymbol{\nabla} \times \mathbf{F}(\mathbf{r}')] \left(2\mathbf{r} \cdot \mathbf{r}' - |\mathbf{r}'|^2\right) dV_{\mathbf{r}'} \tag{3.44}$$

for $\eta t \gg R_0 \max(R_0, |\mathbf{r}|)$. An integration by parts simplifies the expression:

$$\begin{aligned}\boldsymbol{\omega}(\mathbf{r}, t) &= \frac{2\pi}{(4\pi\eta t)^{5/2}} e^{-|\mathbf{r}|^2/4\eta t} \int\limits_{|\mathbf{r}'|\leqslant R_0} \mathbf{F}(\mathbf{r}') \times (\mathbf{r} - \mathbf{r}') dV_{\mathbf{r}'} \\ &= \frac{2\pi}{(4\pi\eta t)^{5/2}} e^{-|\mathbf{r}|^2/4\eta t} (\mathbf{I} \times \mathbf{r} - \mathbf{J}), \end{aligned} \tag{3.45}$$

where

$$\mathbf{J} := \int\limits_{|\mathbf{r}'|\leqslant R_0} \mathbf{F}(\mathbf{r}') \times \mathbf{r}' dV_{\mathbf{r}'}. \tag{3.46}$$

The corresponding velocity field can be found via the Biot–Savart law:

$$\mathbf{v}(\mathbf{r}, t) = \frac{1}{2(4\pi\eta t)^{5/2}} \int\limits_{\mathbb{R}^3} \frac{(\mathbf{I} \times \mathbf{r}_0 - \mathbf{J}) \times (\mathbf{r} - \mathbf{r}_0)}{|\mathbf{r} - \mathbf{r}_0|^3} e^{-|\mathbf{r}_0|^2/4\eta t} dV_{\mathbf{r}_0}. \tag{3.47}$$

As $t \to \infty$, a vanishingly small error is introduced replacing $\mathbf{r}_0$ by $\mathbf{r} - \mathbf{r}_0$ in the exponential. Then

$$\begin{aligned}\mathbf{v}(\mathbf{r}, t) &\sim \frac{1}{2(4\pi\eta t)^{5/2}} \int\limits_{\mathbb{R}^3} \frac{(\mathbf{I} \times (\mathbf{r}_0 - \mathbf{r}) + (\mathbf{I} \times \mathbf{r} - \mathbf{J})) \times (\mathbf{r} - \mathbf{r}_0)}{|\mathbf{r} - \mathbf{r}_0|^3} e^{-|\mathbf{r} - \mathbf{r}_0|^2/4\eta t} dV_{\mathbf{r}_0} \\ &= \frac{\mathbf{I}}{12(\pi\eta t)^{3/2}}. \end{aligned} \tag{3.48}$$

This matches the $\xi \lesssim 1$ limit of (2.39) perfectly for the hydrodynamic impulse of the model vortex ring.

So we see that in the limit as $r \to \infty$, the velocity decays as $O(r^{-3})$, and for any fixed location, the velocity decays as $O(t^{-3/2})$ as $t \to \infty$. The

transition between these two regimes occurs along the same viscous front as we have already analyzed for the vortex ring ($\xi = 1$). Indeed, (2.39) is a good approximation for the velocity away from the impulse for any flow due to a localized impulsive force. Therefore, all our analysis from the previous section carries through and so $\Phi_{5/3}(u_x; a)$ is an excellent approximation of the velocity distribution for a volume of fluid containing any swimmers that exert force in short bursts, such as for instance copepods (Jiang and Strickler, 2007; Jiang and Kiørboe, 2011).

3.4 Multipole expansion

The previous analysis considered a force monopole isolated in space and time, but it is also possible to consider force dipoles, quadrupoles, etc. Initially, the velocity in the far-field decays as

$$\mathbf{v}(\mathbf{r}, t) = O(r^{-2-n}), \qquad r \to \infty, \tag{3.49}$$

where $n = 1$ for a force monopole, $n = 2$, for a dipole, etc. Repeating the argument from Section 3.3, one can then derive that

$$\mathbf{v}(\mathbf{r}, t) = O(t^{-1-n/2}), \qquad t \to \infty. \tag{3.50}$$

The discussion of the diffusive front remains unchanged: the velocity in the far field transitions from (3.49) to (3.50) at time $t \sim r^2/4\eta$.

As in (3.14),

$$p_{U^1}(u) = \frac{1}{V\tau}\int_{v(\mathbf{r},t)=u} \frac{1}{|\boldsymbol{\nabla}_{(\mathbf{r},t)}v(\mathbf{r},t)|}\,dS_{\mathbf{r},t}. \tag{3.51}$$

For the $\xi \gtrsim 1$ limit, the gradient is purely in the radial direction, at least in the limit of (3.49). In particular, $|\boldsymbol{\nabla}_{(\mathbf{r},t)}v(\mathbf{r},t)|^{-1} = O(r^{3+n})$. Since $u = O(r^{-2-n})$, $r = O(u^{-1/(2+n)})$. Therefore, $|\boldsymbol{\nabla}_{(\mathbf{r},t)}v(\mathbf{r},t)|^{-1} = O(u^{-(3+n)/(2+n)})$. Furthermore, the surface of integration is a sphere of radius r in space and an interval of width $O(r^2)$ in time, for a total three-dimensional measure of magnitude $O(r^4) = O(u^{-4/(2+n)})$. Therefore, the $\xi \gtrsim 1$ contribution to (3.51) scales like $O(u^{-1-5/(2+n)})$.

For the $\xi \lesssim 1$ limit, the gradient is purely in the time direction (in the limit (3.50)). Then $|\boldsymbol{\nabla}_{(\mathbf{r},t)}v(\mathbf{r},t)|^{-1} = O(t^{2+n/2}) = O(u^{-(n+4)/(n+2)})$ (since $u = O(t^{-1-n/2})$ implies that $t = O(u^{-2/(2+n)})$). The surface of integration is the ball of radius $r = \sqrt{4\eta t} = O(u^{-1/(2+n)})$, so the $\xi \lesssim 1$ contribution to (3.51) scales like $O(u^{-1-5/(2+n)})$, just as in the other limit.

As in Section 3.2, the above limits each correspond to the small u limit. Therefore, we can conclude that

$$p_{U^1}(u) \sim u^{-1-5/(2+n)}, \qquad u \to 0. \tag{3.52}$$

Going through the same procedure as Section 3.2 results in the conclusion that p_{U^x} follows a (truncated) $\frac{5}{2+n}$-stable distribution. Rushkin et al. (2010) found that the corresponding distribution for microswimmers is a $\frac{3}{n}$-stable

distribution (for $n \geqslant \frac{3}{2}$; the distribution is Gaussian for $n < \frac{3}{2}$), so we see that the effect of diffusion on the stability parameter α is to add two to both the numerator and denominator.

3.5 Discussion

We analyzed the flow field of a model viscous vortex ring and found that for a flow which is initially a vortex filament, the absolute moments of velocity M_n are finite only for $\frac{5}{3} < n < 4$. Consistent with this observation, the density function of the magnitude of velocity is asymptotic to $u^{-8/3}$ for small velocities, and to u^{-5} for large velocities. The former power law is due to the long-time diffusion of vorticity as the vortex ring expands, while the latter is due to the initial diffusion of vorticity away from the vortex filament immediately after its formation. While the large u distribution will depend heavily on the exact model used (e.g., Min et al. (1996) found exponential tails in their study of two-dimensional patches of vorticity because each isolated patch had a maximum velocity), the $u^{-8/3}$ power law for small velocities is robust in the sense that any flow brought about by an initial impulse will produce a distribution with the same power law.

We have constructed a model suspension of viscous vortex rings with convenient analytic properties by superimposing the flow fields for individual vortex rings positioned and oriented randomly throughout space and time. The velocity fluctuations were shown both analytically and nu-

merically to fit a truncated stable distribution with tails decaying as $u^{-8/3}$. This distribution has core width proportional to $\phi^{3/5}$ but energy proportional to ϕ, the vortex volume fraction, so that most of the energy comes from the tail of the distribution (associated with large velocities). Points in space corresponding to the distribution's tail are only influenced by the nearest vortex ring, so interactions between vortices play a negligible role. However, with increasing volume fraction ϕ, the dominant contribution begins to come from the core region encompassing the far-field velocity of many not-so-distant vortices.

Our work extends efforts to understand the velocity fluctuations produced by swimmers at low Reynolds numbers to intermediate values. We expect the model to provide a good approximation for the flow fields associated with a variety of jellyfish species in a physically-realistic regime of the Reynolds number ($60 \lesssim \mathrm{Re} \lesssim 2160$) (Olesen et al., 1994), particularly in light of the robustness of the flow structure to perturbations of the initial impulse. Even among jellyfish, however, different types of flow fields are generated by different species: elongated jellyfish such as *Nemopsis bachei* generate a streak of vortex rings for efficient swimming (Colin and Costello, 2002; Dabiri et al., 2006) while more bulbous species like *Aurelia aurita* generate dual starting and stopping vortex rings (during power and recovery strokes) in the wake of the bell in a slower, axisymmetric-paddling locomotion (Colin and Costello, 2002; Dabiri et al., 2005; Hoover et al., 2017). The extent to which the distribution derived here remains

appropriate for describing such systems, and related nonmotile systems like pulsing corals (Samson et al., 2017), remains an open question for future exploration.

Finally, it is an open question whether the velocity distributions predicted here can be measured experimentally in some context. A realistic environment is probably too noisy to hope for the simple model presented here to have quantitative value, but possibly the tails of the distribution are robust enough to be measurable. Laboratory experiments are not out of the question, though a mechanism would need to be devised for adequate generation of the random vortices, in a tank large enough for edge effects to be negligible.

4 THE DISPLACEMENTS OF TRACER PARTICLES FOR A DILUTE SUSPENSION OF VISCOUS VORTEX RINGS

The particle displacements, or drifts, which arise from the velocity fluctuations studied in the previous chapter are often more important in the context of fluid mixing. In this chapter, we examine the drift over time due to a single vortex ring and then apply that model to an isotropic dilute suspension of viscous vortex rings. Although we were unable to derive analytic expressions for the distribution of drifts in the suspension, which unlike the distribution of velocities will now be time-dependent, we can still make many predictions about various aspects of the probability density function.

In Section 4.1, we examine the velocity autocorrelation function, which will provide clues for how the distribution of drifts should evolve over longer time scales. An expression for the velocity autocorrelation function which is dependent on the size of the domain will be derived, which will shed light on the time scale in which boundary effects become significant. Then in Section 4.2, we integrate the velocity field due to the streamfunction (2.27) numerically, taking into account the motion of the vortex ring as a whole (2.34). We can also derive an asymptotic formula for the drift which is correct to leading order for particles initially positioned far away from the vortex ring. In Section 4.3, we use this asymptotic formula in order to determine the absolute moments of the distribution for a sus-

pension of vortices, which are finite for $\frac{5}{3} < n < 5$ (or for $n > \frac{5}{3}$ without an upper bound when considering corrections in the near field). In particular, the second moment grows in time as $t^{3/2}$, which corresponds to superdiffusion.

Since the second moment is finite and growing in time, we will be able to apply the central limit theorem in order to conclude that the distribution of drifts becomes a truncated Gaussian as $t \to \infty$. Since the drift due to a single vortex ring is bounded by a finite constant, we also know that the tails of the distribution, outside the Gaussian core, will decay exponentially. For smaller times, the distribution is a truncated $\frac{5}{3}$-stable distribution. Interestingly, the scale parameter for this distribution grows linearly in time. This distribution shape and time scaling can be explained in terms of the drifts in the fair field, and they are verified with numerical simulations.

In Sections 4.1-4.3, we assumed the velocity fluctuations were due to force monopoles – the robustness observed for the velocity fluctuations in Section 3.3 carry through to the drifts. The chapter is concluded with a discussion of how the results for the drift distribution are modified for a flow caused by randomly-generated forcing with zero monopole contribution in Section 4.4, followed by a general discussion of all the results of this chapter in Section 4.5.

4.1 Velocity autocorrelations

It will be useful in our discussion of drifts in the subsequent sections to determine properties of the velocity autocorrelation function

$$c_{\nu,ij}(t, t+\tau) := \langle (\mathbf{v}(t) \cdot \hat{\mathbf{e}}_i)(\mathbf{v}(t+\tau) \cdot \hat{\mathbf{e}}_j) \rangle. \tag{4.1}$$

Although τ can be any real number, we will require $\tau \geqslant 0$ for the remainder of this section. The autocorrelation is symmetric in τ, so $c_{\nu,ij}(t, t+\tau) = c_{\nu,ij}(t+\tau, t)$. Assuming as before that the suspension is in equilibrium, c_ν is independent of t, which we now fix to be zero, and by isotropy,

$$c_{\nu,ij}(0, \tau) = \tfrac{1}{3}\delta_{ij}\langle \mathbf{v}(0) \cdot \mathbf{v}(\tau) \rangle. \tag{4.2}$$

Then let $c_\nu(\tau) := \frac{1}{3}\langle \mathbf{v}(0) \cdot \mathbf{v}(\tau) \rangle$, which is the main quantity we will be interested in computing. For very short times τ, $\langle \mathbf{v}(0) \cdot \mathbf{v}(\tau) \rangle \approx 2\mu\mathcal{E}_1$ is approximately twice the energy of the suspension, so $c_\nu(\tau) \sim \frac{2}{3}\mu\mathcal{E}_1$ as $\tau \downarrow 0$. Then the mean square drift (that is, the expectation of the magnitude of the particle displacement squared) is

$$\langle |\boldsymbol{\Delta}|^2 \rangle \sim 2\mu\mathcal{E}_1 t^2 = \frac{1}{3}\frac{\mu\Gamma_0^2 R_0^3 t^2}{\eta}, \tag{4.3}$$

corresponding to ballistic motion. The details of this calculation are expounded upon in Equations (4.9)-(4.11) later in this section.

Now we consider the behavior of $c_v(\tau)$ for larger time differences τ. Towards this end, consider the velocity autocorrelations for a single vortex ring. Approximate the velocity field due to a single vortex ring by (2.39). Recall that this approximation is reasonably close to correct for small velocities, except around the transition region at the viscous front $\xi = 1$. Then for a vortex ring born at the origin at time $t = 0$,

$$\mathbf{v}(\mathbf{r}, t) \cdot \mathbf{v}(\mathbf{r}, t+\tau) = \begin{cases} 0 & t \leqslant 0, \\ \dfrac{\Gamma_0^2 R_0^4 (4z^2 + \rho^2)}{16 r^8} & 0 < t \leqslant t + \tau < \dfrac{r^2}{4\eta}, \\ \dfrac{\Gamma_0^2 R_0^4 (2z^2 - \rho^2)}{48\sqrt{\pi} r^5 \eta^{3/2} (t+\tau)^{3/2}} & 0 < t < \dfrac{r^2}{4\eta} \leqslant t + \tau, \\ \dfrac{\Gamma_0^2 R_0^4}{144\pi\eta^3 t^{3/2} (t+\tau)^{3/2}} & t \geqslant \dfrac{r^2}{4\eta}. \end{cases} \tag{4.4}$$

Now assume that our domain is a large sphere of radius L centered at the origin $B_L(\mathbf{0})$ and that $t \in [0, T]$. Then the expectation of (4.4), averaged over $\mathbf{r}$ and t, is

$$\langle \mathbf{v}(\mathbf{r}, t) \cdot \mathbf{v}(\mathbf{r}, t+\tau) \rangle = \int_0^T \int_{B_L(\mathbf{0})} \mathbf{v}(\mathbf{r}, t) \cdot \mathbf{v}(\mathbf{r}, t+\tau) \, \frac{dV_{\mathbf{r}}}{\frac{4}{3}\pi L^3} \frac{dt}{T}. \tag{4.5}$$

In the limit as $L, T \to \infty$, the integral is asymptotic to

$$\langle \mathbf{v}(t) \cdot \mathbf{v}(t+\tau) \rangle \sim \frac{32 + 9\pi}{288\pi L^3 T} \frac{\Gamma_0^2 R_0^4}{\eta^{3/2} \tau^{1/2}}. \tag{4.6}$$

This is the contribution to the autocorrelation function due to a solitary vortex ring.

If there are $N = \mu \cdot \frac{4}{3}\pi L^3 T$ vortices randomly isotropically distributed in our domain, then

$$\langle \mathbf{v}(0) \cdot \mathbf{v}(\tau) \rangle = \left\langle \sum_{i=1}^{N} \mathbf{v}^i(t_i) \cdot \sum_{j=1}^{N} \mathbf{v}^j(t_j + \tau) \right\rangle = \sum_{i=1}^{N} \langle \mathbf{v}^i(t_i) \cdot \mathbf{v}^i(t_i + \tau) \rangle, \quad (4.7)$$

where $\mathbf{v}^i(t_i)$ is the velocity at the origin due to the ith vortex, which was born at a time $-t_i$. Note that the cross terms go to zero due to isotropy, so this is just N times the contribution to the autocorrelation function due to a single vortex ring, i.e., (4.6). Therefore, the velocity autocorrelation function for the suspension of vortices is

$$c_v(\tau) = \frac{32 + 9\pi}{648} \frac{\mu \Gamma_0^2 R_0^4}{\eta^{3/2} \tau^{1/2}}. \quad (4.8)$$

This decays very slowly with τ. Recall the discussion of particle displacements due to microswimmers from Section 1.4. Zaid et al. (2011) estimated that velocity autocorrelations vanished after a relatively short period of time, after which (1.30) was valid. Since $c_v(\tau)$ does not decay quickly enough with τ in order to be able to integrate in time as $\tau \to \infty$, there is no length of time after which it is okay to assume that the velocity autocorrelations vanish. Therefore, there is no reason to think that the distribution of drifts should become a Gaussian with width scaling like

$t^{1/2}$, and we cannot easily modify the analysis of Zaid et al. (2011) to obtain the distribution of the particle displacements.

From the velocity autocorrelations, it is possible to obtain an estimate for the mean squared displacement. Let $\mathbf{r}(0) = \mathbf{0}$ (so the particle starts at the origin). Then

$$\langle (\mathbf{r}(t) \cdot \hat{\mathbf{e}}_i) \cdot (\mathbf{r}(t) \cdot \hat{\mathbf{e}}_j) \rangle = 2t \int_0^t c_{v,ij}(\tau)\, d\tau - 2 \int_0^t \tau c_{v,ij}(\tau)\, d\tau \tag{4.9}$$

(Graham, 2018). Noting that $c_{v,ij}$ is given by (4.8) for $i = j$ and is zero otherwise,

$$\langle (\mathbf{r}(t) \cdot \hat{\mathbf{e}}_i) \cdot (\mathbf{r}(t) \cdot \hat{\mathbf{e}}_j) \rangle = \frac{32 + 9\pi}{243} \frac{\mu \Gamma_0^2 R_0^4 t^{3/2}}{\eta^{3/2}} \delta_{ij}. \tag{4.10}$$

In particular, the mean square drift is

$$\langle |\boldsymbol{\Delta}|^2 \rangle = \frac{32 + 9\pi}{81} \frac{\mu \Gamma_0^2 R_0^4 t^{3/2}}{\eta^{3/2}}. \tag{4.11}$$

As with other results which make use of (2.39), the coefficient in front is likely incorrect: there should be corrections from the near-field velocity as well as from the diffusive front, but the scaling is correct and will be confirmed in Section 4.3 with explicit computation of the drifts. At present, it is clear that the mean square drift grows superlinearly in time, so the advection of particles in the suspension is superdiffusive (anomalous diffusion).

The preceding discussion assumed that the suspension was in an infinite domain, with L and T taken to go to infinity. However, if L and T are finite, then

$$c_v(\tau) = \frac{32+9\pi}{648}\frac{\mu\Gamma_0^2 R_0^4}{\eta^{3/2}\tau^{1/2}}\left(1-\sqrt{1-\frac{T}{T+\tau}}\right) - \frac{\pi}{18}\frac{T}{L^3}\frac{\mu\Gamma_0^2 R_0^4}{\tau}. \qquad (4.12)$$

The above assumes that $4\eta(T+\tau) < L^2$, which is the region we will focus on. More complicated expressions can be written for the other conditions on the domain boundaries, but they will be unnecessary for our purposes.

The quantity in parenthesis in (4.12) is asymptotic to $T/2\tau$ for $\tau \gg T$, so we see that at time of order T, the final term on the right-hand side of (4.12) becomes dominant, and the velocity autocorrelation decays as $O(\tau^{-1})$ (at least until $\tau \approx L^2/4\eta$).

This argument could be continued in order to compute the scaling for the drifts based on the finite domain size, but for our purposes, it is sufficient to know that the $t^{3/2}$ scaling for the mean square drift will only persist up to times $t \lesssim \min\{T, L^2/4\eta\}$, after which the boundary will start to have an effect. It is also possible for the particle to leave the domain earlier (if μ is large enough), in which case (4.11) is also no longer valid.

4.2 Drift due to a single viscous vortex ring

Let $\mathbf{x}(t)$ be the position of a particle as a function of time. We define the drift of the particle $\boldsymbol{\Delta}(\mathbf{x}(0), t) := \mathbf{x}(t) - \mathbf{x}(0)$ to be the displacement vector of its position. In a flow $\mathbf{U}(\mathbf{x}, t)$, the displacement satisfies

$$\boldsymbol{\Delta}(\mathbf{x}(0), t) = \int_0^t \mathbf{U}(\mathbf{x}(s), s)\, ds. \tag{4.13}$$

In Section 2.5, we noted that the vortex ring grows in size over time as a result of diffusion, so that particles become entrained and eventually move along with the vortex ring as it decays. Therefore, for particles that are trapped by the vortex ring very early on in its evolution, $\boldsymbol{\Delta}(\mathbf{x}, t) \gtrapprox S(t)\mathbb{Q}\hat{\mathbf{z}}$, where recall that $\mathbb{Q}\hat{\mathbf{z}}$ specified the orientation of a vortex ring in Section 3.1. For the remainder of this section, we will assume that all vortices are oriented in the $+\hat{\mathbf{z}}$-direction and are initially created at the origin.

In Figure 4.1, components of the infinite-time drifts $\boldsymbol{\Delta}(\mathbf{x}, \infty)$ are plotted as a function of position for a model vortex ring (see Section 2.3) with Reynolds number $Re = 300$ and with units chosen so that $R_0 = \eta = 1$. Note in particular that the component of drift in the direction of motion of the vortex ring is strictly positive for all points in space, and that it appears to be larger in magnitude than the portion of drift in the perpendicular direction. We see that the particles which are entrained into the vortex ring very early on have a z-displacement of up to 29, while by (2.38), $S(\infty) \approx 20$. Therefore, particles which are entrained into the vortex ring early on end

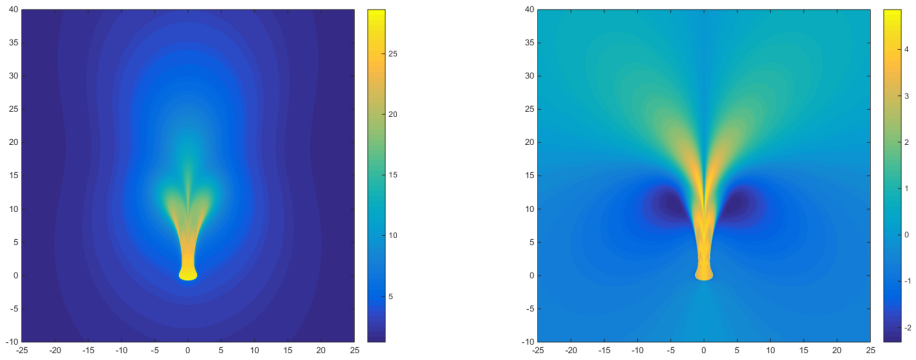

Figure 4.1: Particle displacements in the $\hat{\mathbf{z}}$ (left) and $\hat{\boldsymbol{\rho}}$ (right) directions as a function of initial position due to a vortex ring with Reynolds number $\mathrm{Re} = 300$ initially located at the origin and oriented in the $+\hat{\mathbf{z}}$-direction. Units are chosen such that $R_0 = \eta = 1$.

up closer to the front of the vortex ring as $t \to \infty$, consistent with the observations made in Section 2.5.

Figure 4.2 shows the magnitudes of the displacements as a function of initial position for particles initially located near the origin. Note the sharp transition region near the origin from drifts around $\Delta = 29$ to $\Delta = 5$. Particles near the vortex ring but outside it initially are only dragged a short distance along with the vortex ring, which quickly moves out of the immediate area along with the particles trapped inside it. This transition boundary remains relatively sharp, but moves further away from the centerline $\rho = 0$ as z increases. Thus, we see that the particles which are entrained into the vortex ring and pulled along the furthest are those which are initially in front of the vortex ring, move out of the way around the side of the vortex ring, and then are eventually pulled up through the

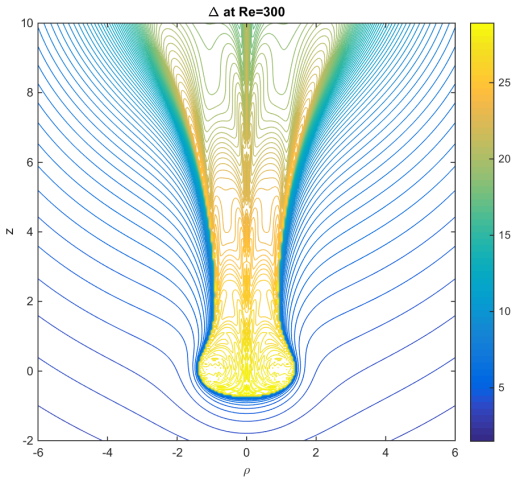

Figure 4.2: The magnitude of the particle displacements on a zoomed-in region near the origin.

center of the vortex ring.

Far-field drifts

The model presented in Section 2.3, while possessing many nice analytical properties, is still too complicated to integrate exactly in order to solve for the drifts, so it is of note that for particles which are initially located a distance $r \gg R_0$ away from the vortex ring, the approximations of the streamfunction (2.18) and velocity field $\mathbf{u}$ (2.17) are valid for all time. Since the vortex ring only moves a distance $O(R_0)$, the correction to the velocity field due to the movement of the vortex ring only enters into the calculation of the velocity as a second-order correction. Also, it is helpful to neglect the motion of the particles themselves, which are dwarfed by the motion

of the vortex ring as they are of order $O(R_0/r)$ or smaller. Therefore, we may approximate the drift as

$$\boldsymbol{\Delta}(\mathbf{x}(0), t) = \int_0^t \mathbf{u}(\mathbf{x}(s), s)\, ds \approx \int_0^t \mathbf{u}(\mathbf{x}(0), s)\, ds. \tag{4.14}$$

It may further be prudent to compute $\mathbf{u}$ using the expression (2.17), but with respect to a different point as the origin. Since the vortex ring completes most of its motion in a time $t = O(R_0^2/\eta)$, the vortex ring spends most of the time near its final position. Therefore, the approximation

$$\boldsymbol{\Delta}(\mathbf{x}(0), t) \approx \int_0^t \mathbf{u}(\mathbf{x}(0) - S(t)\hat{\mathbf{z}}, s)\, ds \tag{4.15}$$

is likely closer to the true drift than (4.14). Note that these equations each predict the same drift fields modulo a shift of $S(t)$ in the $\hat{\mathbf{z}}$-direction.

Explicitly, (4.14) predicts a drift of

$$\boldsymbol{\Delta}(\mathbf{x}, t) \sim \frac{I}{8\pi\eta r^3}\left([C_1(2z^2+\rho^2) + C_2(2z^2-\rho^2)]\hat{\mathbf{z}} + [(C_1+3C_2)z\rho]\hat{\boldsymbol{\rho}}\right), \tag{4.16}$$

valid as $r \to \infty$, where

$$C_1 = \operatorname{erfc}(\xi), \tag{4.17}$$

$$C_2 = \frac{\operatorname{erf}(\xi)}{2\xi^2} - \frac{1}{\pi^{1/2}\xi}e^{-\xi^2}. \tag{4.18}$$

Recall that $\xi = r/\sqrt{4\eta t}$ (we can take $t_0 = 0$ in the original definition),

where for our purposes it is most convenient to measure ξ, with respect to the final time t.

In the limit as $t \to \infty$, $C_1 \to 1$ and $C_2 \to 0$, so that (4.16) approaches the limit

$$\boldsymbol{\Delta}(\mathbf{x}, \infty) \sim \frac{I}{8\pi\eta r^3} \left((2z^2 + \rho^2)\hat{\mathbf{z}} + z\rho\hat{\boldsymbol{\rho}} \right). \tag{4.19}$$

As $2z^2 + \rho^2 > z\rho$ for all points in the far field, we confirm observations made from Figure 4.1 that the drift is primarily in the $\hat{\mathbf{z}}$-direction and 4.1 that this component of drift is always positive.

For finite times t, however, this is not necessarily the case. For points with $r \gg \sqrt{4\eta t}$, $\xi \gg 1$, so C_1 is exponentially small, while $C_2 \sim 1/2\xi^2$. In this regime,

$$\boldsymbol{\Delta}(\mathbf{x}, t) \sim \frac{It}{4\pi r^5} \left((2z^2 - \rho^2)\hat{\mathbf{z}} + 3z\rho\hat{\boldsymbol{\rho}} \right), \tag{4.20}$$

so particles which initially start out with $\rho^2 < 2z^2$ move backwards, opposite the direction of the vortex ring, over a time interval of size $O(r^2/\eta)$. However, the net integrated drift over all particles is still in the positive $\hat{\mathbf{z}}$-direction. An integral of (4.16) over all space reveals that

$$\int_{\mathbb{R}^3} \boldsymbol{\Delta}(\mathbf{x}, t)\, d\mathbf{x} = \frac{2}{3} It\hat{\mathbf{z}}. \tag{4.21}$$

The near field offers an $O(1)$ correction, so the above expression is correct to leading order (in time). This suggests that $2/3$ of the net momentum imparted by the impulse goes into the vortex ring, as in Bühler (2007), who

found that the other $1/3$ goes into a wave propagating out from the source, which we have neglected here since we are assuming incompressibility.

It is also worth looking at the drift before and after the diffusive front hits at time $t = r^2/4\eta =: t_{\xi=1}$. At the diffusive front,

$$\boldsymbol{\Delta}(\mathbf{x}, t_{\xi=1}) \cdot \hat{\mathbf{z}} = \left(0.029531z^2 - 0.0022480\rho^2\right) \frac{I}{\eta r^3}, \tag{4.22}$$

$$\boldsymbol{\Delta}(\mathbf{x}, t_{\xi=1}) \cdot \hat{\boldsymbol{\rho}} = 0.031779 \frac{Iz\rho}{\eta r^3}. \tag{4.23}$$

Note in particular that the drift in the $\hat{\boldsymbol{\rho}}$-direction is larger than the drift in the $\hat{\mathbf{z}}$-direction for many values of z and ρ.

After the diffusive front hits, the remaining drift is

$$(\boldsymbol{\Delta}(\mathbf{x}, \infty) - \boldsymbol{\Delta}(\mathbf{x}, t_{\xi=1})) \cdot \hat{\mathbf{z}} = \left(0.050047z^2 + 0.042037\rho^2\right) \frac{I}{\eta r^3}, \tag{4.24}$$

$$(\boldsymbol{\Delta}(\mathbf{x}, \infty) - \boldsymbol{\Delta}(\mathbf{x}, t_{\xi=1})) \cdot \hat{\boldsymbol{\rho}} = 0.0080099 \frac{Iz\rho}{\eta r^3}. \tag{4.25}$$

We see that the drift in the ρ direction is about 80% completed by the time the diffusive front hits, while there is still a reasonably large positive drift in the z direction after the diffusive front hits which is at least as large as the pre-diffusive drift and often much larger.

Now we redo the calculation for the drifts by taking the motion of the vortex ring into consideration (in order to determine the magnitude of the

error introduced by our approximations). In this case,

$$\Psi(\rho, z, t) \approx \frac{I}{2\pi^{3/2}} \left(\int_0^{\xi} e^{-\xi'^2} d\xi' - \xi e^{-\xi^2} \right) \frac{\rho^2}{((z - S(t))^2 + \rho^2)^{3/2}}, \quad (4.26)$$

where now ξ takes into consideration the total displacement $S(t)$ of the vortex ring:

$$\xi := \sqrt{\frac{(z - S(t))^2 + \rho^2}{4\eta t}}. \quad (4.27)$$

Since $S(t)$ is bounded, we can perform a multipole expansion on Ψ, valid for large r, which results in

$$\Psi \sim \Psi_0 + \Psi_1 \frac{zS(t)}{2r^2} + \cdots, \quad (4.28)$$

$$\Psi_0 = \frac{I}{2\pi^{3/2}} \frac{\rho^2}{r^3} \left(\int_0^{\xi_0} e^{-\xi'^2} d\xi' - \xi_0 e^{-\xi_0^2} \right), \quad (4.29)$$

$$\Psi_1 = \frac{I}{2\pi^{3/2}} \left(3 \int_0^{\xi_0} e^{-\xi'^2} d\xi' - \xi_0 e^{-\xi_0^2} \left(2\xi_0^2 + 3 \right) \right), \quad (4.30)$$

where $\xi_0 := \sqrt{r^2/4\eta t}$ neglects the vortex displacement S. As expected, the leading order term Ψ_0 is simply (2.18). For a constant value of S, the correction to $\boldsymbol{\Delta}(\infty)$ is

$$\boldsymbol{\Delta}_{\text{corr}}(\mathbf{x}, \infty) = \frac{(2z^2 - \rho^2) IS}{16\pi\eta r^5} \mathbf{x}. \quad (4.31)$$

While it is too difficult to perform these calculations for the true vortex movement $S(t)$, we see that the difference between $\boldsymbol{\Delta}$ with and $\boldsymbol{\Delta}$ without nonzero vortex displacement S is proportional to $S\mathbf{x}/r^3$. Thus, the error in

the drift due to ignoring the motion of the vortex ring scales as S/r^2.

In order to determine whether it is better to take the vortex start position or end position as the origin, consider Ψ_1 and compute the first-order correction to $v_z = \mathbf{v} \cdot \hat{\mathbf{z}}$:

$$v_{z,\text{corr}} = \frac{IzS}{8\pi^{3/2}r^7}\left(\left(6\pi^{1/2}\text{erf}(\xi_0) - 4\xi_0 e^{-\xi_0^2}(2\xi_0^2+3)\right)z^2 + \left(2\xi_0 e^{-\xi_0^2}(2\xi_0^2+3)^2 - 9\pi^{1/2}\text{erf}(\xi_0)\right)\rho^2\right). \tag{4.32}$$

Note that the coefficients of z^2 and ρ^2 are each bounded in magnitude by $9\pi^{1/2}$ for all $0 \leqslant \xi_0 < \infty$. As $t \to \infty$ these coefficients go to zero, giving us a better bound dependent on t. Therefore

$$|v_{z,\text{corr}}| \lesssim \min\left(\frac{9I|z|S}{8\pi r^5}, \frac{3Ir|z|S}{128\pi^{3/2}(\eta t)^3}\right). \tag{4.33}$$

Similarly, the correction to $v_\rho = \mathbf{v} \cdot \hat{\boldsymbol{\rho}}$ is

$$v_{\rho,\text{corr}} = \frac{I\rho S}{8\pi^{3/2}r^7}\left(\left(12\pi^{1/2}\text{erf}(\xi_0) - 8\xi_0 e^{-\xi_0^2}(2\xi_0^4+2\xi_0^2+3)\right)z^2 + \left(2\xi_0 e^{-\xi_0^2}(2\xi_0^2+3) - 3\pi^{1/2}\text{erf}(\xi_0)\right)\rho^2\right). \tag{4.34}$$

Now we note that each of the two expressions involving ξ_0 is bounded in magnitude by $12\pi^{1/2}$ (and that we have a better bound as $t \to \infty$), so

$$|v_{\rho,\text{corr}}| \lesssim \min\left(\frac{3I\rho S}{2\pi r^5}, \frac{6I\rho S}{160\pi^{3/2}(\eta t)^{5/2}}\right). \tag{4.35}$$

In order to determine the error in computing the drifts when fixing the final position of the vortex ring as the origin, we let $\sigma(t) = S(\infty) - S(t)$ be the distance the vortex ring has yet to move. Note that the asymptotic expansions in the previous few lines are now valid when replacing S by σ. The quantity σ is bounded by $S(\infty)$, and as with the velocity, we have a better bound for large times:

$$0 \leqslant \sigma \lesssim \min\left(\frac{5I}{24\pi^2\eta R_0}, \frac{7I}{120\sqrt{2\pi^3\eta^3 t}}\right). \tag{4.36}$$

Using these bounds on σ and $|\nu|$ gives us a finite bound on the error integral. To leading order,

$$\begin{aligned} |\boldsymbol{\Delta}_{\text{corr}}(\infty)\cdot\hat{\mathbf{z}}| = &\int_0^{49\pi R_0^2/1250\eta} \frac{9I|z|}{8\pi r^5}\frac{5I}{24\pi^2\eta R_0}\,dt \\ &+ \int_{49\pi R_0^2/1250\eta}^{r^2/(2\times 6^{1/3}\pi^{1/6}\eta)} \frac{9I|z|}{8\pi r^5}\frac{7I}{120\sqrt{2\pi^3\eta^3 t}}\,dt \\ &+ \int_{r^2/(2\times 6^{1/3}\pi^{1/6}\eta)}^{\infty} \frac{3Ir|z|}{128\pi^{3/2}(\eta t)^3}\frac{7I}{120\sqrt{2\pi^3\eta^3 t}}\,dt. \end{aligned} \tag{4.37}$$

A similar calculation holds for $|\boldsymbol{\Delta}_{\text{corr}}(\infty)\cdot\hat{\boldsymbol{\rho}}|$. The integrals evaluate to

$$|\boldsymbol{\Delta}_{\text{corr}}(\infty)\cdot\hat{\mathbf{z}}| \lesssim \frac{21\times 6^{5/6}}{1600\pi^{31/12}}\frac{|z|I^2}{\eta^2 r^4} \approx 0.0030357\frac{|z|I^2}{\eta^2 r^4}, \tag{4.38}$$

$$|\boldsymbol{\Delta}_{\text{corr}}(\infty)\cdot\hat{\boldsymbol{\rho}}| \lesssim \frac{7\times 2^{9/10}\times 5^{4/5}}{640\pi^{13/5}}\frac{\rho I^2}{\eta^2 r^4} \approx 0.0037708\frac{\rho I^2}{\eta^2 r^4}. \tag{4.39}$$

Therefore, we see that the error in the drift when using the final vortex position as the origin is $O(1/r^3)$, while the error in using the initial vortex

position as the origin must be $O(1/r^2)$ (since that is the difference between the two calculations). Therefore, using the final vortex position as the origin is definitively better than using the initial position.

We confirmed this analytical observation numerically by computing drifts for the model vortex ring analytically, integrating using Matlab's built-in ODE45 solver, and comparing the results to the drifts predicted by (4.16) with the origin at either the starting location of the vortex ring or the final position. For the purposes of these simulations, $R_0 = \eta = 1$ was fixed, as was the Reynolds number $Re = 100$. The results for $\Delta z = \boldsymbol{\Delta} \cdot \hat{\mathbf{z}}$ and $\Delta\rho = \boldsymbol{\Delta} \cdot \hat{\boldsymbol{\rho}}$ for several different choices of initial z and ρ are plotted as functions of time in Figures 4.3a-4.7a. The corresponding particle trajectories are plotted in the ρz-plane in Figures 4.3b-4.7b, respectively. It is clear for a wide range of initial conditions that the analytic expression (4.16) in the shifted domain (with the origin set to be the final position of the vortex ring) is generally much closer to the actual drift than the same expression in the unshifted domain.

Of special note are the trajectories for points with initial z in the range $0 \leqslant z \leqslant S(\infty)$, as in Figure 4.5. For a particle initially located at the point $z = 3 \approx 0.45S(\infty)$ and $\rho = 20$, note that the analytic approximation for Δz in both the shifted and unshifted domains is very close to the actual drift in that direction. However, the signs of $\Delta\rho$ in the two calculations are different. The expression for the shifted domain has the correct sign, which is unsurprising given that the vortex ring passes $z = 3$ in time

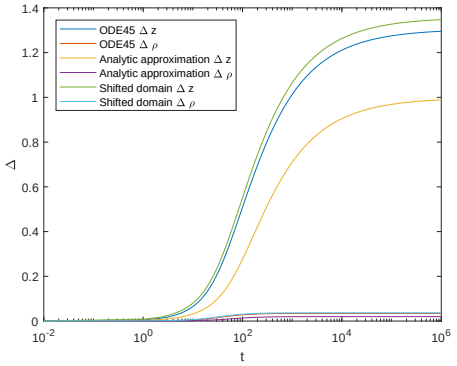

(a) Change in position as a function of time.

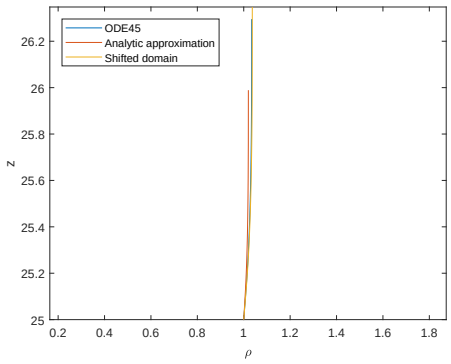

(b) Particle paths.

Figure 4.3: Drift and particle paths for tracer initially at $z = 25$ and $\rho = 1$.

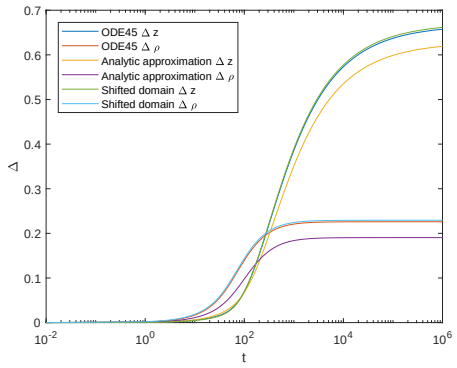

(a) Change in position as a function of time.

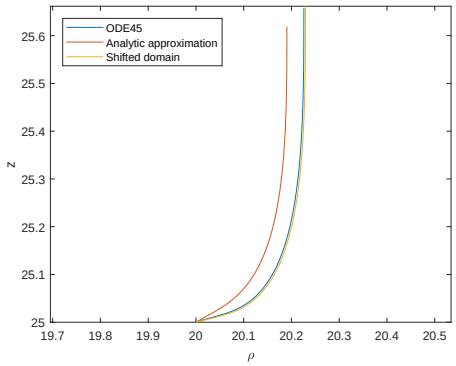

(b) Particle paths.

Figure 4.4: Drift and particle paths for tracer initially at $z = 25$ and $\rho = 20$.

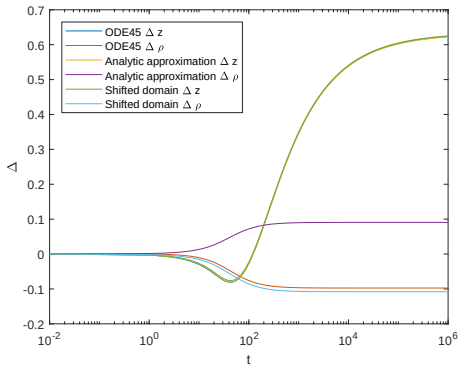

(a) Change in position as a function of time.

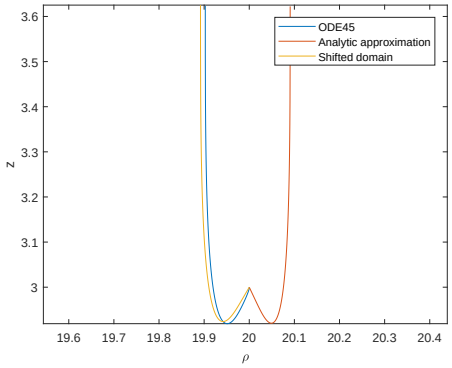

(b) Particle paths.

Figure 4.5: Drift and particle paths for tracer initially at $z = 3$ and $\rho = 20$.

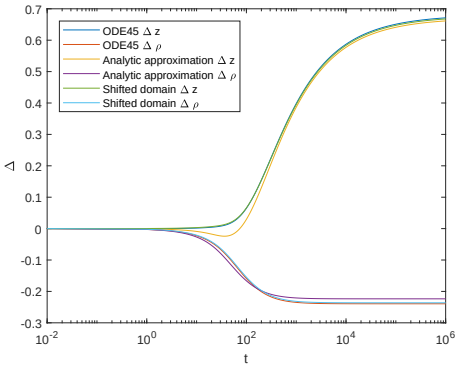

(a) Change in position as a function of time.

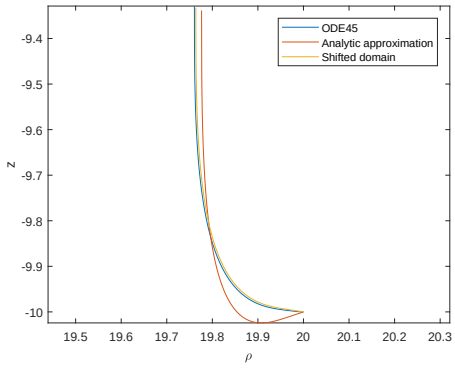

(b) Particle paths.

Figure 4.6: Drift and particle paths for tracer initially at $z = -10$ and $\rho = 20$.

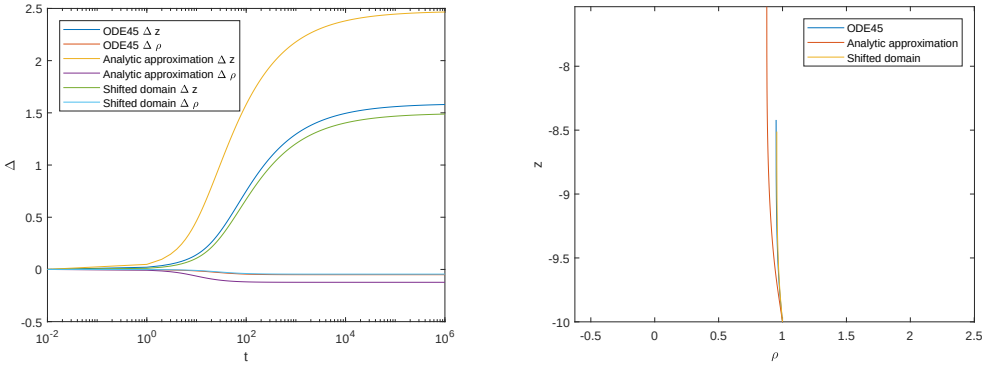

(a) Change in position as a function of time.

(b) Particle paths.

Figure 4.7: Drift and particle paths for tracer initially at $z = -10$ and $\rho = 1$.

$O(R_0^2/\eta)$, while there is significant particle motion in the $\hat{\boldsymbol{\rho}}$-direction for time $O(r^2/\eta)$. Since v_ρ changes sign depending on whether z is positive or negative, it is clearly better to use the shifted domain, which gives the wrong direction of the drift in the $\hat{\boldsymbol{\rho}}$-direction for a much shorter period of time than in the unshifted domain.

Also striking is the difference in the predictions in Δz, particularly for points closer to the axis of motion $\rho = 0$. In Figures 4.3 and 4.7, we plot the drifts for particles initially located so that $\rho = 1$ and so that $z = 25$ (in front of the vortex ring) or $z = -10$ (behind the vortex ring), respectively. Although the analytic approximations for Δz are not as good in these figures as in the others (which have $\rho = 20$), the approximation in the shifted domain is easily seen to be closer to correct. Indeed, in each of Figures 4.3b-4.7b, the trajectories predicted by the analytic formula in the shifted domain look much closer to the true particle paths.

4.3 Drift due to a suspension of viscous vortex rings

We now turn to a suspension of viscous vortex rings, as in Chapter 3. Just like with velocity fluctuations, it is natural to want to understand the fluctuations of particle positions (i.e., drifts) caused by a random isotropic suspension of vortices. As with the velocity fluctuations in Section 3.2, we can modify an argument by Thiffeault (2015) in the study of particle displacements due to microswimmers. The argument is more complicated for vortex rings than for microswimmers because the Stokes equations (1.7) are time-independent, so for the microswimmers, only one time integral is required: displacement is the integral of velocity. For the case of mixing by vortices, however, the time at which the vortices were born also matters due to the fact that they decay over time. Therefore, a second time integral is required over possible birth times.

Single vortex ring

We first need additional notation to handle the drift due to a single vortex ring born before the start of the tracking of the particle displacement. Let

$$\boldsymbol{\Delta}_1(\mathbf{x}, t; \mathbf{x}_0, t_0, \mathbb{Q}) := \mathbb{Q}[\boldsymbol{\Delta}(\mathbf{x} - \mathbf{x}_0, t - t_0) - \boldsymbol{\Delta}(\mathbf{x} - \mathbf{x}_0, -t_0)] \tag{4.40}$$

be the drift between times zero and t due to a single vortex ring born at time t_0. Here, we require $\boldsymbol{\Delta}(\mathbf{x}, t) \equiv \mathbf{0}$ for $t \leqslant 0$ in order to be able to handle the case that the vortex ring is born after the time where we start tracking the drifts (in which case it only starts to affect the motion of the particle after it was born). The vortex ring is formed at position $\mathbf{x}_0$, and as before, $\mathbb{Q}$ is the orientation of the vortex ring.

Recall that we replaced the model velocity with a simpler form (2.17) valid in the far field and again with the even simpler form (2.39) using the large and small ξ limits. As with the velocity, it will also make sense to simplify the drift formula by integrating (2.39) in order to obtain a simpler expression which captures the correct scaling, which is what will determine the behavior of the drift distribution. Towards this end, recall that the velocity before the diffusive front hits is given by

$$\mathbf{v}(\mathbf{x}, t) \approx \frac{\Gamma_0 R_0^2[(2z^2 - \rho^2)\hat{\mathbf{z}} + 3z\rho\hat{\boldsymbol{\rho}}]}{4r^5}, \tag{4.41}$$

so

$$\boldsymbol{\Delta}(\mathbf{x}, t) \approx \frac{\Gamma_0 R_0^2[(2z^2 - \rho^2)\hat{\mathbf{z}} + 3z\rho\hat{\boldsymbol{\rho}}]}{4r^5} t, \qquad t \lesssim \frac{r^2}{4\eta}. \tag{4.42}$$

Using this approximation, when the diffusive front hits, the particle a displacement

$$\boldsymbol{\Delta}(\mathbf{x}, r^2/4\eta) \approx \frac{\Gamma_0 R_0^2[(2z^2 - \rho^2)\hat{\mathbf{z}} + 3z\rho\hat{\boldsymbol{\rho}}]}{16\eta r^3}. \tag{4.43}$$

This has the same scaling and magnitude as (4.22)-(4.23), although (4.43) overestimates the size of the drift somewhat.

After the diffusive front hits, recall that (2.39) indicates that the velocity is

$$\mathbf{v}(\mathbf{x}, t) \approx \frac{\Gamma_0 R_0^2 \hat{\mathbf{z}}}{12\sqrt{\pi}(\eta t)^{3/2}}, \tag{4.44}$$

which results in additional displacement

$$\boldsymbol{\Delta}(\mathbf{x}, t) - \boldsymbol{\Delta}(\mathbf{x}, r^2/4\eta) \approx \frac{\Gamma_0 R_0^2 (1-\xi)\hat{\mathbf{z}}}{3\sqrt{\pi}\eta r}, \qquad \xi = \frac{r^2}{4\eta t} \gtrsim 1. \tag{4.45}$$

The total displacement in this case is then the sum of (4.43) and (4.45).

Using this approximation, the drift due to a single vortex ring formed at the origin (so that $\mathbf{x}_0 = \mathbf{0}$) and oriented in the $+\hat{\mathbf{z}}$-direction (so that $\mathbb{Q} = \mathbb{I}$ is the identity) is given by the cases

$$\frac{\boldsymbol{\Delta}_1(\mathbf{x}, t; \mathbf{0}, t_0, \mathbb{I})}{\Gamma_0 R_0^2} \approx \begin{cases} \dfrac{(2z^2 - \rho^2)\hat{\mathbf{z}} + 3z\rho\hat{\boldsymbol{\rho}}}{16\eta r^3 \xi_d^2}, & \xi_d \geqslant 1, \\ \dfrac{(2z^2 - \rho^2)\hat{\mathbf{z}} + 3z\rho\hat{\boldsymbol{\rho}}}{16\eta r^3} + \dfrac{1-\xi_d}{3\sqrt{\pi}\eta r}\hat{\mathbf{z}} & \xi_d < 1, \end{cases} \tag{4.46}$$

when $0 \leqslant t_0 < t$ ($\xi_d := r/\sqrt{4\eta(t-t_0)}$) and by the cases

$$\frac{\boldsymbol{\Delta}_1(\mathbf{x}, t; \mathbf{0}, t_0, \mathbb{I})}{\Gamma_0 R_0^2} \approx \begin{cases} \dfrac{(2z^2-\rho^2)\hat{\mathbf{z}} + 3z\rho\hat{\boldsymbol{\rho}}}{4r^5} t, & \xi_d \geqslant 1, \\ \dfrac{(2z^2-\rho^2)\hat{\mathbf{z}} + 3z\rho\hat{\boldsymbol{\rho}}}{4r^5}\left(\dfrac{r^2}{4\eta} + t_0\right) + \dfrac{1-\xi_d}{3\sqrt{\pi}\eta r}\hat{\mathbf{z}} & \xi_d < 1, \end{cases} \tag{4.47}$$

when $t_0 < 0$ and $r^2 > -4\eta t_0$. If $r^2 < -4\eta t_0$, then the diffusive front of the vortex ring has already hit the particle by the time we start tracking it, and so

$$\boldsymbol{\Delta}_1(\mathbf{x}, t; \mathbf{0}, t_0, \mathbb{I}) \approx \frac{\Gamma_0 R_0^2}{3\sqrt{\pi}\eta r}\left(\frac{r}{\sqrt{-4\eta t_0}} - \xi_d\right)\hat{\mathbf{z}}. \tag{4.48}$$

In the remaining case where $t_0 \geqslant t$, $\boldsymbol{\Delta}_1 \equiv \mathbf{0}$.

We will be particularly interested in the absolute moments of $\boldsymbol{\Delta}_1$ at a point $\mathbf{x} = \mathbf{0}$ integrated over $\mathbf{x}_0$ and t_0. In order to make use of the above equations, note that it is equivalent to integrate over $\mathbf{x}$ instead and fix $\mathbf{x}_0 = \mathbf{0}$, since the moments in an infinite domain should be independent of the exact position. We analyze the contributions to each of the moments from each of the five nonzero cases above, checking in particular for the values of n for which the n^{th} absolute moment is finite and for the particular value when $n = 2$.

First, consider the case where $0 \leqslant t_0 < t$ and $\xi_d \geqslant 1$. For fixed value of t_0, this corresponds to the region in space where $r \geqslant \sqrt{4\eta(t-t_0)}$. Since $|\boldsymbol{\Delta}_1|$ scales as $O(r^{-3})$, the spatial integral of $|\boldsymbol{\Delta}_1|^n$ scales as $O((t -$

$t_0)^n r_{\min}^{3-3n}) = O((t-t_0)^{(3-n)/2})$. An integration over t_0 between 0 and t reveals that this is finite for $(3-n)/2 > -1$, or $n < 5$. Note that in order for the spatial integral to be finite, it is necessary that $3-3n < 0$, so $n > 1$ as well. The contribution to the second moment is given by

$$\int_0^t \int_{|\mathbf{x}| \geqslant \sqrt{4\eta(t-t_0)}} |\boldsymbol{\Delta}_1(\mathbf{x}, t; \mathbf{0}, t_0, \mathbb{I})|^2 \, d\mathbf{x} \, dt_0 = \frac{\pi}{72} \Gamma_0^2 R_0^4 \frac{t^{3/2}}{\eta^{3/2}}. \tag{4.49}$$

Next, consider the case where $0 \leqslant t_0 < t$ and $\xi_d < 1$. In this region, $|\boldsymbol{\Delta}_1|$ scales as $O(r^{-1})$, so the spatial integral of $|\boldsymbol{\Delta}_1|^n$ scales as $O(r_{\max}^{3-n}) = O((t-t_0)^{(3-n)/2})$. From these calculations, it is clear that the moments are finite for $n < 5$. The contribution to the second moment from this region is given by

$$\int_0^t \int_{|\mathbf{x}| < \sqrt{4\eta(t-t_0)}} |\boldsymbol{\Delta}_1(\mathbf{x}, t; \mathbf{0}, t_0, \mathbb{I})|^2 \, d\mathbf{x} \, dt_0 = \frac{128 + 27\pi}{648} \Gamma_0^2 R_0^4 \frac{t^{3/2}}{\eta^{3/2}}. \tag{4.50}$$

Now consider the case where $t_0 < 0$, so the vortex ring is born before we start tracking particles, and $\xi_d \geqslant 1$. In this region, $|\boldsymbol{\Delta}_1|$ scales as $O(r^{-3})$, so the spatial integral of $|\boldsymbol{\Delta}_1|^n$ scales as $O(r_{\min}^{3-3n}) = O((t-t_0)^{3(1-n)/2})$. Then the integral over t_0 is finite for $n > \frac{5}{3}$, and the contribution to the second moment is given by

$$\int_{-\infty}^0 \int_{|\mathbf{x}| \geqslant \sqrt{4\eta(t-t_0)}} |\boldsymbol{\Delta}_1(\mathbf{x}, t; \mathbf{0}, t_0, \mathbb{I})|^2 \, d\mathbf{x} \, dt_0 = \frac{\pi}{24} \Gamma_0^2 R_0^4 \frac{t^{3/2}}{\eta^{3/2}}. \tag{4.51}$$

Next, consider the case where $t_0 < 0$ and $r^2 \leqslant -4\eta t_0$. In this regime,

the displacement is completely independent of r, so the spatial integral grows as $O(r_{max}^3)$, with time dependence dependent upon whether we are taking $t_0 \to 0^-$ or $t_0 \to -\infty$. In the former limit, $|\boldsymbol{\Delta}_1| = O(|t_0|^{-1/2})$, so the spatial integral of $|\boldsymbol{\Delta}_1|^n$ scales as $O(|t_0|^{(3-n)/2})$, which implies that it is necessary for $n < 5$. In the latter limit, however, $|\boldsymbol{\Delta}_1| = O(|t_0|^{-3/2})$ due to the cancellation between the terms. Therefore, the spatial integral of $|\boldsymbol{\Delta}_1|^n$ scales as $O(|t_0|^{3(1-n)/2})$, which implies that it is necessary for $n > \frac{5}{3}$. Now the contribution to the second moment is given by

$$\int_{-\infty}^{0} \int_{|\mathbf{x}| \leqslant \sqrt{-4\eta t_0}} |\boldsymbol{\Delta}_1(\mathbf{x}, t; \mathbf{0}, t_0, \mathbb{I})|^2 \, d\mathbf{x} \, dt_0 = \frac{24\pi - 64}{81} \Gamma_0^2 R_0^4 \frac{t^{3/2}}{\eta^{3/2}}. \tag{4.52}$$

Finally, consider the case where $t_0 < 0$, $\xi_d < 1$, and $r^2 > -4\eta t_0$. The contribution to the second moment is given by

$$\int_{-\infty}^{0} \int_{\sqrt{-4\eta t_0} < |\mathbf{x}| < \sqrt{4\eta(t-t_0)}} |\boldsymbol{\Delta}_1(\mathbf{x}, t; \mathbf{0}, t_0, \mathbb{I})|^2 \, d\mathbf{x} \, dt_0 = \frac{640 - 183\pi}{648} \Gamma_0^2 R_0^4 \frac{t^{3/2}}{\eta^{3/2}}. \tag{4.53}$$

Determining which moments converge is trickier. In the limit as $t_0 \to 0^-$, $|\boldsymbol{\Delta}_1|$ can be bounded by some constant multiple of r_{min}^{-1}, where $r_{min} = \sqrt{-4\eta t_0}$. Therefore, the integral over space of $|\boldsymbol{\Delta}_1|^n$ is bounded by a function which is $O(r_{min}^{3-n}) = O(|t_0|^{(3-n)/2})$, so the singularity at $t_0 = 0$ can only cause moments with $n \geqslant 5$ to diverge (although we have not proven that they actually will diverge). Getting a sharp bound is not necessary or worthwhile, since we already know these moments will diverge due

to previous cases. Now taking the limit as $t_0 \to -\infty$, the spatial region becomes a spherical shell of thickness $O(t^{1/2})$. In this shell, which has volume $O(t^{1/2}|t_0|)$, $|\boldsymbol{\Delta}_1| = O(t/|t_0|^{3/2})$, so the spatial integral of $|\boldsymbol{\Delta}_1|^n$ decays as $O(|t_0|^{(2-3n)/2})$, which requires $n > \frac{4}{3}$ in order for the integral over t_0 to be finite.

Adding together the five different contributions to the second moment, we find that

$$\int_{\mathbb{R}} \int_{\mathbb{R}^3} |\boldsymbol{\Delta}_1(\mathbf{x}, t; \mathbf{0}, t_0, \mathbb{I})|^2 \, d\mathbf{x} \, dt_0 = \frac{32 + 9\pi}{81} \Gamma_0^2 R_0^4 \frac{t^{3/2}}{\eta^{3/2}}, \tag{4.54}$$

which is (4.11) divided by μ. In particular, note that the second moment grows as $t^{3/2}$. As with the velocity distribution, the coefficient we have found is wrong due to the approximations we have made, but the overall scaling, which is more important, should be correct, as it is unchanged by the simplifications.

Based on the above calculations, it is precisely the $\frac{5}{3} < n < 5$ absolute moments which are finite. However, we know that the blow-up of $|\boldsymbol{\Delta}_1|$ at the origin predicted by the simplified models is unphysical: there is a maximum drift. Therefore, there is actually no upper bound on which absolute moments are finite.

We computed the drift distribution numerically via a Monte Carlo simulation with $N = 10^5$ individual realizations on a rectangular domain with edges of length $2L = 150R_0$ aligned with the Cartesian coordinate

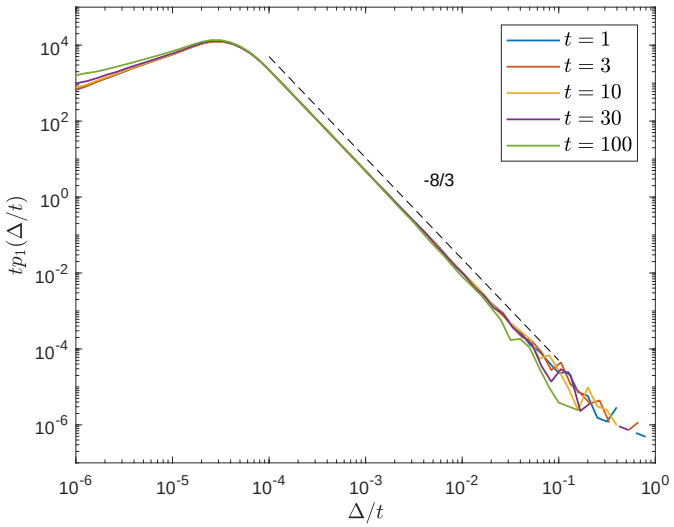

Figure 4.8: The distribution of drifts due to a single vortex ring normalized by the time.

axes and centered at the origin. Vortices were allowed to be born at any point in the time interval $[-T, t_{final}]$, where $T = 1400R_0^2/\eta$ and drifts were computed for $0 \leqslant t \leqslant t_{final}$.

The resulting distribution is plotted in Figure 4.8, normalized by the time of integration $t_{final} = t$. The distribution for the small drifts scales like $\Delta^{-8/3}$. These drifts correspond to points in the far-field initially, where the velocity changes very slowly with time (see, e.g., (4.20)). Therefore, those drifts are roughly t times the initial velocity. Since the probability density for the velocity distribution of a single vortex ring scales as $u^{-8/3}$ for small velocities, we therefore see that the probability density for the drifts scales as $\Delta^{-8/3}$ as well. Note that for the absolute smallest drifts, the boundary of the domain cuts off points which would drift that distance

(e.g., for $\Delta/t \lesssim 10^{-4}$), which explains why the $-8/3$ power law does not persist all the way to $\Delta = 0$.

Note that the $-8/3$ power law is consistent with the observation that moments are infinite for $n \leqslant \frac{5}{3}$. A different power law for large drifts, necessary so that moments are finite for $\frac{5}{3} < n < 5$, was not observed in our simulations, as more realizations would have been necessary in order to accurately resolve that portion of the distribution. However, as there is in reality a finite maximum drift d_{max}, the decision was made not to expend the computational resources necessary in order to do so.

Suspension of vortices

As in Section 3.1, we construct a dilute suspension of viscous vortex rings by allowing vortices to be born at a constant rate μ per unit volume per unit time. We again assume a dilute suspension, so $\phi := \mu R_0^5/\eta \ll 1$. Since vortices remain far apart, we can ignore interactions between them, and since the motion of the vortices or particles in the far field only affect the drift at second-order, it is reasonable to assume in this situation that the net displacement of the particle is the sum of the displacements due to the individual vortices. For N vortices, this means that

$$\boldsymbol{\Delta}(\mathbf{x}, t) = \sum_{i=1}^{N} \boldsymbol{\Delta}_1(\mathbf{x}, t; \mathbf{x}_i, t_i, \mathbb{Q}_i), \tag{4.55}$$

where the ith vortex ring is created at $\mathbf{x}_i$ at time t_i with orientation $\mathbb{Q}_i\hat{\mathbf{z}}$. Since each of the vortices is generated independently and oriented isotropically, the expected (mean) square drift is simply

$$\langle|\boldsymbol{\Delta}(\mathbf{x},t)|^2\rangle = \sum_{i=1}^{N}\langle|\boldsymbol{\Delta}_1(\mathbf{x},t;\mathbf{x}_i,t_i,\mathbb{Q}_i)|^2\rangle = N\langle|\boldsymbol{\Delta}_1|^2\rangle. \tag{4.56}$$

Now assume a spherical domain with volume V centered at $\mathbf{x}$ and that vortices are born as far back as time $-T$. Then

$$\langle|\boldsymbol{\Delta}(\mathbf{x},t)|^2\rangle = \frac{N}{V(T+t)}\int_{-T}^{t}\int_{V}|\boldsymbol{\Delta}_1(\mathbf{x},t;\mathbf{x}_0,t_0,\mathbb{I})|^2\,d\mathbf{x}_0\,dt_0. \tag{4.57}$$

Note that $N/(V(T+t)) = \mu$, and that in the limit as $-T \to -\infty$ and $V \to \mathbb{R}^3$, the integrals converge to (4.54). Therefore, we see that the mean square drift $\langle|\boldsymbol{\Delta}|^2\rangle$ is proportional to $\mu\Gamma_0^2R_0^4t^{3/2}/\eta^{3/2}$. This means that individual particle trajectories are superdiffusive.

In Section 1.4, it was noted that determining a full analytical justification for the shape of the distribution of drifts is a hard problem, particularly in the case where velocity autocorrelations die slowly enough that the second moment is superlinear in time. However, the qualitative understanding of the features of the velocity distribution explored in Section 3.2 can be applied to the drift distribution in order to obtain some partial results about its overall shape.

Since the standard deviation of the drift distribution scales like $\sigma =$

$\mu^{1/2}t^{3/4}$, for large enough t (regardless of μ), the width of the distribution (for a large enough domain) must grow to eventually be larger than the maximum drift due to a single vortex ring. By the time this occurs (if not sooner), the Berry-Esséen theorem dictates that the distribution must become Gaussian (Shlesinger, 1995), at least with the exception of the tails corresponding to larger drifts. Note that there is no guarantee that the width of the core of the distribution must scale like σ, at least for small times, since the tails could make a significant contribution to the variance of the distribution, as occurred in Section 3.2 with the velocity distribution of the suspension of vortex rings.

We now focus our attention on the tails of the distribution in an effort to surmise their shape and determine the frequency of large drifts. Especially at later times when the width of the distribution is larger than the maximum displacement due to a single vortex, the only way to achieve large drifts is for many vortices with similar orientations to be born near the particle as it moves. The probability of such an occurrence scales as e^{-N}, where N is the number of vortices born close to the particle. Since the number of vortices required to achieve a drift of d scales linearly with d, the tails of the probability density function of drifts should scale as e^{-d}. These exponential tails have been observed several times for microswimmers (e.g., Leptos et al. (2009); Zaid et al. (2011); Thiffeault (2015)). Therefore, we expect a distribution of drifts which looks similar to (1.28), but which has a variance that grows with $t^{3/2}$ instead of t.

Note that all of the above discussion is only valid for large t. Although the fact that there is a finite maximum drift due to a single vortex ring guarantees that as $d \to \infty$, the distribution will have exponential tails beyond d_{max}, it is also possible that there are another set of tails outside the core of the distribution which obey a different scaling law and then eventually transition to the exponential tails at some fixed d, similar to the transition between the $-8/3$ power law and the -5 power law observed for the velocity distribution.

Unfortunately, such intermediate-range tails (assuming they exist), are very difficult to analyze. This is because the $1/r$ scaling of drifts for particles where the diffusive front has hit falls off too slowly to make the approximation that the drift due to the nearest vortex ring is the only one which matters. Since we have to add up the contributions due to a number of vortex rings which may depend on the time and on the magnitude of the drift over that time, there is no reason to believe that the moments of the drift distribution for a single vortex can give us the correct scaling either. Therefore, we will have to rely on numerical simulations in order to determine the properties of this part of the distribution.

However, it is still possible to guess at the shape of the distribution using intuition gained from the study of the velocity in Chapter 3. Recall that for the core of the distribution, the velocity was the sum of contributions from many different vortices, while in the tails, the velocity was generally due to a single vortex ring. We now consider each of these cases

separately.

First consider the velocities which contribute to the core of the distribution. For vortices with age in the time interval $[\tau, \tau + \Delta t]$, where $\Delta t \ll R_0^2/4\eta$, the radius of the diffused vortex ring is approximately $\sqrt{4\nu\tau}$, so the probability that a given point is outside of the diffusive front of a particular vortex ring is $1 - (\sqrt{4\nu\tau}/L)^3$, where L is the radius of the domain. Recall from Section 4.1 that the drift is superdiffusive only for times $t \leqslant L^2/4\eta$ (and $t \leqslant T$, where T is the age of the oldest vortices at time $t = 0$), so this probability is generally very close to one, except for the oldest vortices. Since the oldest vortices have the smallest velocities, we expect that most of the vortices contributing to the velocity at a point are far enough away that the point is outside their diffuse fronts. Recall from (2.39) that the contribution to the velocity from these vortex rings is approximately constant in time.

Therefore, we expect the drifts in this case to be ballistic: $\boldsymbol{\Delta} \approx \mathbf{v}(t = 0)t$. Thus, small drifts should grow linearly in time and the core of the drift distribution should have width directly proportional to t.

Now consider the velocities from the tails of the velocity distribution, which are largely due to single vortices. By (3.15), the probability that the velocity due to a single vortex ring is u and comes from a point where $\xi \leqslant 1$ is proportional to

$$p(v = u, \xi \leqslant 1) \propto 0.13682 \frac{\Gamma_0^{5/3} R_0^{10/3}}{\eta} u^{-8/3}. \tag{4.58}$$

Meanwhile, (3.18) implies that

$$p(\nu = u, \xi \geqslant 1) \propto 0.01453 \frac{\Gamma_0^{5/3} R_0^{10/3}}{\eta} u^{-8/3}, \tag{4.59}$$

with the same constant of proportionality. Therefore,

$$p(\xi \geqslant 1 | \nu = u) = \frac{0.13682}{0.13682 + 0.01453} = 90.40\% \tag{4.60}$$

is the probability that a point with a given velocity is inside the diffusive front of the vortex ring. Note that this is independent of u. For small Δt, the velocity at the points inside the diffusive front decreases to $(1 - \frac{3}{2}(\Delta t) t_u^{-5/2})u$, where t_u is the time associated with the velocity u, while the velocity at most points outside the diffusive front remains constant at u. Note that in each case the direction of the velocity is constant – that only changes around the diffusive front. Therefore, the probability that the velocity is u at the end of the time interval is

$$\begin{aligned} p(\nu(\Delta t) = u) &= 0.9040 p_{U^1}((1 - \tfrac{3}{2}(\Delta t) t_u^{-5/2})^{-1} u) + 0.0960 p_{U^1}(u) \\ &\sim 0.9040((1 - \tfrac{3}{2}(\Delta t) t_u^{-5/2})^{-1} u)^{-8/3} + 0.0960 u^{-8/3} \\ &\sim \left(1 - 3.616(\Delta t) t_u^{-5/2}\right) u^{-8/3}. \end{aligned} \tag{4.61}$$

Recall that $t_u = (\Gamma_0 R_0^2 / 12u\sqrt{\pi}\eta^{3/2})^{2/3} \sim u^{-2/3}$, so $t_u^{-5/2} \sim u^{5/3}$. Therefore, for small enough Δt, $p(\nu(\Delta t) = u) = O(u^{-8/3})$, while the scaling changes to $O(u^{-1})$ at somewhat larger Δt. Thus, for the smallest times, the drift

obeys a $-8/3$ power law, which by the generalized central limit theorem means that the distribution should be a (truncated) $\frac{5}{3}$-stable distribution. This power law eventually breaks down for large enough times, but we were already fairly certain that the distribution will eventually become a truncated Gaussian with exponential tails.

In summary, the above heuristic argument predicts that the distribution of drifts after a relatively short time t will be a truncated $\frac{5}{3}$-stable distribution with core width scaling linearly in t. Eventually, the distribution must change shape to become a Gaussian with exponential tails.

Numerical results

In order to test the above heuristics, we generated tracer particle trajectories for randomly-generated suspensions of vortex rings in Matlab. Vortices were generated uniformly in position, age, and orientation throughout a selected rectangular domain centered at the origin oriented with the x-, y-, and z-axes of side-length $2L$ over a time interval $[-T, t_{\text{final}}]$, where the simulation was set to run for $0 \leqslant t \leqslant t_{\text{final}}$. The number of vortices was predetermined using a single Poisson random variable with parameter $\lambda = 8\mu L^3(T + t_{\text{final}})$. Vortices were allowed up evolve using the model for a single vortex ring from Section 2.3 and linear superposition, but individual particle trajectories were integrated using Matlab's ODE45 function. Each simulation was used to generate a single trajectory which started at the origin.

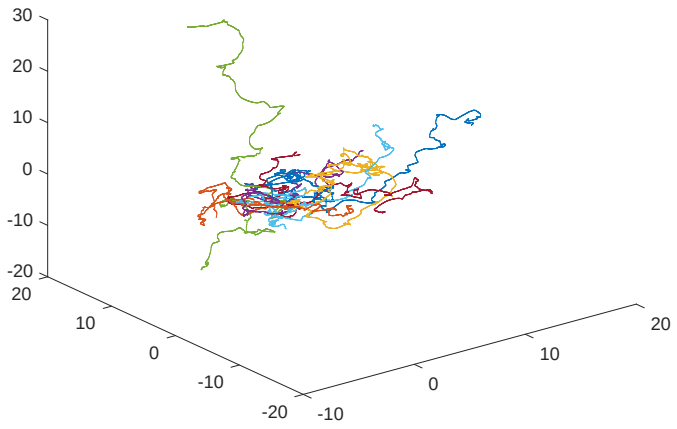

Figure 4.9: Tracer particle trajectories from the origin for fifteen different simulations of the suspension.

Fifteen such trajectories are graphed on the same three-dimensional plot in Figure 4.9. For these particular simulations, the parameters $\mu = 10^{-7}$, $L = 75$, $T = 2000$, and $t_{\text{final}} = 10^4$ were selected. Trajectories for larger domains are not shown since they remained qualitatively very similar. Each of the trajectories exhibits some random motion, but particles tend to continue moving in the same direction they started in with only small deflections periodically. That is, particle paths are seen to be qualitatively in between ballistics and Brownian motion, consistent with a superdiffusive Lévy flight.

We also ran $n = 10^5$ simulations with $\mu = 10^{-6}$, $L = 75$, $T = 1400$, and $t_{\text{final}} = 1000$, in order to determine the full drift distribution. Recall from Section 4.1 that $T \gtrsim t_{\text{final}}$ is necessary to avoid boundary effects from choosing a finite domain. The probability density function $p(d_x)$ for a single component of the drift at a time t_j was computed numerically by

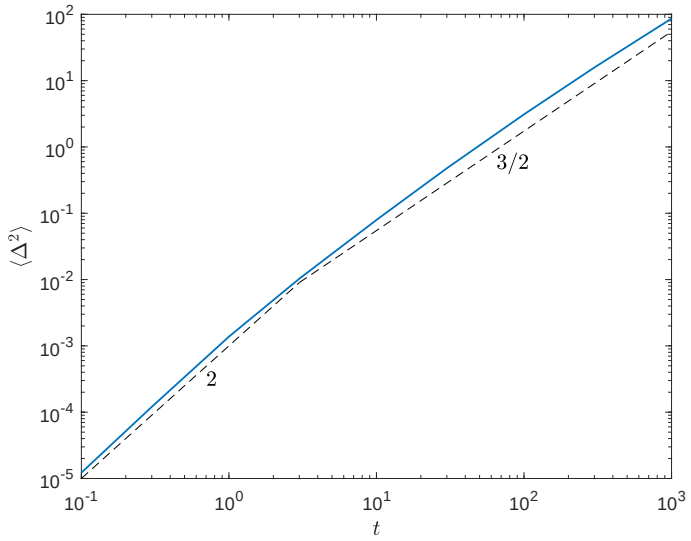

Figure 4.10: The mean square drift as a function of time. We see numerically that $\langle \Delta^2 \rangle \propto t^{3/2}$ for a wide range of times.

placing the results into exponentially-sized bins. The times selected were $t_j = 0.1, 0.3, 1, 3, 10, 30, 100, 300, 1000$. The square drifts for each realization were also averaged in order to obtain the mean square drift as a function of time.

The mean square drift is plotted in Figure 4.10. We see that the slope of the line is approximately equal to $\frac{3}{2}$ for times $3 \lesssim t \lesssim 1000$, so the mean square drift does indeed grow superdiffusively. At early times, however, the particle appears to undergo roughly ballistic motion (there is probably some transition between ballistic motion and the subsequent $t^{3/2}$ scaling which is underresolved). In Figures 4.11-4.12, the probability density function of the x-coordinate of the drifts, d_x, is plotted. The former graph shows that the distribution of drifts at any given time $t \leqslant 100$ collapses

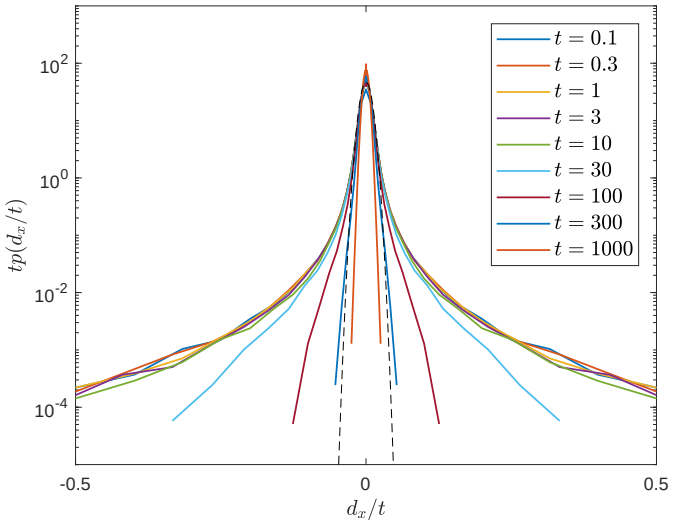

Figure 4.11: The distribution of drifts in the x-direction at various times, normalized by the time. The dashed curve is a Gaussian with standard deviation $\sigma = 0.0085$.

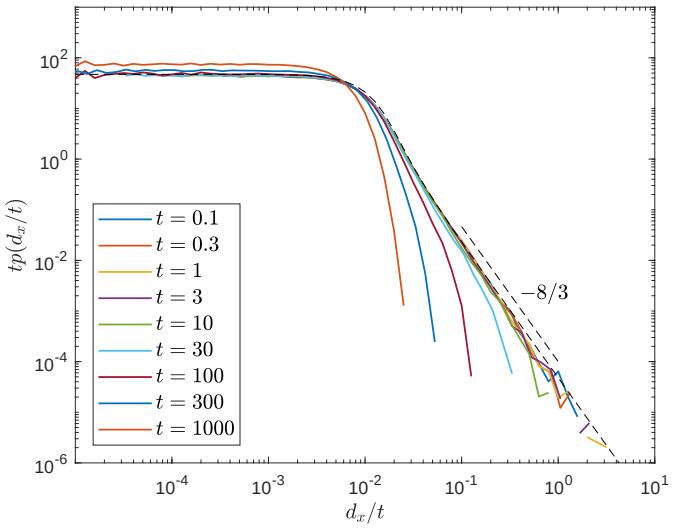

Figure 4.12: The distribution of drifts in the x-direction at various times, normalized by the time. We see that for small times, the distribution is a (truncated) $\frac{5}{3}$-stable distribution with width proportional to t (dashed curve). There is also a dashed line with slope $-8/3$ labeled for reference.

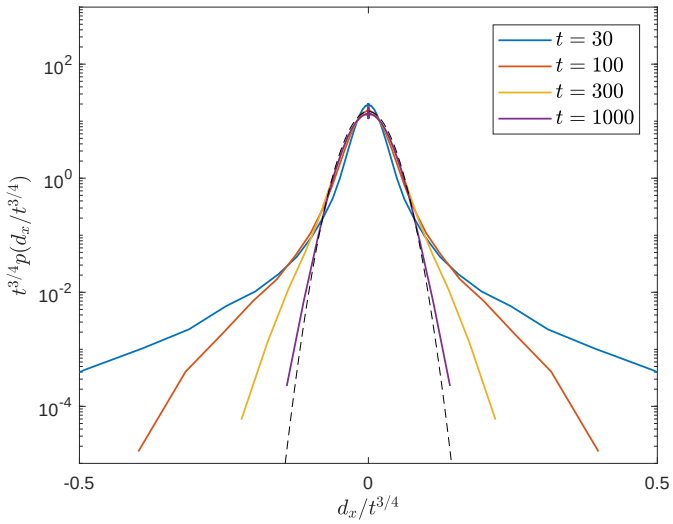

Figure 4.13: The distribution of drifts in the x-direction at later times t, normalized by $t^{3/4}$. We see that the distribution is Gaussian with exponential tails for $t \geqslant 100$. The dashed curve is a Gaussian with standard deviation $\sigma = 0.027$.

onto a single curve (a truncated $\frac{5}{3}$-stable distribution), at least for small drifts, when normalized by the time. This is already quite surprising, since the width of the drift distribution scales as $t^{1/2}$ for microswimmers. For $t > 100$, the distribution appears to have a Gaussian core of width $t^{3/4}$ with exponential tails. The scaling is verified in Figures 4.13-4.14, which also clearly show the transition from a $\frac{5}{3}$-stable distribution to a Gaussian at $t = 100$.

The tails exhibit complex behavior. For early times, we see in Figure 4.12 that the tails scale as $d_x^{-8/3}$, although this behavior does not persist for larger times. We see that as t increases, the value of d_x/t at which the $-8/3$ power law gives way to a faster drop-off decreases. Looking

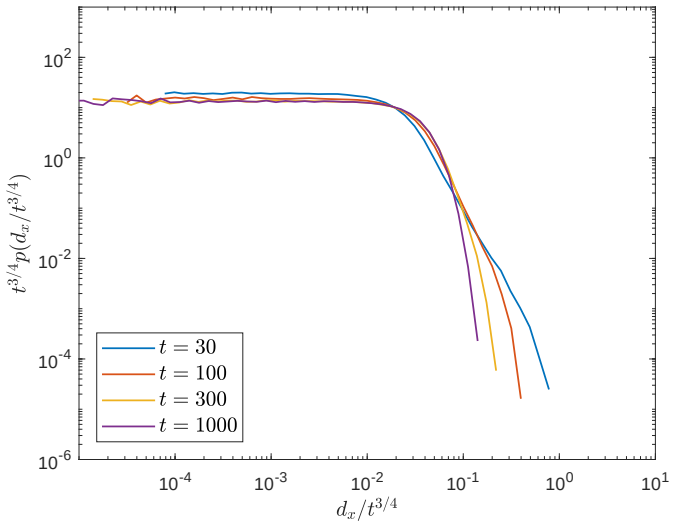

Figure 4.14: The distribution of drifts in the x-direction at later times t, normalized by $t^{3/4}$.

again at Figures 4.11 and 4.13, we see that for larger times, the tails of the probability density function become linear on the semilogarithmic plot, indicating exponential decay, as predicted. The transition in the behavior of the tails corresponds precisely to the transition from a $\frac{5}{3}$-stable distribution to a Gaussian, which follows immediately from the Berry-Esséen theorem (Shlesinger, 1995), just as with the transition in the shape of the velocity distribution observed in Section 3.2. Unlike the observations for microswimmers made by Leptos et al. (2009), however, we do not find that the drift distribution for the suspension of vortices collapses onto a single curve when appropriately normalized in time: the exponential tails seem to vanish as t increases.

4.4 Multipole expansion

Just as with the velocity distribution, the results from this chapter are robust, as they follow immediately from the basic properties of the velocity field, which did not depend on the specifics of the model for the vortex ring.

We can also redo most of the above calculations for the case of velocity disturbances due to force dipoles, quadrupoles, etc. Recall that the velocity field due to a single vortex ring scales as $O(r^{-(n+2)})$ as $r \to \infty$ and $O(t^{-(n+2)/2})$ as $t \to \infty$, where $n = 1$ for a force monopole, $n = 2$, for a force dipole, etc. Then the velocity autocorrelation function will scale as $O(\tau^{(1-2n)/2})$ for large time differences τ. This contrasts with the results found by Zaid et al. (2011), which suggested that the autocorrelation decayed somewhat slower at a rate of $O(\tau^{1-n})$. For each result, these are some caveats about the particular angular dependence of some models, which can lead to the autocorrelation function having asymptotically faster decay, but we will not explore this phenomenon here.

In the case of $n = 1$, we saw that the slow decay of the autocorrelation function implied that the mean square drift grew superlinearly, leading to anomalous diffusion. For $n \geqslant 2$, however, the Taylor-Green-Kubo formula implies that the particle undergoes regular diffusion with diffusivity given by the integral:

$$D = \int_0^\infty c_v(\tau)\, d\tau \tag{4.62}$$

(Graham, 2018).

Since the maximum drift due to a single forcing is finite, regardless of n, we can again expect the distribution of drifts in the suspension to be a truncated Gaussian with exponential tails. However, for $n \geqslant 2$, the width of this distribution now scales as $t^{1/2}$ for long times, so it seems very likely that (1.30) can be used to determine the details of the distribution once the velocity autocorrelations have decayed sufficiently.

4.5 Discussion

We used our analysis of the flow field from Chapter 3 in order to construct a model for the drifts due to a single viscous vortex ring. Far away from the initial impulse, the local drift decays as $1/r$ if the diffusive front has hit, while it decays as t/r^3 for points located far enough away that the diffusive front has not had the opportunity to reach the point yet. Somewhat surprisingly, the second moment of the distribution of drifts scales like $t^{3/2}$. This carries over to the distribution of drifts for the suspension of vortices, so we find that particles in the fluid disperse superdiffusively.

Beyond the moments, the full distribution of drifts at early times was a truncated $\frac{5}{3}$-stable distribution with scale parameter scaling linearly in time. As with the velocity distribution, the large drift distribution will depend heavily on the exact details of the model, although the shape for small to moderately-size drifts (relative to the given time) is likely quite robust.

At later times, the distribution had a Gaussian core with exponential tails, as in (1.28). This distribution differs from the drift distribution for microswimmers, however, in that it is wider, with core width scaling as $t^{3/4}$ instead of $t^{1/2}$. This larger power can be understood in terms of the diffusion of momentum, which occurs too slowly to kill the correlations between the velocity now and at a later time, which scale as $O(\tau^{-1/2})$. Therefore, particles drift in the same direction for a longer period of time, resulting in asymptotically larger drifts.

The transition from a non-Gaussian stable distribution to a Gaussian distribution as time increases is indicative of a (perhaps unsurprising) transition from the bulk of the contribution to the mean square drift coming from individual impulses (vortices) at short times, to the main contribution coming from the many vortices at long times. Since the main contribution to the energy generally comes from the closest vortex ring, this observation suggests that particles are primarily moving around under the action of several vortices in series. However, since individual vortices can only move particles a finite distance, it is clear that the far-field drifts, generally due to many vortices acting simultaneously, must also play a central role in determining particle displacements. More research is necessary to clarify the precise roles of the near- and far-field contributions to the drifts.

This work is limited in that we have been unable to provide an analytic explanation for the shape of the drift distribution at small times. We have also neglected the nonlinear terms in the Navier–Stokes equations, which

may affect the results, except in imposing an upper bound in how far an individual vortex ring can cause a single particle to move. However, since the neglected terms are small in the far field, it seems likely that nonlinearity does not completely kill the enhancement to the drift, at least at small μ (i.e., $\phi \ll 1$). Future study is necessary in order to fill in the gaps analytically and to determine what role nonlinearity plays in the determination of the drifts, especially as the production rate μ increases.

Finally, it is an open question how well these results apply to other, more realistic, models of swimming. True force monopoles do not actually exist in nature, so swimming should generally produce a force dipole, barring the possibility of external forcing. Correlations between different strokes in swimming, which often occur on a time scale which is much shorter than the scale R_0^2/η, may affect the shape of the distribution and require further study, as do the effects of anisotropy.

REFERENCES

Bühler, O. 2007. Impulsive fluid forcing and water strider locomotion. *J. Fluid Mech.* 573:211–236.

Caflisch, R. E., and J. H. C. Luke. 1985. Variance in the sedimentation speed of a suspension. *Physics of Fluids* 28(3):759–760.

Cantwell, Brian, and Nicholas Rott. 1988. The decay of a viscous vortex pair. *Physics of Fluids* 31(11):3213–3224.

Cater, J. E., J. Soria, and T. T. Lim. 2004. The interaction of the piston vortex with a piston-generated vortex ring. *J. Fluid Mech.* 499:327–343.

Colin, S. P., and J. H. Costello. 2002. Morphology, swimming performance and propulsive mode of six co-occurring hydromedusae. *Journal of experimental biology* 205(3):427–437.

Colin, S. P., J. H. Costello, J. O. Dabiri, A. Villanueva, J. B. Blottman, B. J. Gemmell, and S. Priya. 2012. Biomimetic and live medusae reveal the mechanistic advantages of a flexible bell margin. *PLoS One* 7(11):e48909.

Dabiri, J. O., S. P. Colin, and J. H. Costello. 2006. Fast-swimming hydromedusae exploit velar kinematics to form an optimal vortex wake. *Journal of Experimental Biology* 209(11):2025–2033.

Dabiri, J. O., S. P. Colin, J. H. Costello, and M. Gharib. 2005. Flow patterns generated by oblate medusan jellyfish: field measurements and laboratory analyses. *Journal of Experimental Biology* 208(7):1257–1265.

Dabiri, John O. 2006. Note on the induced Lagrangian drift and added-mass of a vortex. *J. Fluid Mech.* 547(-1):105.

Dabiri, John O., and Morteza Gharib. 2004. Fluid entrainment by isolated vortex rings. *J. Fluid Mech.* 511:311–331.

Delbende, Ivan, and Maurice Rossi. 2009. The dynamics of a viscous vortex dipole. *Physics of Fluids* 21(7):073605.

Delmotte, B., E. E. Keaveny, E. Climent, and F. Plouraboué. 2018. Simulations of Brownian tracer transport in squirmer suspensions. *IMA J. of Applied Math.* 84(4):680–699.

Dewar, W. K., R. J. Bingham, R. L. Iverson, D. P. Nowacek, L. C. St. Laurent, and P. H. Wiebe. 2006. Does the marine biosphere mix the ocean? *J. Marine Research* 64:541–561.

Dombrowski, C., L. Cisneros, S. Chatkaew, R. E. Goldstein, and J. O. Kessler. 2004. Self-concentration and large-scale coherence in bacterial dynamics. *Phys. Rev. Lett.* 93(9):098103.

Drescher, K. D., R. E. Goldstein, N. Michel, M. Polin, and I. Tuval. 2010. Direct measurement of the flow field around swimming microorganisms. *Phys. Rev. Lett.* 105:168101.

Feller, W. 1971. *An introduction to probability theory and its applications, volume 2*. New York: John Wiley & Sons.

Fukumoto, Y. 2010. Global time evolution of viscous vortex rings. *Theoretical and Computational Fluid Dynamics* 24(1-4):335–347.

Fukumoto, Y., and F. Kaplanski. 2008. Global time evolution of an axisymmetric vortex ring at low Reynolds numbers. *Physics of Fluids* 20(5): 053103.

Gnedenko, V. V., and A. N. Kolmogorov. 1968. *Limit distributions of sums of independent random variables*. Reading: Addison-Wesley.

Graham, M. D. 2018. *Microhydrodynamics, brownian motion, and complex fluids*. Cambridge, U.K.: Cambridge University Press.

Guasto, J. S., K. A. Johnson, and J. P. Gollub. 2010. Oscillatory flows induced by microorganisms swimming in two-dimensions. *Phys. Rev. Lett.* 105:168102.

Guazzelli, E., and J. Hinch. 2011. Fluctutations and instability in sedimentation. *Annu. Rev. Fluid Mech.* 43:97–116.

Hamlet, C., L. A. Miller, T. Rodriguez, and A. Santhanakrishnan. 2012. The fluid dynamics of feeding in the upside-down jellyfish. In *Natural locomotion in fluids and on surfaces*, 35–51. Springer.

Helmholtz, H. 1858. über integrale der hydrodynamischen gleichunger welche den wirbelbewegungen entsprechen. *Crelles J.* 55:25–55.

Hill, M. J. M. 1894. On a spherical vortex. *Philos. Trans. Royal Soc. Lond. A* 185:213–245.

Hoover, A. P., B. E. Griffith, and L. A. Miller. 2017. Quantifying performance in the medusan mechanospace with an actively swimming three-dimensional jellyfish model. *Journal of Fluid Mechanics* 813:1112–1155.

Hörmander, L. 1983. *The analysis of linear partial differential operators i*. Berlin: Springer-Verlag.

Huntley, M. E., and M. Zhou. 2004. Influence of animals on turbulence in the sea. *Marine Ecology Progress Series* 273:65–79.

Ishikawa, T. 2009. Suspension biomechanics of swimming microbes. *J. Roy. Soc. Interface* 6:815–834.

Ishikawa, T., and T. J. Pedley. 2007. Diffusion of swimming model microorganisms in a semi-dilute suspension. *J. Fluid Mech.* 588:437–462.

Jiang, H., and T. Kiørboe. 2011. The fluid dynamics of swimming by jumping in copepods. *J. Roy. Soc. Interface* 8(61):1090–1103.

Jiang, H., and J. R. Strickler. 2007. Copepod flow modes and modulation: a modelling study of the water currents produced by an unsteadily swimming copepod. *Philos. Trans. Royal Soc. Lond. B* 362:1959–1971.

Katija, K., and J. O. Dabiri. 2009. A viscosity-enhanced mechanism for biogenic ocean mixing. *Nature* 460:624–627.

Kelvin, Lord. 1867. The translatory velocity of a circular vortex ring. *Philos. Mag.* 33:511–512.

Kremien, M., U. Shavit, T. Mass, and A. Genin. 2013. Benefit of pulsation in soft corals. *Proceedings of the National Academy of Sciences* 201301826.

Lamb, H. 1932. *Hydrodynamics*. Sixth ed. Cambridge: Cambridge University Press.

Leptos, K. C., J. S. Guasto, J. P. Gollub, A. I. Pesci, and R. E. Goldstein. 2009. Dynamics of enhanced tracer diffusion in suspensions of swimming eukaryotic microorganisms. *Phys. Rev. Lett.* 103:198103.

Lévy, P. 1925. *Calcul des probabilités*. Paris: Gauthier-Villars.

Lin, Z., J.-L. Thiffeault, and S. Childress. 2011. Stirring by squirmers. *J. Fluid Mech.* 669:167–177.

Luke, J. H. C. 2000. Decay of velocity fluctuations in a stably stratified suspension. *Physics of Fluids* 12(6):1619–1621.

Maxworthy, T. 1972. The structure and stability of vortex rings. *J. Fluid Mech* 51(1):15–32.

McHenry, M. J., and J. Jed. 2003. The ontogenetic scaling of hydrodynamics and swimming performance in jellyfish Aurelia aurita. *J. Exp. Biol.* 206:4125–4137.

Min, I. A., I. Mezic, and A. Leonard. 1996. Lévy stable distributions for velocity and velocity difference in systems of vortex elements. *Physics of Fluids* 8(5):1169–1180.

Möller, J., and T. Naraynan. 2017. Velocity fluctuations in sedimenting brownian particles. *Phys. Rev. Lett.* 118(19):198001.

Morrell, T., S. Spagnolie, and J.-L. Thiffeault. 2019. Velocity fluctuations in a dilute suspension of viscous vortex rings. *Phys. Rev. Fluids* 4(4):044501.

Mucha, P. J., S.-Y. Tee, D. A. Weitz, B. I. Shraiman, and M. P. Brenner. 2004. A model for velocity fluctuations in sedimentation. *J. Fluid Mech.* 501: 71–104.

Nawroth, J. C., H. Lee, A. W. Feinberg, C. M. Ripplinger, M. L. McCain, A. Grosberg, J. O. Dabiri, and K. K. Parker. 2012. A tissue-engineered jellyfish with biomimetic propulsion. *Nature Biotechnology* 30(8):792.

Nicolai, H., and B. Herzhaft. 1995. Particle velocity fluctuations and hydrodynamic self-diffusion of sedimenting non-brownian spheres. *Physics of Fluids* 7(1):12–23.

Olesen, N. J., K. Frandsen, and H. U. Riisgård. 1994. Population dynamics growth and energetics of jellyfish Aurelia aurita in a shallow fjord. *Marine Ecology Progress Series* 105:9–18.

Ortlieb, L., S. Rafaï, P. Peyla, C. Wagner, and T. John. 2019. Statistics of colloidal suspensions stirred by microswimmers. *Phys. Rev. Lett.* 122: 148101.

Phillips, O. M. 1956. The final period of decay of non-homogeneous turbulence. *Mathematical Proceedings of the Cambridge Philosophical Society* 52(01):135.

Pushkin, D. O., and J. M. Yeomans. 2013. Fluid mixing by curved trajectories of microswimmers. *Phys. Rev. Lett.* 111:188101.

Rott, N., and B. Campbell. 1993. Vortex drift. i: Dynamic interpretation. *Phys. of Fluids A* 5:1443–1450.

Rushkin, I., V. Kantsler, and R. E. Goldstein. 2010. Fluid velocity fluctuations in a suspension of swimming protists. *Physical Review Letters* 105: 188101.

Saffman, P. G. 1967. The large-scale structure of homogeneous turbulence. *J. Fluid Mech.* 27(3):581–593.

———. 1970. The velocity of viscous vortex rings. *Studies in Applied Mathematics* 49(4):371–380.

———. 1992. *Vortex dynamics*. Cambridge, U.K.: Cambridge University Press.

———. 1997. Vortex models of isotropic turbulence. *Philosophical Transactions of the Royal Society of London A: Mathematical, Physical and Engineering Sciences* 355(1731):1949–1956.

Samson, J. E., N. A. Battista, S. Khatri, and L. A. Miller. 2017. Pulsing corals: A story of scale and mixing. *preprint arXiv:1709.04996*.

Shadden, Shawn C., John O. Dabiri, and Jerrold E. Marsden. 2006. Lagrangian analysis of fluid transport in empirical vortex ring flows. *Physics of Fluids* 18(4):047105.

Shariff, Karim, and Anthony Leonard. 1992. Vortex rings. *Annual Review of Fluid Mechanics* 24(1):235–279.

Shlesinger, M. F. 1995. Comment on "stochastic process with ultraslow convergence to a gaussian: The truncated lévy flight". *Phys. Rev. Lett.* 74(24):4959.

Stanaway, S K, B J Cantwell, and P R Spalart. 1988. A Numerical Study of Viscous Vortex Rings Using a Spectral Method. Tech. Rep. 101401, NASA.

Synge, J. L., and C. C. Lin. 1943. On a statistical model of isotropic turbulence. *Transactions of the Royal Society of Canada* 37:45–79.

Tait, P. G. 1867. Translation of 'on integrals of the hydrodynamical equations which express vortex-motion' by h. helmholtz. *Philos. Mag.* 33: 485–512.

Thiffeault, J.-L. 2015. Distribution of particle displacements due to swimming microorganisms. *Phys. Rev. E* 92:023023.

Underhill, P. T., J. P. Hernandez-Ortiz, and M. D. Graham. 2008. Diffusion and spatial correlations in suspensions of swimming particles. *Phys. Rev. Lett.* 100:248101.

Villanueva, A., C. Smith, and S. Priya. 2011. A biomimetic robotic jellyfish (Robojelly) actuated by shape memory alloy composite actuators. *Bioinspiration & biomimetics* 6(3):036004.

Visser, A. W. 2007. Biomixing of the oceans? *Science* 316:838–839.

Voit, J. 2005. *The statistical mechanics of financial markets*. 3rd ed. Berlin: Springer-Verlag.

Yeomans, J. M., D. O. Pushkin, and H. Shum. 2014. An introduction to the hydrodynamics of swimming microorganisms. *Eur. Phys. J. Special Topics* 223(9):1771–1785.

Zaid, I., and D. Mizuno. 2016. Analytical limit distributions from random power-law interactions. *Phys. Rev. Lett.* 117:030602.

Zaid, I. M., J. Dunkel, and J. M. Yeomans. 2011. Lévy fluctuations and mixing in dilute suspensions of algae and bacteria. *J. Roy. Soc. Interface* 8: 1314–1331.

INDEX